Title	Characterizations of drying-infiltration and reaction processes in water-unsaturated sandstone
Author(s)	西山, 直毅
Citation	大阪大学, 2014, 博士論文
Version Type	VoR
URL	https://doi.org/10.18910/34033
rights	
Note	

Doctoral Thesis

Characterizations of drying-infiltration and reaction processes in water-unsaturated sandstone

不飽和砂岩中の乾燥-浸透と反応過程の
キャラクタリゼーション

Naoki Nishiyama　　西山　直毅

Department of Earth and Space Science,
Graduate School of Science, Osaka University

February, 2014

Abstract

When water infiltrates into the pores of a rock near the Earth's surface, water contacts mineral surfaces, interacts with the mineral (e.g., the dissolution and precipitation of minerals and the adsorption-desorption of dissolved solutes), and transports reactants by flow. To quantify such water-rock interaction, it is essential to evaluate the parameters characterizing the reaction and transport properties of the rock. Rock pores above the water table are usually not saturated with water. Water saturation changes depending on the conditions of drying and wetting, resulting in the complex distributions of water and air in pore spaces. Air in pores may disturb water flow and reduce the surface area available for reactions by limiting the contact between the mineral surfaces and water. In view of these points, I have investigated the effect of water saturation on (1) the distribution of water and air, (2) the hydraulic conductivity (a parameter describing the velocity of fluid flow percolating the rock), and (3) the reactive (mineral-water contact) surface area.

First, the distributions of water and air in pores as a function of pore size during drying−infiltration processes were characterized by the water-expulsion porosimetry, and the results were used to discuss the mechanisms of the decrease of hydraulic conductivity with water saturation. A core of Fontainebleau sandstone, having an open porosity of 6.3% and pore diameters of 2–43 μm, consisting of ~100% quartz, was used. Evaluation of the size distribution of pore water under various degrees of drying revealed that the volume of pore water decreased successively from larger pores to smaller ones as drying proceeded, which reflected the migration of water driven by capillary pressure differences in each pore size class. In the case of infiltration, water was passed through the sample preliminarily adjusted to various degrees of drying, and the size distribution of pore water and hydraulic conductivity were measured. The results showed that air was preferentially entrapped in the pores of specific size, which seemed to be the reason of the significant decrease of hydraulic conductivity with decreasing water saturation.

Secondly, to investigate the relationship between the reactive surface area and water saturation, flow-through dissolution experiments were performed using the core of Fontainebleau sandstone at various water saturations. The water saturation of the core was adjusted to 0, 51, or 100% by drying, and at each saturation, water was infiltrated into the core at a constant pressure. The experimental results showed that the total amount of dissolved Si did not change with decreasing water saturation. It can be therefore concluded that virtually all of the mineral surfaces in air-containing pores were wetted with water film and allowed the progression of dissolution; i.e., the reactive

surface area was not affected by water saturation despite the presence of air in the pores. The results also suggested that the flushing rate of dissolved Si from the interior of the water film to the exterior was fast enough to keep the Si concentration in the film sufficiently lower than the equilibrium concentration of quartz.

Thirdly, to theoretically underpin the results of flow-through dissolution experiment and to discuss a general concept of the relationship between water saturation and reactive surface area, two models, one is a model for estimating the thickness of water film on pore walls, and the other is a reactive-transport model describing the dissolution and diffusion in water film, were constructed. The first model shows that the water film thickness changes depending on the pore diameter in which air is present, mineral type, and pore solution compositions. Especially for the system in which quartz grains contact dilute pore solution, the thickness of water film is mainly controlled by pore diameter: the larger the size of pores, the thicker the water film. In the case of the Fontainebleau sandstone, film thicknesses of 7–18 nm were estimated. The reactive-transport model shows that the solute concentration in water film is a function of the film thickness, diffusion length (~grain size), dissolution rate of the mineral, equilibrium concentration, and roughness factor. The reactive-transport calculation confirmed that the total amount of dissolution of the sandstone sample was almost unaffected by water saturation owing to the high flushing efficiency of dissolved Si in water film, which agrees with the experimental result. Finally, the models were applied to various sedimentary rocks differing in mineral compositions, grain sizes, and pore diameters, and a diagram to assess whether the reactive surface area and the dissolution rate are affected by water saturation was derived.

Acknowledgements

Table of Contents

Abstract

2.1. Introduction

2.2. Experimental Methods

    2.2.1. Sample Descriptions

    2.2.2. Drying of Pore Water and Adjustment of Pre-flow Saturation

    2.2.3. Measurement of Size Distribution of Pore Water after Drying

    2.2.4. Measurement of Hydraulic Conductivity

    2.2.5. Measurement of Size Distribution of Pore Water after Infiltration

2.3. Theoretical Models

    2.3.1. MVG Model and its Modified Version

    2.3.2. Estimation of Model Parameters

2.4. Results

    2.4.1. Rate of Drying

    2.4.2. Time Variations of Water Saturation and Flow Rate

    2.4.3. Relationship between Pre-flow Saturation and Air Entrapment

    2.4.4. Relationship between Water Saturation and Hydraulic Conductivity

    2.4.5. Size Distributions of Pore Water after Drying and Infiltration

        2.4.5.1. Bulk Pore Structure

        2.4.5.2. Pore Water after Drying

        2.4.5.3. Pore Water after Infiltration

2.5. Discussion

    2.5.1. Cause of the Decrease of Hydraulic Conductivity

    2.5.2. Comparison of the Size Distributions of Pore Water and Hydraulic Conductivities Obtained by Model and Experiment

2.6. Conclusions

Chapter 1

General Introduction

Advances in the understanding of water-rock interaction near the Earth's surface are important for considering natural and engineering processes including groundwater chemistry, contaminant transport, geological sequence of carbon dioxide, and weathering of rocks. Water-rock interaction progresses by the combination of geochemical reactions (dissolution and precipitation of minerals, adsorption–desorption of dissolved matters, and ion exchange) and the transport of solutes by flow and diffusion in pore water (Fig. 1.1). As an example of water-rock interaction, when rock-forming minerals dissolve and dissolved solutes are flushed by water flow (the case of chemical weathering), the concentration of a component c (mol m^{-3}) along flow paths (x) can be written by the following one-dimensional version of reactive-transport equation:

$$\frac{\partial c}{\partial t} = -v\frac{\partial c}{\partial x} + \frac{A}{\phi}r_{const}\left(1 - \frac{c}{c_{eq}}\right) \qquad (1.1)$$

where t (s) is the time, v (m s^{-1}) is the flow velocity in pore water, A (m^2 m^{-3}) is the mineral-water reactive surface area of the rock, ϕ is the porosity of the rock, r_{const} (mol m^{-2} s^{-1}) is the dissolution rate constant, and c_{eq} (mol m^{-3}) is the equilibrium concentration. Such reactive-transport modeling allows the rate and extent of the water-rock interaction to be evaluated. Therefore, the understanding of each parameter characterizing the reaction and transport properties of the rock is an essential first step toward quantitatively understanding the whole picture of the water-rock interaction.

The rock pores below the water table are usually saturated with water, and thereby all mineral surfaces are available for reactions and solutes migrate throughout the pores. In contrast, rocks above the water table undergo drying and infiltration, and the pores are not saturated with water. This region, known as the vadose zone or the unsaturated zone, ranges in depth from a few meters to hundreds of meters from the ground surfaces (*Zimmerman and Bodvarsson*, 1989). When water is supplied to a completely or partially dried rock, water displaces air in pores and starts to flow through the pores. However, some of air is confined by pore water and remains in pore spaces as entrapped air (*Faybishenko*, 1995). In such process, it is known that more air is trapped in drier rock (e.g., *Land*, 1968; *Suzanne et al.*, 2003). Consequently, water saturation (volume of pore water/volume of open pores) changes depending on the condition of drying and wetting. Because the change in water saturation potentially affects some parameters in the reactive-transport model, evaluation of the influences is essential for quantitative treatment of water-rock interaction in the vadose zone. The rate constants and

equilibrium constants of various reactions generally depend on the type of mineral and the composition of pore solution, and they will not vary with water saturation. In contrast, the transport properties and the reactive surface area are likely to be affected by water saturation.

The occurrence of air entrapment can reduce the volume of pores available for water flow and make the flow paths more tortuous. This suggests that hydraulic conductivity, a parameter characterizing flow velocity (v in Eq. (1.1)) at a given hydraulic gradient, is affected by the changes in water saturation. In fact, the effect of water saturation on the hydraulic conductivity has been relatively well studied for soils (e.g., *Gupta and Swartzendruber*, 1964; *Lenhard and Parker*, 1987; *Sakaguchi et al.*, 2005). As to rocks, there have been many efforts to study the hydraulic conductivity under water-saturated condition (e.g., *Walsh and Brace*, 1984; *Katz and Thompson*, 1986; *Yokoyama and Takeuchi*, 2009; *Bernabé et al.*, 2010), while there have been few studies focusing on porous rocks in the vadose zone where water and air coexist in pores at low hydraulic gradient. Moreover, how pore water and entrapped air are distributed in each pore size class remains poorly understood (*Parker and Lenhard*, 1987; *Fugerlund et al.*, 2008). Because the size of flow path is a critical factor controlling the hydraulic conductivity, to know the size distributions of pore water and air is important for considering how the occurrence of air entrapment affects the hydraulic conductivity.

The decreases in water saturation also have the potential to reduce the surface area available for geochemical reactions (A in Eq. (1.1)) because air may limit the degree of contact between mineral surfaces and water. The reactive surface area, an essential parameter for quantifying various reactions, has often been estimated by geometric calculation or Brunauer−Emmet−Teller (BET) method (e.g., *White and Peterson*, 1990; *Gautier et al.*, 2001; *White and Brantley*, 2003). The geometric calculation yields the surface area by assuming that the mineral grains or pores have smooth surfaces and uniform geometry (e.g., sphere). The BET method determines the surface area by measuring the volume of adsorbed inert gas such as N_2 and Kr on mineral surfaces. Although the values obtained by these approaches are likely to be reasonable estimations of the reactive surface areas for water-saturated rocks, they may not be appropriate for unsaturated rocks because the effect of water saturation on the reactive surface area must be taken into account. To address this issue, *Saripalli* (2008) has developed a theoretical model describing the reactive surface area of unsaturated porous media. In this model, the reactive surface area decreases with decreasing water saturation because only the surfaces of water-filled pores are assumed to react. In

contrast, previous experiments using mineral plates have shown that the surfaces of minerals exposed to air are covered with adsorbed water, although water film have a variety of thicknesses depending on relative humidity and the type of mineral: quartz (*Pashley and Kitchener*, 1979; *Gee et al.*, 1999), glass (*Busscher et al.*, 1986), calcite (*Bohr et al.*, 2010), and muscovite (*Beaglehole and Christenson*, 1992; *Balmer et al.*, 2008). Moreover, observations of the surfaces of calcite in contact with air have shown the occurrences of dissolution and growth, which is interpreted as a reaction induced by a water film adsorbed on the surfaces (e.g., *Stipp et al.*, 1996; *Hausner et al.*, 2007). If such water film is present in the rock pores having complicated pore structure, the surfaces of pores occupied by air may be available for reactions. Therefore, to understand how the geochemical reaction is affected by water saturation, it is necessary to know the extent to which the pore surfaces are wetted with water film and to elucidate whether the water film has an ability to induce reactions and transport solutes.

With these points in mind, the aims of this study are (1) to evaluate the distributions of water-filled pores, air-filled pores, and water film in each pore size class in an unsaturated sandstone, (2) to experimentally investigate how the hydraulic conductivity and reactive surface area of the sandstone change depending on water saturation, and (3) to interpret the effect of water saturation on the hydraulic conductivity and reactive surface area on the basis of the evaluated distributions of pore water−air−water film. In my doctoral thesis, I first characterized the distribution of pore water and air as a function of pore size during drying−infiltration processes by the water-expulsion porosimetry (e.g., *Gelinas and Angers*, 1986; *Yokoyama and Takeuchi*, 2009). This porosimetry is the method that pore water is expelled by increasing gas pressure in a stepwise fashion and the volumes of water in each pore size class are quantified. The size distributions of pore water of a sandstone core were determined under various degrees of drying. In addition, water was infiltrated in the sandstone initially adjusted to various degrees of drying, and the hydraulic conductivity and the size distribution of pore water were measured. On the basis of the results, the ease of water infiltration/air entrapment as a function of pore size and its relevance to the decreases in hydraulic conductivity were discussed. Next, to investigate the effect of water saturation on the reactive surface area, water was infiltrated in the sandstone initially adjusted to water-saturated or dried conditions, and the amounts of dissolved elements in the effluent were compared. The results showed that water film wetting pore surfaces plays an important role in the reaction under unsaturated conditions. To theoretically underpin the experimental results, I constructed two models, one is a model for estimating the thickness of water film on pore walls, and the other is a

reactive-transport model considering the effect of water film. Finally, by applying the reactive-transport model to rocks with a variety of mineral compositions and grain sizes, I considered the effect of water saturation on dissolution behavior in general cases.
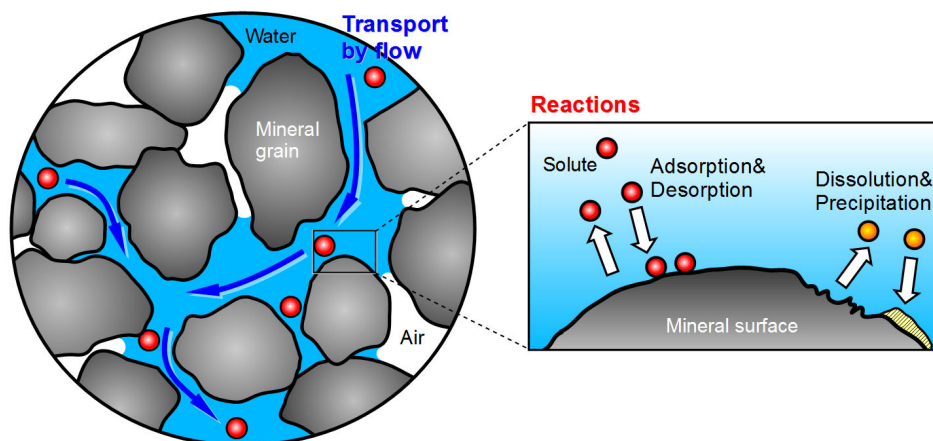
Fig. 1.1. Schematic of water-rock interaction in pore spaces under a water-unsaturated condition.

References

Balmer T. E., Christenson H. K., Spencer N. D. and Heuberger M. (2008) The effect of surface ions on water adsorption to mica. *Langmuir* **24**, 1566–1569.

Beaglehole D. and Christenson H. K. (1992) Vapor adsorption on mica and silicon: Entropy effects, layering, and surface forces. *J. Phys. Chem.* **96**, 3395–3403.

Bernabé Y., Li, M. and Maineult, A. (2010) Permeability and pore connectivity: a new model based on network simulations. *J. Geophys. Res.* **115**, B10203.

Bohr J., Wogelius R. A., Morris P. M. and Stipp S. L. S. (2010) Thickness and structure of the water film deposited from vapour on calcite surfaces. *Geochim. Cosmochim. Acta* **74**, 5985–5999.

Busscher H. J., Kip G. A. M., van Silfhout A. and Arends J. (1986) Spreading pressures of water and n-propanol on polymer surfaces. *J. Colloid Interface Sci.* **114**, 307–313.

Faybishenko B. (1995) Hydraluic behavior of quasi-saturated soil in the presence of entrapped air: laboratory experiments. *Water Resour. Res.* **31**, 2421–2435.

Fagerlund F., Niemi A. and Illangasekare T. H. (2008) Modeling of nonaqueous phase liquid (NAPL) migration in heterogeneous saturated media: effects of hysteresis and fluid immobility in constitutive relations, *Water Resour. Res.* **44**, W03409.

Gautier J. M., Oelkers E. H. and Schott J. (2001) Are quartz dissolution rates proportional to

B.E.T surface areas? *Geochim. Cosmochim. Acta* **65**, 1059–1070.

Gee M. L., Healy T. W. and White L. R. (1999) Hydrophobicity effects in the condensation of water films on quartz. *J. Colloid Interface Sci.* **140**, 450–465.

Gelinas C. and Angers R. (1986) Improvement of the dynamic water-expulsion method for pore size distribution measurements. *Am. Ceram. Soc. Bull.* **65**, 1297−1300.

Gupta R. P. and Swartzendruber D. (1964) Entrapped air content and hydraulic conductivity of quartz sand during prolonged liquid flow. *Soil Sci. Soc. Am. J.* **28**, 9–12.

Hausner D. B., Reeder R. J. and Strongin D. R. (2007) Humidity-induced restructuring of the calcite surface and the effect of divalent heavy metals. *J. Colloid Interface Sci.* **305**, 101–110.

Katz A. J. and Thompson A. H. (1986) Quantitative prediction of permeability in porous rock. *Phys. Rev. B* **34**, 8179–8181.

Land C. S. (1968) Calculation of imbibition relative permeability for two- and three-phase flow from rock properties. *Soc. Pet. Eng. J. Trans. Am. Inst. Min. Metall. Pet. Eng.* **243**, 149–156.

Lenhard R. J. and Parker J. C. (1987) A model for hysteretic constitutive relations governing multiphase flow: 2. Permeability-saturation relations. *Water Resour. Res.* **23,** 2197–2206.

Parker J. C. and Lenhard R. J. (1987) A model for hysteretic constitutive relations governing multiphase flow: 1. Saturation-pressure relations. *Water Resour. Res.* **23,** 2187–2196.

Pashley R. M. and Kitchener J. A. (1979) Surface forces in adsorbed multilayers of water on quartz. *J. Colloid Interface Sci.* **71**, 491–500.

Sakaguchi A., Nishimura T., and Kato M. (2005) The effect of entrapped air on the quasi-saturated soil hydraulic conductivity and comparison with the unsaturated hydraulic conductivity, *Vadose Zone J.* **4**, 139−144.

Saripalli K. P., Freedman V. L., McGrail B. P. and Meyer P. D. (2006) Characterization of the specific solid-water interfacial area-water saturation relationship and its import to reactive transport. *Vadose Zone J.* **5**, 777–783.

Stipp S. L. S., Gutmannsbauer W. and Lehmann T. (1996) The dynamic nature of calcite surfaces in air. *Am. Mineral.* **81**, 1–8.

Suzanne K., Haman G., Billiotte J. and Trocme V. (2003) Experimental relationships between residual gas saturation and initial gas saturation in heterogeneous sandstone reservoirs. Paper presented at SPE Annual Technical Conference and Exhibition, SPE, Denver, Colorado.

Walsh J. B. and Brace W. F. (1984) The effect of pressure on porosity and the transport properties of rock. *J. Geophys. Res.* **89**, 9425–9431.

White A. F. and Peterson M. L. (1990) Role of reactive-surface-area characterization in

geochemical kinetic models. *In Chemical modeling of aqueous systems II*. ACS symposium series 416. Eds. D. C. Melchior and R. L. Bassett. 461–475.

White A. F. and Brantley S. L. (2003) The effect of time on the weathering of silicate minerals: why do weathering rates differ in the laboratory and field? *Chem. Geol.* **202**, 479–506.

Yokoyama T. and Takeuchi S. (2009) Porosimetry of vesicular volcanic products by a water-expulsion method and the relationship of pore characteristics to permeability. *J. Geophys. Res.* **114**, B02201.

Zimmerman R. W. and Bodvarsson G. S. (1989) An approximate solution for one-dimensional absorption in unsaturated porous-media. *Water Resour. Res.* **25**, 1422−1428.

Chapter 2

Size Distributions of Pore Water and Entrapped Air during Drying-Infiltration Processes of Sandstone Characterized by Water-Expulsion Porosimetry

Abstract

The transport of pore water in a rock during drying-infiltration processes was characterized by water-expulsion porosimetry. In this method, pore water is expelled by increasing gas pressure in a stepwise fashion, and the amounts of water in each pore size class are determined. Fontainebleau sandstone, having an open porosity of 6% and main pore radii of 1–20 μm, was used. The change in size distribution of pore water was determined as a function of the degree of drying. As the drying proceeded, the amount of water decreased first in the larger pores followed by the smaller pores. Next, water was infiltrated into the sample preliminarily adjusted to various water saturations ($S_{pre-flow}$), and the entrapped air saturation, hydraulic conductivity (K), and size distribution of pore water were measured. As $S_{pre-flow}$ decreased, the entrapped air saturation increased and K decreased as approximated by $K \propto S_{flow}^{4.5}$, where S_{flow} is the water saturation after the infiltration. A comparison of the size distributions of pore water before and after the infiltration revealed that the ease of water infiltration (air entrapment) depends on pore size. If pores of >8 μm radii were emptied by drying, they were readily refilled with water, whereas smaller pores were only partially refilled because air was trapped in them. The experimentally measured K-S_{flow} relationship generally agreed with those predicted by the Mualem-van Genuchten model and its modified version accounting for air entrapment, but some differences in the size distribution of pore water were observed between the experiment and the models.

2.1. Introduction

Knowledge of the transport of water in rocks is essential for understanding the material transport in the Earth's surface. Rocks above water tables are usually partially saturated, and this region is known as the vadose zone. The depth of the vadose zone ranges from a few meters to a few hundreds of meters from the ground surface (*Zimmerman and Bodvarsson*, 1989). Water saturation in rocks, namely, the proportion of the volume of pore water to total volume of open pores, can vary strongly, influencing the transport of water in the rocks.

The effect of water saturation on hydraulic conductivity has been relatively well studied for soils. The hydraulic conductivities of unsaturated soils are highly dependent on water saturation (e.g., *Jury and Horton*, 2004) and can decrease by several orders of magnitude as water saturation decreases (*Mualem*, 1986; *Hillel*, 1998). Regarding rocks, many efforts have been devoted to elucidating the unsaturated flow in rock fractures (*Evans et al.*, 2000; *Indraratna and Ranjith*, 2001). In addition, considering the

enhanced recovery of oil and gas from reservoirs by injection of water, the relationship between water saturation and relative permeability has been evaluated under the condition that two or more fluids including water, oil and gas move simultaneously at high flow rates (e.g., *Bear*, 1972; *Dullien*, 1979; *Heaviside*, 1991). Furthermore, the results of hydraulic conductivity measured by field test often reflect water saturation of the rocks at the test site. These studies, however, did not aim to evaluate how the hydraulic conductivity of rock matrices varies with changing water saturation in the vadose zone, where water and air coexist in pores at low hydraulic gradient.

The present study focuses on a rock near the ground surface undergoing drying and infiltration. When pore water in a porous medium evaporates, water in larger pores migrates to smaller pores and the amount of water evaporated from the smaller pores is compensated (e.g., *Scherer*, 1990). This water transport is considered to be a result of "capillary pumping" (*Tsimpanogiannis et al.*, 1999), also known as "capillary transfer" (*Coussot*, 2000) or "capillary flow" (*Shokri et al.*, 2008). The first objective in the present study is to characterize how and how much pore water migrates during sandstone drying.

As drying proceeds, water saturation decreases. If water infiltrates into the partially saturated rock, some of air is entrapped in pore spaces. Previously reported values of entrapped (residual) gas saturation in sandstones typically range from 10 to 35% (e.g., *Pentland et al.*, 2011; *Zhou et al.*, 2011; *Krevor et al.*, 2012), but values beyond this range have also been found (*Suzanne et al.*, 2003; *Kumar et al.*, 2010). The total amount of air trapped in the rock depends on the water saturation prior to inflow of water ($S_{pre-flow}$). *Land* (1968) has proposed an empirical relationship between the entrapped air saturation and $S_{pre-flow}$. This entrapped air is known to affect the hydraulic conductivity (e.g., *Gupta and Swartzendruber*, 1964; *Lenhard and Parker*, 1987; *Faybishenko*, 1995; *Sakaguchi et al.*, 2005), and a model for estimating hydraulic conductivity under the occurrence of air entrapment has been proposed by *Lenhard and Parker* (1987). In this model, the total volume of entrapped air is estimated by the equation of *Land* (1968), and each pore size class is assumed to entrap air in proportion to its volume. By combining this assumption with *Mualem*'s (1976) relative hydraulic conductivity model, which was derived without considering air entrapment, an expression for relative hydraulic conductivity is derived. It should be noted that the equation of *Land* (1968) can only predict the total amount of entrapped air. Therefore, the amount of air entrapped as a function of pore size is unknown (*Parker and Lenhard*, 1987; *Fagerlund et al.*, 2008). With these points in mind, the second objective of the present study is to experimentally verify the real distribution of air entrapment in each

pore size class during drying-infiltration.

In this chapter, first the change in the size distribution of pore water was evaluated by "water-expulsion porosimetry" as a function of the degree of drying. Second, water was infiltrated in the sample adjusted to various $S_{pre-flow}$ by drying. After the infiltration at each value of $S_{pre-flow}$, the entrapped air saturation and hydraulic conductivity were measured. In addition, the size distributions of pore water (thus, those of entrapped air) were evaluated by the water-expulsion method. Based on the result, we discuss the mechanism by which water saturation affects hydraulic conductivity. We also compare the experimentally measured size distribution of pore water and "hydraulic conductivity – water saturation" relationship with those predicted by the relative hydraulic conductivity models and thereby evaluate the predictability of the models.

2.2. Experimental Methods

2.2.1. Sample Descriptions

Fontainebleau sandstone (France) was used in the experiment. The rock is composed of ~100% quartz, as confirmed by X-ray powder diffraction analysis. The quartz grains are well sorted, with approximate sizes of 200–300 μm (Fig. 2.1a). These properties are consistent with prior reports by *Bourbie and Zinszner* (1985) and *Doyen* (1988). The rock was cut into a cylinder (35 mm diameter and 9.5 mm length), mounted in a resin (Technovit 4004) to seal its lateral side, and used for the hydraulic conductivity measurement and water-expulsion porosimetry. Prior to the experiment, the sample was cleaned by rinsing and injecting ultrapure water (Milli-Q), followed by drying in an oven at 70°C. A sample was also taken for mercury intrusion measurement (diameter 14 mm and length 5.3 mm, no lateral seal).

The rock pores can be categorized as follows (Fig. 2.2): (1) total pores; (2) connected or open pores, which are open to the outside of the rock sample, comprised of transport pores and dead-end pores as defined below; (3) isolated or closed pores; (4) transport pores, which penetrate the sample from one end to another, providing a way for fluid to pass through the sample, not including pores that diverge from transport pores but come to a dead end; and (5) dead-end pores, which are connected to transport pores or directly to the surfaces of the sample but come to dead ends. The details of these categories and measurement procedures have been presented by *Yokoyama and Takeuchi* (2009). The total porosity of the sandstone was determined to be 7.4% from measurements of the bulk density (2.45×10^3 kg m^{-3}) and the solid density (2.65×10^3

kg m^{-3}). The open porosity of the sample is 6.3%, as determined by the difference between the water-saturated and dry weights. The saturated weight was obtained by following the procedure of *Yokoyama and Takeuchi* (2009). The transport porosity of the sample is 3.7%, as determined by measuring the volume of water expelled to one side of the sample by exerting a gas pressure of 1.6×10^5 Pa to the other side (corresponding to a capillary number of $< 3 \times 10^{-6}$).

Mercury intrusion porosimetry as well as the water-expulsion method measures the size distribution of entry pores (throats) through which they are accessible, which is commonly interpreted as a pore size distribution. The size distribution of pores measured by the mercury intrusion method (Fig. 2.1b) shows that pore radii generally range between a few hundreds of micrometers to a few micrometers, having a peak at approximately 5 μm. The presence of pores approximately 100 μm in radius may be attributable to the following reason. As is evident from Fig. 2.1a, pores with a width of ~200 μm, which were likely formed by detachment of quartz grains at the time of sample preparation, are present on the surface of the sample. The volumetric ratio of pores with a width of ~200 μm located on the sample surface can be calculated by $V_{p(200)} \times N \times a / (V \times \phi_{open}) \times 100$, where $V_{p(200)}$ (cm^3) is the volume of a ~200 μm width pore, N (cm^{-2}) is the number of 200 μm width pores per unit outer area of the sample, a is (cm^2) the outer area, V (cm^3) is the volume of sample, and ϕ_{open} is the open porosity. This expression shows that the volumetric ratio of 200 μm width pores is affected by the sample size and geometry (a/V). The sample used in the mercury intrusion measurement (no lateral seal) has $a = 5.3$ cm^2 and $V = 0.79$ cm^3. It can be estimated from the SEM image (Fig. 2.1a) that the number of ~200 μm width pores per unit outer area (1 mm^2) is roughly 1–2. If it is assumed that one cubic pore with a side of 200 μm is present per 1 mm^2, for the sample in the mercury intrusion method the volumetric ratio of 200 μm width pores can be calculated by $0.02^3 \times (1 \times 100) \times 5.3 / (0.79 \times 0.063) \times 100 = 8.5\%$, and this value agrees with that in Fig. 2.1b.
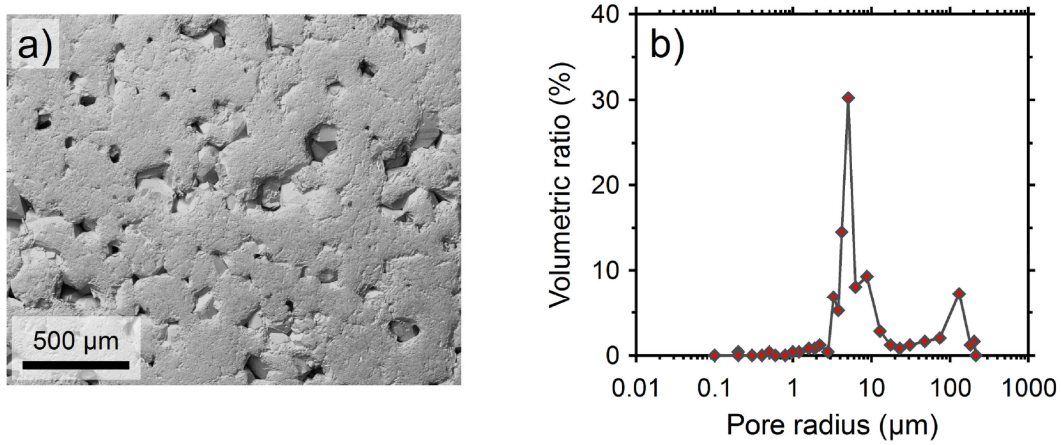
Fig. 2.1. (a) Scanning electron microscope image of a cut surface of Fontainebleau sandstone. (b) Pore size distribution of the rock measured by mercury intrusion porosimetry.
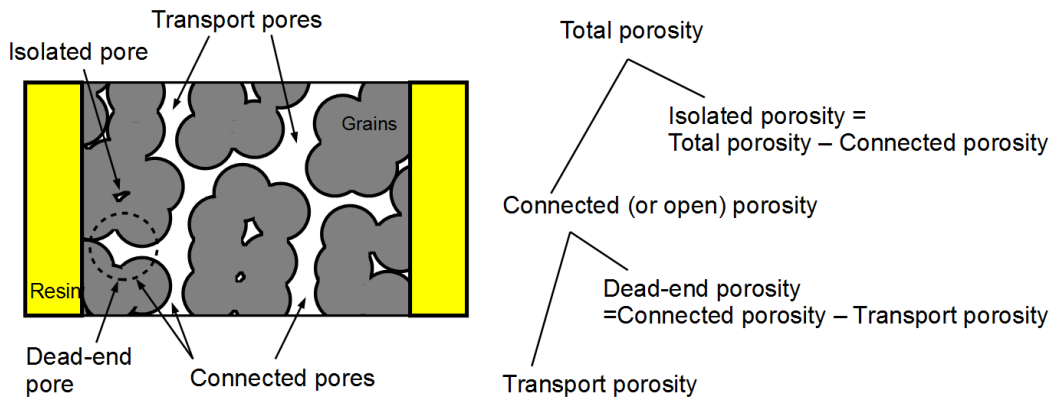
Fig. 2.2. Schematic of pore structure in a rock and the classification of pore types, modified after *Yokoyama and Takeuchi* (2009).

2.2.2. Drying of Pore Water and Adjustment of Pre-flow Saturation

The pore water preexisting before the inflow of new water and its saturation have been referred to as "old water" (*Turton et al.*, 1995; *GouetKaplan et al.*, 2009) and "initial water saturation" (*Heaviside*, 1991), respectively. Instead of using these terms, we use "pre-flow saturation" and its symbol "$S_{pre-flow}$" to specify water saturation after drying and prior to inflow. We also use water saturation after inflow, "S_{flow}", which is defined in detail in section 2.2.4. First, a sample was completely saturated with water. Ultrapure water was employed throughout the experiment. Pre-flow saturation was then adjusted by drying the water-saturated sample for different periods. In this process, the

cylindrical sample with a lateral seal was placed in a container (closed) with silica gel, as shown in Fig. 2.3a, so that the pore water evaporates from the top and bottom of the sample. The temperature and relative humidity inside the container were recorded by a portable weather meter (Kestrel4000, Mistral Instruments) every minute. The temperature and relative humidity during the adjustments of $S_{\text{pre-flow}}$ were 24–25°C and 43 ± 11%, respectively. To check the progress of drying, the sample was weighed by a digital balance with an accuracy of 0.0001 g at certain time intervals. $S_{\text{pre-flow}}$ was calculated by (the volume of water remaining in the sample after drying) ∕ (the volume of open pores) × 100. $S_{\text{pre-flow}}$ was adjusted to 100, 88, 70, 51, and 24%. For the adjustment of $S_{\text{pre-flow}}$ = 0%, the sample was heated in an oven at 70°C until a constant weight was attained.

2.2.3. Measurement of Size Distribution of Pore Water after Drying

To measure the volume of water in each pore size for different levels of water saturation, we employed water-expulsion porosimetry (also called "gas breakthrough experiment" (*Hildenbrand et al.*, 2002, 2004)). The measurement principle is similar to the "pressure plate method" used in soil physics to determine the capillary pressure-water saturation relationship (e.g., *Klute*, 1986), but the experimental setup differs. Fig. 2.3b is a schematic of the apparatus used for water-expulsion porosimetry, which is identical to that used by *Yokoyama and Takeuchi* (2009) except for the humidifying section newly added. When a differential gas pressure ΔP (Pa) is applied to the sample at a given water saturation, a capillary pressure arises in resistance to the ΔP. If the ΔP is larger than the capillary pressure, pore water is extruded from the upper surface of the sample (balloon in Fig. 2.3b). Assuming that pores have ideal cylindrical forms, the magnitude of ΔP required to expel water from the pore of radius r (m) is given by (*Gelinas and Angers*, 1986; *Innocentini and Pandolfelli*, 2001)

$$\Delta P = \frac{2\gamma \cos\theta}{r},$$
(2.1)

where γ is the surface tension of the liquid-gas interface (for water, $7.20 \times 10^{-2} - 7.22 \times 10^{-2}$ N m^{-1} at 24–25°C) and θ (degrees) is the contact angle between the solid and liquid. θ was assumed to be 0°, as in the works of *Gelinas and Angers* (1986) and *Innocentini and Pandolfelli* (2001). According to Eq. (2.1), water is expelled first from the largest pores, and water in smaller pores is progressively expelled with increasing ΔP. Thus, by measuring the volume of water expelled from the sample with incrementally increasing

ΔP and concurrently determining the pore radius, the pore water size distribution for transport pores can be obtained (balloon in Fig. 2.3b). The volume of water expelled at each ΔP was measured as follows: a dry tissue was weighed, the water discharged from the top of the sample was wiped with the tissue, the wet tissue was immediately weighed, and the pore water volume was calculated from the change in the weight of the tissue. This wipe was continued until water expulsion at each step ceased. To minimize the evaporative loss of pore water during the experiment, compressed air was passed through water before injection into the sample (humidifying section in Fig. 2.3b) and the relative humidity RH was raised to approximately 93%. A water trap in the humidifying section prevents water from flowing into the sample. Humidified air was also provided around the top of the sample to reduce evaporation.

In the measurement, $\Delta P = 6.0 \times 10^3$ Pa was first applied to the sample, and the volume of water in pores of >23 μm radii was determined. Next, ΔP was increased in incremental steps. The final ΔP was 1.6×10^5 Pa, equivalent to a pore radius of 0.90 μm. This procedure was repeated for various $S_{pre\text{-}flow}$ using the same sample, which allows the size distribution of pore water to be evaluated as drying proceeds. The pore size distribution measured by the mercury intrusion porosimetry (Fig. 2.1b) shows that the pores of >0.90 μm radii occupy 98% of the volume of open pores. Thus, by applying $\Delta P = 1.6 \times 10^5$ Pa, almost all water in transport pores can be expelled. To check the reproducibility, we performed the measurement in triplicate using the sample of $S_{pre\text{-}flow} = S_{flow} = 100\%$. The changes in the volume of each pore size in the three measurements were typically less than a volumetric ratio of ±1% but somewhat larger for the largest pores (>23 μm). This difference is attributable to the fact that the water wetting the upper surface of the sample in addition to that expelled from the pores were wiped at the first step of the water expulsion. We tried to reduce this effect by wiping off the sample surfaces with a wet tissue prior to exerting a gas pressure, but the effect remained. This issue can account for the larger volume of water in $S_{flow} = 67\%$ and 39% than $S_{flow} = 100\%$ (data shown in section 2.4.5.3). The effect of the evaporation of water from the rock and the tissue during the measurement was evaluated in the following manner. To determine the amount of water expelled at minimum evaporation, humidified air ($RH = 93\%$) at $\Delta P = 1.6 \times 10^5$ Pa was immediately applied to the saturated sample containing 0.5300 g of total pore water and 0.3224 g of water was collected. In contrast, if ΔP was increased stepwise using the humidified air (from $\Delta P = 6.0 \times 10^3$ Pa to 1.6×10^5 Pa; 13 steps), 0.3242 g of water was collected. Because the amounts of water collected were almost the same between the immediate and stepwise conditions, the evaporative loss from the tissue was small. However, at the end of the stepwise increase of ΔP, the

weight of the water remaining in the sample was 0.1456 g; thus, 0.0602 g (= 0.5300 − 0.3242 − 0.1456) of water evaporated at high *RH*. To evaluate the origin of evaporative loss, non-humidified air (*RH* = 43%) was used and ΔP was increased stepwise. A total of 0.3025 g of water was collected, and the evaporation was 0.1830 g. Although the evaporation at *RH* = 43% was significantly larger than that at *RH* = 93%, the difference in the total water collected was small (9.3% smaller at *RH* = 43%). Thus, even at *RH* = 100% the pore water size distribution is unlikely to change significantly from that at *RH* = 93%. Thus, the evaporative loss is mainly due to the evaporation of water at, for instance, dents along transport pores (these dents are categorized as dead-end pores and the water they contain is not expelled by applying gas pressure). This evaporation has little effect on the pore water size distribution for transport pores, which is most important for this study.
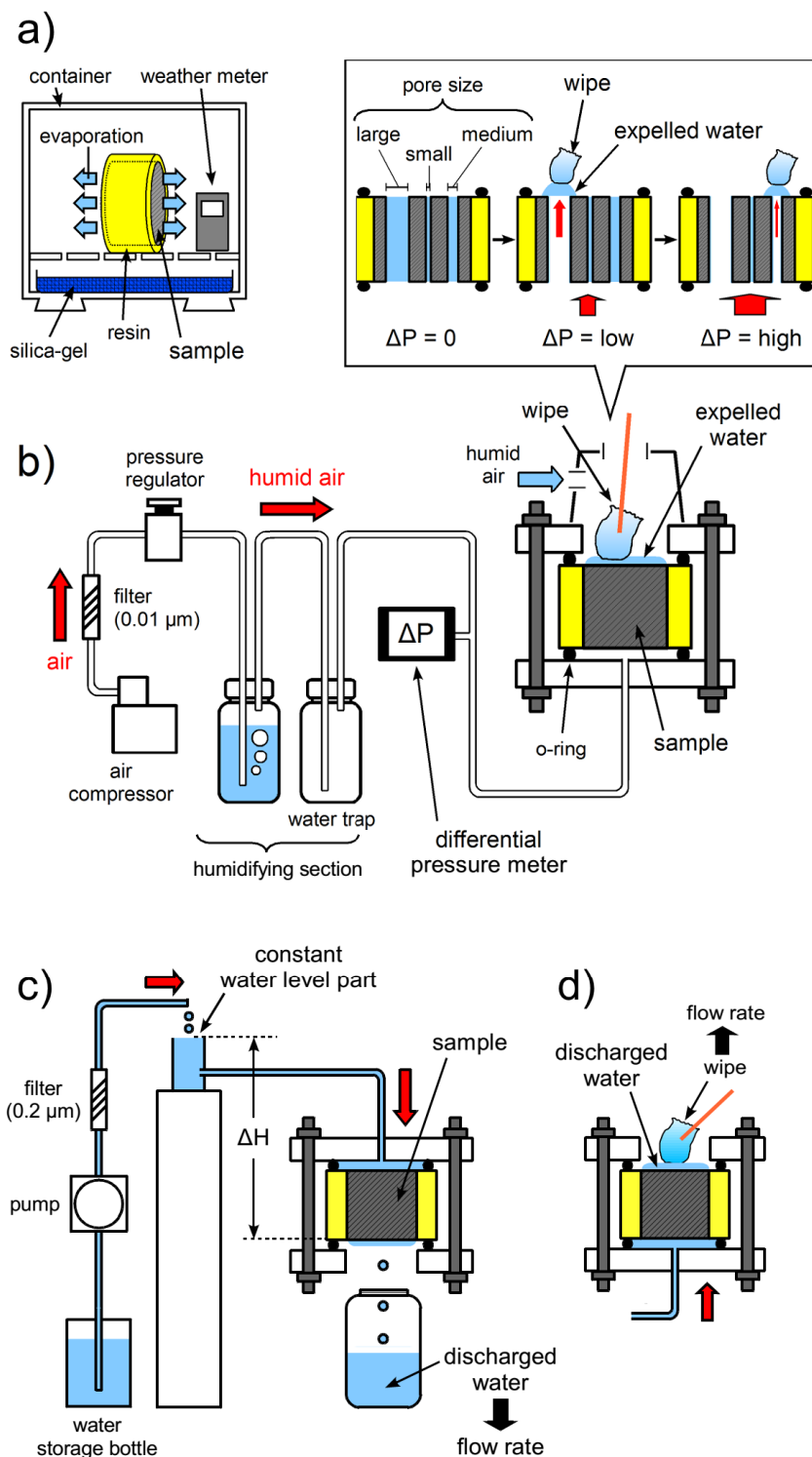
Fig. 2.3. (a) Schematic of the setup of the drying experiment. (b) Schematic of the water-expulsion porosimetry apparatus. The upper balloon shows the procedure for determining the pore water size distribution. (c), (d) Schematic of the apparatus used for measuring hydraulic conductivity. In the setting of (c), discharged water drops from the bottom of the sample. In the setting of (d), water is discharged from the top of the sample.

25

2.2.4. Measurement of Hydraulic Conductivity

Fig. 2.3c is a schematic of the apparatus used for measuring hydraulic conductivity. The apparatus is composed of a water storage bottle, pump, constant water level part, and sample holder, all of which are connected by Tygon tubing. The sample was installed at the sample holder immediately after adjusting $S_{pre\text{-}flow}$ (elapsed time was less than approximately 1 min). By continuously supplying water into the constant water level part so that water overflows, the water head difference ΔH was kept at 10 cm. When the time intervals of the measurement of flow rate were short (beginning 15 min from the onset of the experiment), we adopted the setup shown in Fig. 2.3d, in which the water discharged from the top of the sample was wiped with a pre-weighed tissue. This procedure was used because the effluent water did not fall down to the bottle and flow rate could not be measured within short time steps. When attempting to measure the flow rate on a time scale of hours, the experiment was first started using the setup shown in Fig. 2.3d. Fifteen minutes from the onset of the experiment, the sample holder was turned over (Fig. 2.3c) to prevent the pooling of effluent water by extending the time interval of flow rate measurement. We first evaluated how water saturation changes over 24 h. The sample was periodically removed from the holder, and its weight was measured. Water saturation significantly changed several minutes from the onset of the experiment, after which the changes became small (data shown in section 2.4.2). The temporal change in the flow rate showed a pattern similar to that of water saturation: the flow rate rapidly increased in the first several minutes, and then the variation became small. Thus, the flow reaches a quasi-steady-state within the first several minutes, which is maintained for at least a day. Based on these results, this paper focused on the flow at the quasi-steady-state. Water saturation at the quasi-steady-state flow is defined as "S_{flow}". The hydraulic conductivity at the S_{flow}, described as $K(S_{flow})$ (m s^{-1}), was calculated based on the following form of Darcy's law for unsaturated flow:

$$\frac{Q(S_{\text{flow}})}{A} = K(S_{\text{flow}})\frac{\Delta H}{L}, \tag{2.2}$$

where $Q(S_{\text{flow}})$ (m^3 s^{-1}) is the volumetric flow rate, A (m^2) is the cross-sectional area of the sample, and L (m) is the length of the sample. The measurement of S_{flow} and $K(S_{flow})$ was performed for each $S_{pre\text{-}flow}$. The saturated hydraulic conductivity of our sample, K_{sat}, was 1.7×10^{-7} m s^{-1}. From the repeated measurements of $K(S_{flow})$ (three

times at K_{sat} and twice at $K(39\%)$ and $K(67\%)$), the error in the determination of $K(S_{flow})$ was estimated to be approximately 2–7%. According to *Bourbie and Zinszner* (1985) and *Kieffer et al.* (1999), Fontainebleau sandstone with an open porosity of 6.3% has intrinsic permeabilities of 10^{-15}–10^{-13} m^2 with an average value of 2×10^{-14} m^2. Because the intrinsic permeability k and K_{sat} are related by $K_{sat} = k\rho g/\mu$ (where $\rho = 9.97 \times 10^2$ kg m^{-3} and $\mu = 8.9 \times 10^{-4}$ Pa s are the density and the viscosity of water at 25°C, respectively, and $g = 9.81$ m s^{-2} is the gravitational acceleration), k for our sample is calculated to be 1.6×10^{-14} m^2. Thus, the value for K_{sat} obtained in the present study is in the range of previously reported values.

2.2.5. Measurement of Size Distribution of Pore Water after Infiltration

To evaluate how air is entrapped and flow paths are formed during infiltration, the pore water size distribution was measured by water-expulsion porosimetry after the hydraulic conductivity was measured at each S_{flow}.

2.3. Theoretical Models

The experimentally measured $K\text{-}S_{flow}$ relationship and size distributions of pore water after infiltration can be compared with those predicted by the Mualem-van Genuchten (MVG) model and its modified version. The outline of the models and the procedure to determine the required parameters are described below.

2.3.1. MVG Model and its Modified Version

To predict the relationship between hydraulic conductivity and water saturation, many models have been proposed (e.g., *Burdine*, 1953; *Brooks and Corey*, 1964; *Mualem*, 1976; *van Genuchten*, 1980; *Kosugi*, 1996; *Assouline*, 2001). The MVG model, often used in soil physics and petroleum engineering, was derived based on *van Genuchten*'s (1980) capillary pressure-water saturation ($P_c\text{-}S_w$) relationship (also called water retention curve) and *Mualem*'s (1976) relative hydraulic conductivity model. Because P_c is linked with pore radius (r) by $P_c = 2\gamma\cos\theta/r$ if pores are assumed to be capillary tubes, the $P_c\text{-}S_w$ relationship and the pore size distribution can be interconverted (e.g., *D'Hollander*, 1979; *Kosugi*, 1994). To characterize the $P_c\text{-}S_w$ relationship, *van Genuchten* (1980) presented the following:

$$\overline{S}_w = \left[1 + \left(\alpha P_c\right)^{\frac{1}{1-m}}\right]^{-m} \tag{2.3}$$

where $\overline{S}_w$ is the effective water saturation calculated by $\overline{S}_w = \left(S_w - S_{wr}\right)/\left(1 - S_{wr}\right)$. Here, S_w $\left(S_{wr} < S_w \le 1\right)$ is the water saturation at a given P_c (different from S_{flow}) and S_{wr} is the (minimum) residual water saturation. The residual water may correspond to the water present at grain contacts as pendular rings (*Dullien*, 1989), in dead-end pores, and so strongly adsorbed onto mineral surfaces, that it does not contribute to water flow (e.g., *Luckner et al.*, 1989; *Brutsaert*, 2000). α (Pa^{-1}) and m ($0 < m < 1$) are fitting parameters related to the inflection point of the P_c-S_w curve and the broadness of the pore size distribution, respectively. m becomes larger for rock with a narrower pore size distribution. By applying Eq. (2.3) to the model of *Mualem* (1976), the relative hydraulic conductivity, K_r, is obtained as

$$K_r = \overline{S}_w^{\frac{1}{2}}\left[1 - \left(1 - \overline{S}_w^{\frac{1}{m}}\right)^m\right]^2 \tag{2.4}$$

This expression is the original MVG model for calculating K_r under various $\overline{S}_w$. It is assumed in the MVG model that at a given $\overline{S}_w$, the pores whose radii are smaller than a certain size are filled with water and larger pores are empty (*Mualem*, 1986). Using this assumption, the size distribution of pore water at the $\overline{S}_w$ is determined. When air entrapment occurs, some of the pores may not be always filled with water (even for relatively small pores), but this effect is not considered in the MVG model. A modified MVG model that accounts for the effect of entrapped air has been presented by *Lenhard and Parker* (1987). In this model, to estimate the total volume of entrapped air after water infiltrates at a given $S_{pre-flow}$, the following *Land* (1986) empirical model is used:

$$\overline{S}_{tot-air} = 1 - \overline{S}_{flow} = \frac{1 - \overline{S}_{pre-flow}}{1 + R\left(1 - \overline{S}_{pre-flow}\right)} \tag{2.5}$$

where $\overline{S}_{tot-air}$ is the total effective entrapped air saturation, $\overline{S}_{flow}$ is the effective flow-state saturation, and $\overline{S}_{pre-flow}$ is the effective pre-flow saturation. The bars on these saturations stand for scaling by $1 - S_{wr}$, e.g., $\overline{S}_{flow} = \left(S_{flow} - S_{wr}\right)/\left(1 - S_{wr}\right)$. R is defined as $R = \left(1/\overline{S}_{tot-air}^{max}\right) - 1$, where $\overline{S}_{tot-air}^{max}$ represents the maximum total effective entrapped air saturation. Because Eq. (2.5) can only provide information on the total volume of entrapped air, *Parker and Lenhard* (1987) introduced the assumption that each pore size has an identical water-to-entrapped-air-volume ratio. As a result, the

following equation, referred to as the modified MVG model in the present study, was obtained:

$$K_r = \overline{S}_{flow}^{\frac{1}{2}} \left[1 - \left(\frac{1 - \overline{S}_{flow}}{1 - \overline{S}_{pre-flow}} \right) \left(1 - \overline{S}_{pre-flow}^{\frac{1}{m}} \right)^m \right]^2$$ (2.6)

In this equation, one term originally contained in *Lenhard and Parker* (1987) is excluded because it becomes zero at any S_{flow} in the current experimental condition (the original expression is given in Appendix 2A).

2.3.2. Estimation of Model Parameters

Applications of the original and modified MVG models require estimation of m and S_{wr}. To predict the K-S relationship for infiltration process, these values must be estimated from the P_c-S_w curve for infiltration process (wetting P_c-S_w curve) because the shape of the curve measured in the drainage process (drainage P_c-S_w curve) typically differs from that in the infiltration process, which is referred to as a hysteresis. However, in our data, only the P_c-S_w curve for drainage process (displacement of water by a gas) is available. For such a case, *Parker and Lenhard* (1987) and *Lenhard et al.* (1991) have proposed a procedure to facilitate practical application of modified MVG model by minimizing the experimental data requirements. In this procedure, it is assumed that m and S_{wr} are the same between the infiltration and drainage processes but that α is different. This assumption has been used in various models addressing the hysteresis in the P_c-S_w relationship (*Kool and Parker*, 1987; *Luckner et al.*, 1989; *Haverkamp et al.*, 2002; *Canone et al.*, 2008). Therefore, the only data required are the drainage P_c-S_w curve of a water-saturated sample, and the value of $\overline{S}_{tot-air}^{\max}$ for the use of Eq. (2.5).

2.4. Results
2.4.1. Rate of Drying

The changes in $S_{pre-flow}$ and drying rate with time are shown in Fig. 2.4. The drying rate is expressed as the volume of evaporated water divided by twice the sectional area of the sample (evaporation occurred from the top and bottom of the sample). When a porous medium is dried from a water-saturated condition, the drying rate becomes approximately constant at relatively high value in the early stage of drying, which is

called "stage 1 evaporation" (*Lehmann et al.*, 2008; *Shokri et al.*, 2008). In this stage, overall drying rate is controlled by the humidity, temperature, and velocity of ambient air because each pore water is connected and evaporation occurs mainly near the external surface of the sample. After stage 1, following the intermediate region, the drying shifts to "stage 2 evaporation", in which water becomes completely disconnected and evaporation occurs from isolated water clusters. In this stage, the drying rate is controlled by the diffusion of vapor through the porous medium. As shown in Fig. 2.4, the drying rate is extremely high at the onset of drying, but this behavior seemed to be due to the evaporation of the water wetting the top and bottom surfaces of the sample. The drying rate constantly decreased during the experiment. After approximately 120 min passed, the drying rate is approximately inversely proportional to the square root of time. This fact implies that the drying of this period corresponds to the stage 2 (e.g., *Parlange et al.*, 1992; *Brutsaert and Chen*, 1995) and the drying before 120 min is mainly intermediate region.
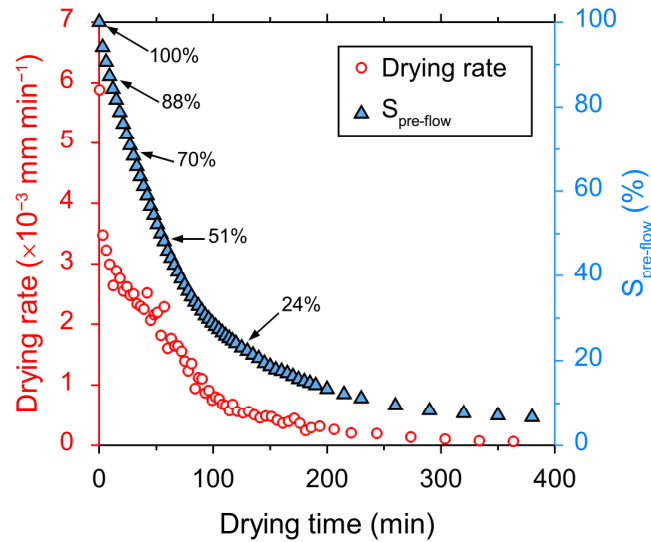
Fig. 2.4. Changes in drying rates and pre-flow saturation ($S_{\text{pre-flow}}$) with elapsed drying time.

2.4.2. Time Variations of Water Saturation and Flow Rate

Fig. 2.5a and b show the temporal changes in the volumetric flow rate and water saturation for the sample at $S_{pre\text{-}flow}$ = 0% and 51%. The volumetric flow rate and the water saturation increased rapidly in several minutes from the onset of the experiments. After several hours passed, these values were still changing but to a much smaller extent

and did not reach the values of water-saturated condition. A similar trend was also observed for the other $S_{pre\text{-}flow}$. Therefore, for each $S_{pre\text{-}flow}$, we adopted S_{flow} and $K(S_{flow})$ after 5–15 min had passed from the onset of the flow (quasi-steady-state).
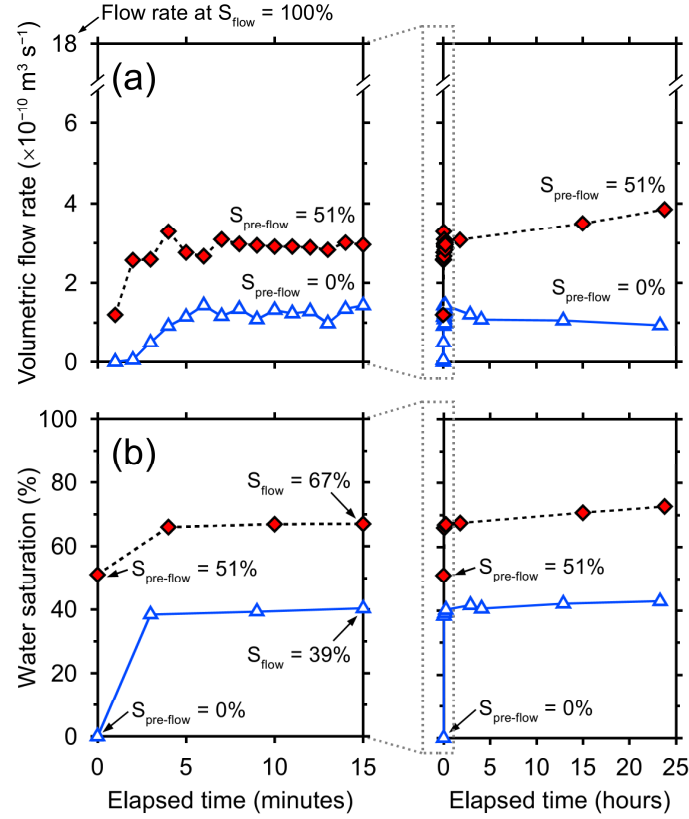
Fig. 2.5. Changes in volumetric flow rate (a) and water saturation (b) with elapsed experimental time at $S_{preflow}$ = 0% and 51%. For the first 15 min (the left side in Fig. 2.5a and b), the scale of the horizontal axis is in minutes, after which, the scale is in hours.

2.4.3. Relationship between Pre-flow Saturation and Air Entrapment

Fig. 2.6 shows a plot of S_{flow} versus $S_{pre\text{-}flow}$. S_{flow} decreased with decreasing $S_{pre\text{-}flow}$; these quantities for our sample were related by $S_{flow} = 0.64 \times S_{preflow} + 36$. The deviation of S_{flow} from the line of $S_{preflow} = S_{flow}$ corresponds to the amount of water newly infiltrated into empty (dried) pores. The gap between S_{flow} and S_{flow} = 100% is equivalent to the amount of entrapped air. As $S_{pre\text{-}flow}$ decreased, more water flowed into empty pores but more air was trapped, which is typical for the case of strongly water-wet systems (*Krevor et al.*, 2012). The amounts of air trapped in our sample were up to approximately 60% of open pore space at $S_{preflow}$ = 0%. *Suzanne et al.* (2003)

31

measured the amounts of trapped gas for Fontainebleau sandstones having various porosities and reported that the maximum values of trapped gas saturation were approximately 30, 50, and 70% for porosities of 21, 15, and 8.5%, respectively. *Kumar et al.* (2010) also estimated the maximum entrapped air saturation for Fontainebleau sandstone to be 50% and 29% for porosities of 14% and 18%. Based on a porosity close to that of our sample (6%), our result generally agrees with the value of *Suzanne et al.* (2003), although some differences at $S_{pre\text{-}flow} < 51\%$ exist. This difference may be due to the difference of fluids used (oil was used in *Suzanne et al.* (2003)). As for other rocks, previously reported maximum values of trapped CO_2 saturation for Berea sandstone (porosity = 22%) at $S_{pre\text{-}flow}$ = 15–90% were 35% (*Pentland et al.*, 2011; *Krevor et al.*, 2012) and that for Paaratte sandstone (porosity = 28–29%) at $S_{pre\text{-}flow}$ = 35–75% was 33% (*Krevor et al.*, 2012). These values are plotted with our results in Fig. 2.6 for comparison, although the gas species differ. Our trapped gas saturation data were distributed within the variation of the results of the other studies, but relatively high. The amount of gas entrapment increases as pore-to-throat ratio (aspect ratio) increases and the pore connectedness (coordination number) decreases (*Wardlaw and Cassan*, 1978; *Chatzis et al.*, 1983; *Lowry and Miller*, 1995). Previous research on Fontainebleau sandstone has shown that as porosity decreases, the connectedness of pores decreases and the pore-to-throat ratio increases (*Doyen*, 1988; *Lindquist et al.*, 2000; *Sok et al.*, 2002). These observations suggest that entrapped air saturation increases as the porosity of Fontainebleau sandstone decreases, which is consistent with the results shown in Fig. 2.6. The porosity of our sample is relatively low, which is likely to be a cause of the high amount of gas entrapment.
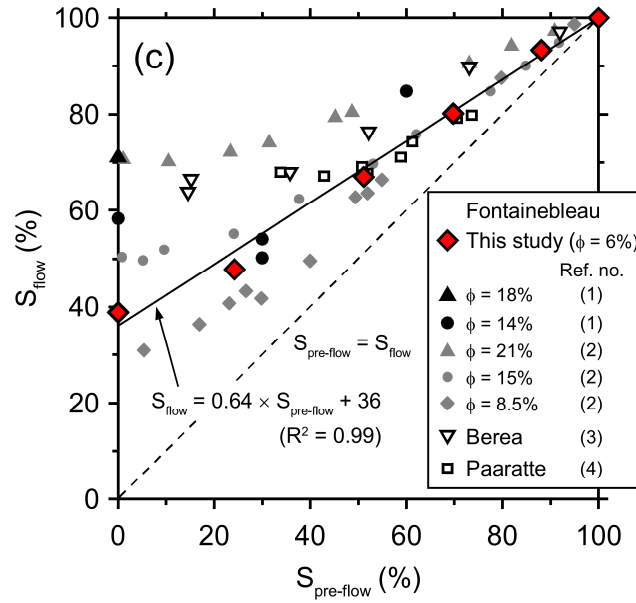
Fig. 2.6. Relationship between pre-flow saturation ($S_{pre-flow}$) and water saturation after infiltration at steady-state (S_{flow}). For comparison, the entrapped gas (air or CO_2) saturation data for Fontainebleau sandstones (*Kumar et al.*, 2010; Ref. (1)) (*Suzanne et al.*, 2003; Ref. (2)), Berea sandstone (*Pentland et al.*, 2011; Ref. (3)), and Paaratte sandstone (*Krevor et al.*, 2012; Ref. (4)) are shown. The data by *Suzanne et al.* (2003) were obtained in oil/gas systems, and the other data were obtained in water/gas systems. ϕ stands for the rock porosity.

2.4.4. Relationship between Water Saturation and Hydraulic Conductivity

The relative hydraulic conductivity K_r, the ratio of $K(S_{flow})$ to K_{sat}, is plotted against S_{flow} (also, $S_{pre-flow}$) in Fig. 2.7. As S_{flow} ($S_{pre-flow}$) decreases, K_r monotonically decreases by more than one order of magnitude, except for S_{flow} = 39% ($S_{pre-flow}$ = 0%). K_r are well correlated with S_{flow} by the relationship of $K_r = S_{flow}^n$, where n is approximately 3 to 5 (best fit: $n = 4.5$) and S_{flow} is the fraction (here, not percentage).
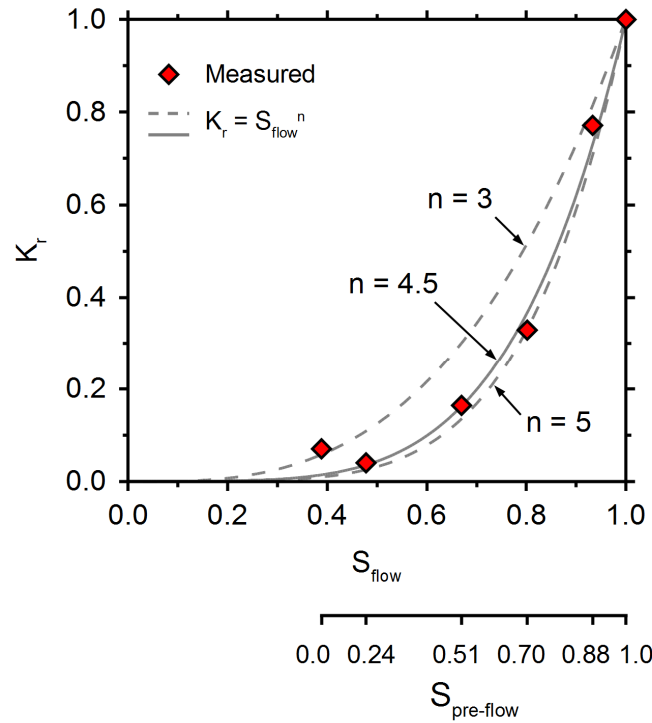
Fig. 2.7. Measured relative hydraulic conductivity (K_r) as a function of $S_{pre\text{-}flow}$ and S_{flow}. The solid and dashed curves show power-law functions of S_{flow}, $K_r = S_{flow}^n$, where the curves of n =3, 5, and 4.5 (best fit) are depicted.

2.4.5. Size Distributions of Pore Water after Drying and Infiltration

Fig. 2.8 show the result of the water-expulsion porosimetry at various $S_{pre\text{-}flow}$ and S_{flow}. The volumetric ratios (%) are calculated by (volume of water expelled from pores of each size) / (total volume of open pores) × 100. Note that sum of each volumetric ratio does not become 100% because water in dead-end pores is not expelled by the water-expulsion porosimetry. These data provide information on how the distribution of pore water changes by drying and infiltration.
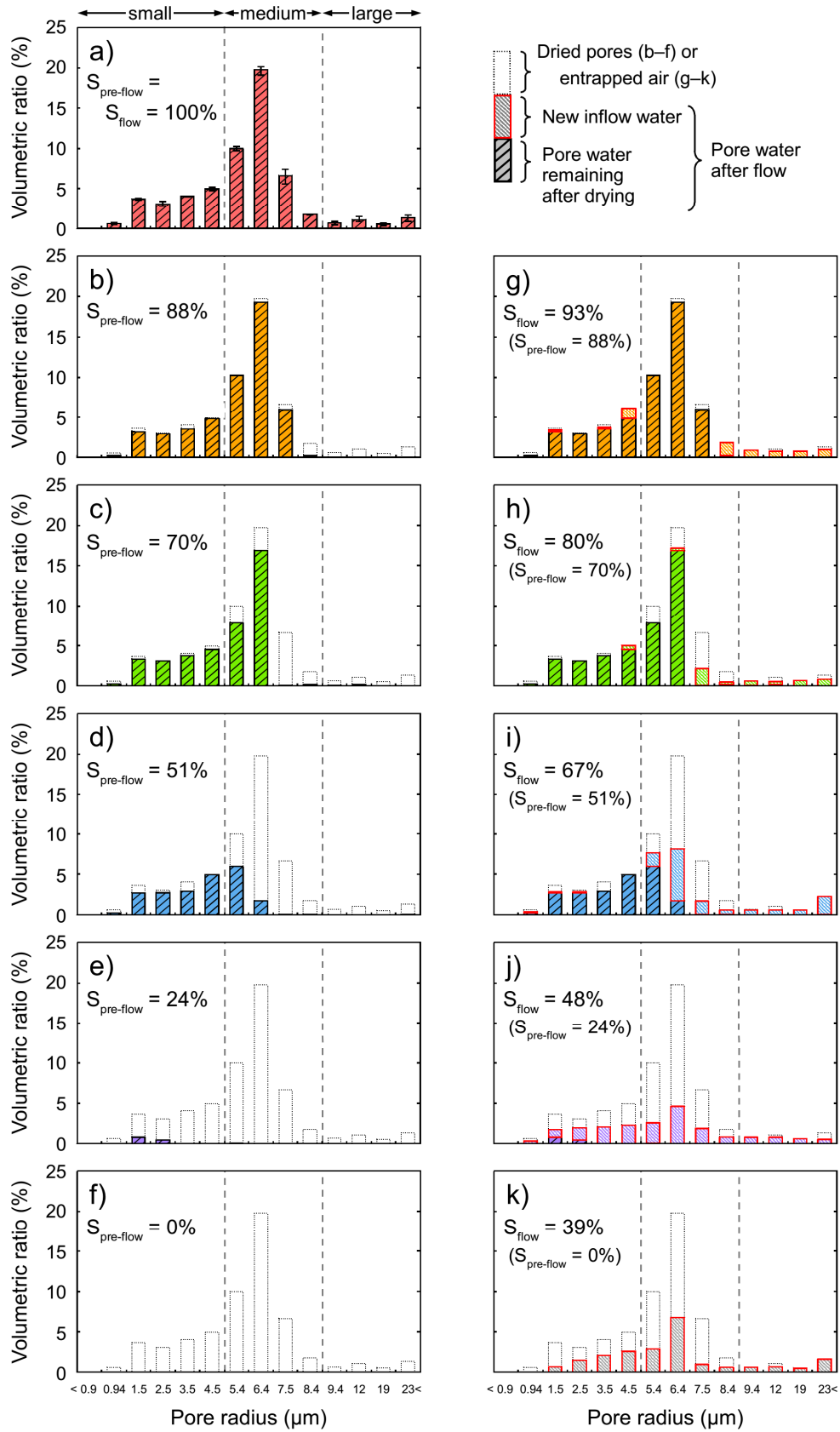
Fig. 2.8. Size distribution of pore water at various $S_{pre\text{-}flow}$ and S_{flow} obtained by water-expulsion porosimetry. (a) pore size distribution of watersaturated sample, corresponding to bulk structure of the sample. (b−f) results after drying. Solid bars with diagonal lines correspond to the volume of water remaining after drying. (g−k) results after flow. The light-colored solid bar corresponds to the volume of new inflow water, while the dotted frame (empty) corresponds to the volume of entrapped air.
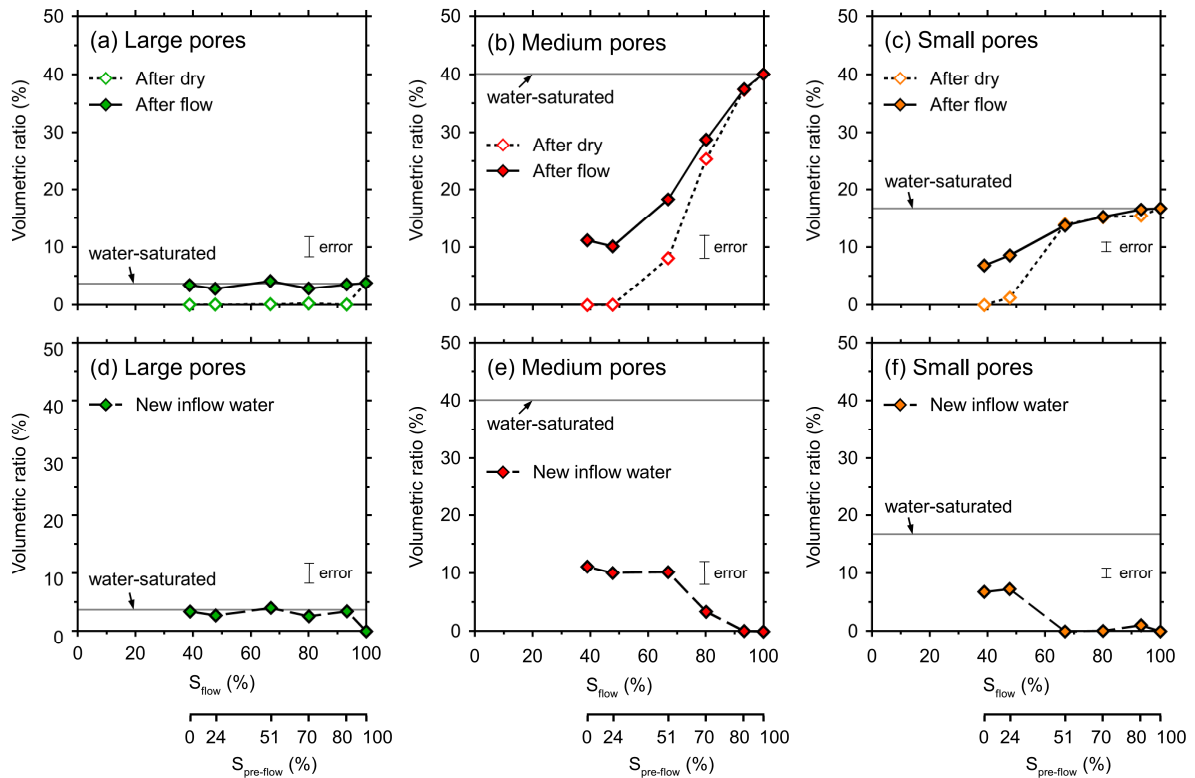
Fig. 2.9. Volumetric ratio of pore water after drying and after flow plotted against S_{flow} ($S_{pre\text{-}flow}$) for large pores (a), medium pores (b), and small pores (c). Volumetric ratio of new inflow water plotted against S_{flow} ($S_{pre\text{-}flow}$) for large pores (d), medium pores (e), and small pores (f), calculated by subtracting the value after drying from that after flow. Errors were estimated from the reproducibility of the water-expulsion measurements.

2.4.5.1. Bulk Pore Structure

Fig. 2.8a shows the pore size distribution of water-saturated sample, representing bulk pore structure of the sample. The radii of pores are mostly 1–20 μm, and there is a peak at approximately 6 μm. Although the water-expulsion method yields the size distribution of transport pores and the mercury intrusion method provides that of open

pores, the results from the two generally agree well (Fig. 2.1b and 2.8a), with the exception of the peak at approximately 100 μm. As described in section 2.2.1, the peak at approximately 100 μm in the mercury intrusion method seems to be a result of detached grains at the sample surfaces. For the sample used in the water-expulsion method (lateral side sealed, $a = 9.4$ cm^2 and $V = 8.9$ cm^3), the volumetric ratio of 200 μm width pores is calculated to be 1.3%. This value is consistent with the value of >23 μm pores shown in Fig. 2.8a.

In the following discussion, we categorize the pores into three groups; pores with mean radii of ≥9.4 μm, 8.4–5.4 μm and ≤4.5 μm are defined as "large pores", "medium pores" and "small pores", respectively.

2.4.5.2. Pore Water after Drying

Fig. 2.8b–2.8f show the size distributions of pore water at $S_{pre-flow}$ = 88, 70, 51, 24, and 0%. The changes of the amount of water in large, medium, and small pores as a result of drying are shown in Fig. 2.9a, b, and c, respectively. These results reveal that the decrease of pore water during drying depends on pore size. The large pores lost water almost completely in the early stage of drying, even at $S_{preflow}$ = 88% (Fig. 2.9a). The medium pores continuously lost water with decreasing $S_{preflow}$ over a wide range of $S_{preflow}$. At $S_{preflow}$ = 88–51%, the loss of water in medium pores dominates the overall loss of pore water. The loss of water in small pores at $S_{pre-flow}$ = 100–51% was small but increased rapidly as $S_{pre-flow}$ further decreased. The results ensure the occurrence of capillary flow; its concept is generally explained by a simple model modified after *Scherer* (1990) as follows (Fig. 2.10a–c). When the evaporation of pore water occurs, menisci are formed in pores and capillary pressure arises. The capillary pressure difference due to the variation in pore sizes induces the flow of water toward smaller pore (from Fig. 2.10a to 2.10c). Thus, the size of pores filled with water progressively becomes smaller as drying continues. Although the actual pore structure of the sandstone is more complicated than that described in Fig. 2.10, the capillary flow during drying accounts for the results of water-expulsion porosimetry well (Fig. 2.8b–f and Fig. 2.9a–c).
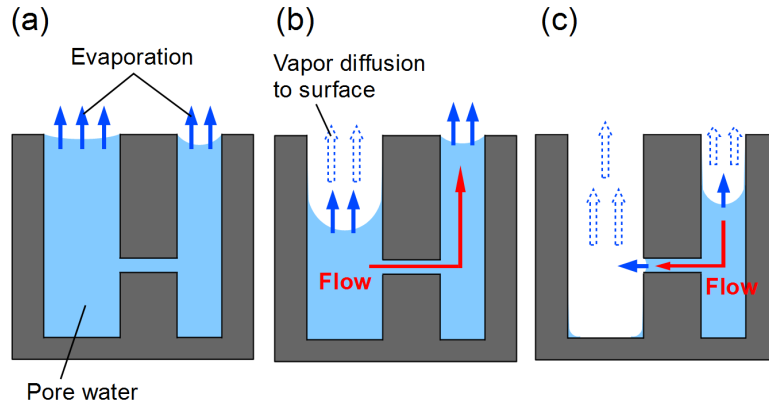
Fig. 2.10. Schematic of the drying process of a simplified porous medium having three different pore sizes, showing how water moves and how the size of pore water changes as drying proceeds.

2.4.5.3. Pore Water after Infiltration

Fig. 2.8g–k show the size distributions of pore water after the flow at S_{flow} = 93, 80, 67, 48, and 39%, respectively, corresponding to $S_{pre-flow}$ = 88, 70, 51, 24, and 0% before infiltration. The total volume of water after the flow can be separated to the fractions of preexisting water and new inflow water. The difference in the size distributions of pore water before and after the flow (e.g., for $S_{pre-flow}$ = 88%, the difference between Fig. 2.8g and Fig. 2.8b), shown as bars with light colors (red outer frame), corresponds to the volume of new inflow water. The total volumes of water in large, medium, and small pores after the flow are plotted against S_{flow} in Fig. 2.9a, b, c, respectively, and the volumes of new inflow water in each pore size class are plotted in Fig. 2.9d, e, f. Regarding the large pores, the volume of new inflow water was almost equal at any S_{flow} (Fig. 2.9d). Therefore, the large pores lost almost all water by drying even at high $S_{pre-flow}$ but were saturated again by new inflow water at any S_{flow}. Regarding the medium pores, when a relatively high amount of preexisting water remained in the pores ($S_{pre-flow}$ > 70%), the amount of new inflow water was small (Fig. 2.9e). Thus, water mainly infiltrated by connecting the preexisting water and did not invade into the empty (dried) pores. More empty pores were refilled by water at $S_{pre-flow}$ < 70%, but the amount of new inflow water did not exceed a volumetric ratio of ~10% (~25% of medium pores) at any $S_{pre-flow}$ owing to the occurrence of air entrapment. A similar trend was observed for the small pores (Fig. 2.9f), but because the small pores do not lose water easily by drying, new inflow water began to increase only when water saturation considerably fell. In addition, ~40% of the small pores were filled with new

inflow water, which was somewhat larger than that for the medium pores. Based on these results, the way flow paths are formed is affected both by the pore size distribution of water before flow and the pore size dependence of air entrapment.

2.5. Discussion

2.5.1. Cause of the Decrease of Hydraulic Conductivity

If water readily flows in empty pores, all pores will be saturated by new inflow water as time passes. However, small changes in flow rate and water saturation with time after several minutes from the onset of the experiment (Fig. 2.5a and b) indicate that stable flow paths as the result of air entrapment were formed. In Fig. 2.7, K_r generally decreases with decreasing S_{flow}. Because almost the same amount of water flows through large pores at any S_{flow} (Fig. 2.9a), the flow paths due to large pores are unlikely to be related to the decrease of K_r. The decrease of the volume of water in small pores at $S_{flow} = 100$–80%, where K_r significantly decreases, was small (Fig. 2.9c). In addition, the flow rate in small pores is smaller than that in medium pores under the same differential pressure, according to the Hagen-Poiseuille's law, which describes flow in a smoothwalled cylindrical pipe: $Q = \left(\pi r^4/8\mu\right)\left(dP/dl\right)$ (volume flow rate Q, pressure gradient dP/dl). Therefore, the flow in small pores is also unlikely to be related to the rapid decrease of K_r. In contrast to the large pores and small pores, medium pores lost significant water at $S_{flow} = 100$–80% (Fig. 2.9b), which suggests that the considerable decrease in K_r at $S_{flow} = 100$–80% is induced by the decrease of water in medium pores. At S_{flow} lower than 80%, the change of K_r gradually becomes smaller (Fig. 2.7). This change appears to be because water always comes into medium pores as much as 25% even if water in medium pores is almost completely lost by drying (Fig. 2.9b and e). K_r (39%) was larger than K_r (48%), contradicting the overall trend of K_r-S_{flow}. In Fig. 2.9b, the amount of water in medium pores before the flow was zero at both $S_{flow} = 39\%$ and 48%, but that after the flow was larger at $S_{flow} = 39\%$ than at $S_{flow} = 48\%$. This finding suggests that at $S_{flow} = 48\%$ the preexisting pore water prevents new water from entering into empty medium pores, resulting in smaller value of $K_r(48\%)$.

2.5.2. Comparison of the Size Distributions of Pore Water and Hydraulic Conductivities Obtained by Model and Experiment

To evaluate the predictability of the K-S relationship in the original and modified MVG models and the validity of the size distribution of pore water assumed in the

models, we compare the results obtained from the models with those from the experiments. Fig. 2.11 shows the P_c-S_w relationship obtained for the water-saturated sample by the water-expulsion porosimetry. Fitting Eq. (2.3) to the P_c-S_w curve yielded m = 0.82 and α = 4.2 × 10^{-5} Pa^{-1}, assuming S_{wr} = 0.40 which was the water saturation at the maximum P_c. This assumption for S_{wr} was employed for consistency with the estimate of other S_{wr} (see below). Even if S_{wr} is regarded as a fitting parameter, almost the same result is obtained (m = 0.84, α = 4.3 × 10^{-5} Pa^{-1}, and S_{wr} = 0.43). The value of $\overline{S}_{tot-air}^{max}$ was 0.65, which corresponded to R = 0.55 in Eq. (2.5). In calculating $\overline{S}_{pre-flow}$ and $\overline{S}_{flow}$ (= $(S - S_{wr})/(1 - S_{wr})$, where S is $S_{pre-flow}$ or S_{flow}), if S_{wr} is regarded as a constant and the value obtained from the saturated sample is used, $\overline{S}_{pre-flow}$ and $\overline{S}_{flow}$ become negative at low $S_{pre-flow}$ and S_{flow}. Although this case is indicated by *Lenhard et al.* (1991), the solution is not provided. Therefore, we regarded S_{wr} in the numerator of $(S - S_{wr})/(1 - S_{wr})$ as a variable. That is, the numerator and the denominator correspond to the volume of water in transport pores and the total volume of transport pores, respectively. S_{wr} was determined from the results of water-expulsion measurement after each infiltration and drying process, and its values are summarized in Table 2.1. S_{wr} decreases with decreasing $S_{pre-flow}$, which indicates that the amount of evaporation of residual water depends on $S_{pre-flow}$.

First, we consider the MVG model. The size distribution of pore water at S_{flow} = 39% ($S_{pre-flow}$ = 0%) obtained by the assumption in the MVG model is shown in Fig. 2.12b, which can be compared with the experimental result (Fig. 2.12a). In addition, to evaluate how the volume of water at each pore size class changes with S_{flow}, the volumetric ratios of water in large, medium, and small pores obtained by the model and the experiment are shown in Fig. 2.12d, e, and f, respectively. For the medium pores at $S_{flow} \geq 67\%$ (Fig. 2.12e), the experimental result is well reproduced by the model. However, for large pores (Fig. 2.12d) and small pores (Fig. 2.12f), the results from the experiment and model differ. The MVG model presumes that the large pores are empty at low S_{flow}, but the experimental result showed that they are always filled with new inflow water at any S_{flow}. The model also presumes that the small pores are filled with water at any S_{flow}, but the experimental result revealed that the volume of entrapped air increases with decreasing S_{flow}. Despite these differences, the relative hydraulic conductivities calculated from Eq. (2.4) with an assumption of $\overline{S}_w = \overline{S}_{flow}$ agree well with those from the experiment (Fig. 2.13). This accordance is likely due to the agreement for the volume of water in the medium pores by which hydraulic conductivity is controlled. However, it is unclear whether this agreement holds true for

any pore structure, and we cannot say that the MVG model generally has high predictability of the flow behavior under air entrapment.

Next, we consider the modified MVG model. The values of $\overline{S}_{flow}$ at each $\overline{S}_{pre-flow}$ obtained in the experiment generally accord with those calculated by the *Land*'s (1986) equation (Table 2.1). Therefore, the assumption in the modified MVG model for the use of *Land*'s equation seems to be successful. The model also predicts well the *K-S* relationship obtained in the experiment (Fig. 2.13). Fig. 2.12c shows the size distribution of pore water at $S_{flow} = 39\%$ ($S_{pre-flow} = 0\%$) assumed in the modified MVG model. In the model, pores were first filled with water from smaller pores to larger ones until water saturation reaches $\overline{S}_{pre-flow}$, after which the total volume of new inflow water is distributed to remaining empty pores as each pore size has the same water-to-entrapped-air-volume ratio. The volumetric ratios of water in three pore size classes obtained by the model (Fig. 2.12d, e, f) generally agree well with the experimental values, which accounts for the fact that K_r calculated from the model predicts the experimental values well. However, there are some differences in the details; for example, the modified MVG model predicts that only a portion of the large pores is filled with water, but the experimental result shows that the large pores were always refilled with new inflow water.

Although the modified MVG model successfully predicted the hydraulic conductivity and the size distribution of pore water for the sandstone used in this study, *Fagerlund et al*. (2008) reported the disagreement between the prediction based on the assumption of *Parker and Lenhard* (1987) and the experimental result using a sand column, mentioning that the non-wetting phase may be entrapped in a specific pore size (they used nonaqueous liquid rather than air). This finding implies that the nature of entrapment has diversity. There are various factors that might affect the size distribution of entrapped air and thereby the predictability of *K-S* relationship by the modified MVG model, such as the pore structure, mineral composition, magnitude of hydraulic head difference, and drying-infiltration history. It would be important to evaluate how these factors affect the behavior of air entrapment using an experiment such as that used in the present study, which can provide fundamental information to validate or improve the underlying assumption and predictability of the model.

Table 2.1. Measured and calculated effective flow-state saturation and relative hydraulic conductivities.

$S_{pre\text{-}flow}$	$\bar{S}_{pre\text{-}flow}$	$S_{wr}{}^{a}$	S_{flow}	$\bar{S}_{flow}$		$S_{wr}{}^{c}$	K (meas)^{d}	K_r (meas)	K_r / ratio^{e}	
				Meas.	Calc.^{b}				MVG	Modified MVG
1.00	1.00	0.40	1.00	1.00	1.00	0.40	1.71	1.00	1.00	1.00
0.88	0.87	0.35	0.93	0.95	0.88	0.36	1.32	0.77	0.79 / 1.0	0.79 / 1.0
0.70	0.66	0.30	0.80	0.77	0.71	0.33	0.56	0.33	0.38 / 1.2	0.39 / 1.2
0.51	0.37	0.29	0.67	0.60	0.53	0.31	0.28	0.16	0.17 / 1.0	0.19 / 1.1
0.24	0.02	0.23	0.48	0.35	0.36	0.26	0.07	0.04	0.03 / 0.8	0.07 / 1.8
0.00	0.00	0.00	0.39	0.38	0.35	0.16	0.12	0.07	0.04 / 0.6	0.08 / 1.1

^{a} Residual water saturation at each $S_{pre\text{-}flow}$.

^{b} Calculated from the *Land* (1968) model.

^{c} Residual water saturation at each S_{flow}.

^{d} Unit is $\times 10^{-7}$ m s^{-1}.

^{e} In each cell, the relative hydraulic conductivity calculated from the model (Eq. (2.4) for the MVG model, Eq. (2.6) for the modified MVG model) is shown on the left side, and the proportion of the calculated value to the measured value (expressed as a ratio) is shown on the right side.
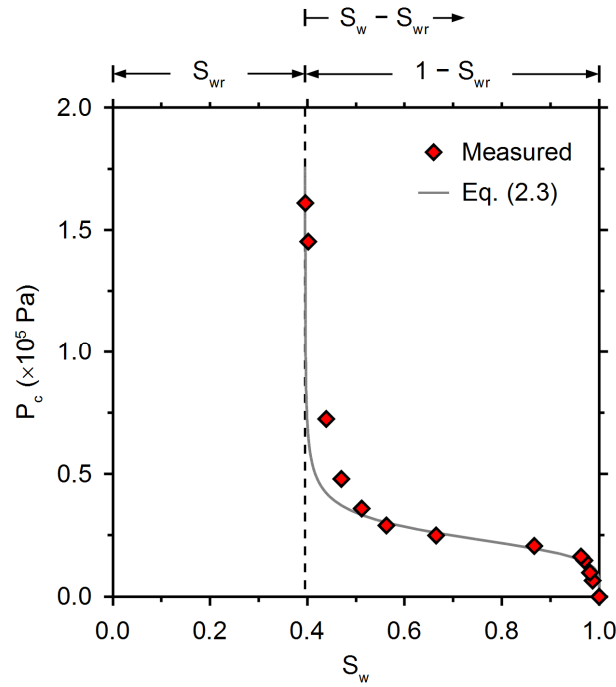
Fig. 2.11. Relationship between capillary pressure (P_c) and water saturation (S_w) during the water-expulsion experiment applied to the water-saturated sample. The grey curve

was fitted according to the model of van Genuchten.
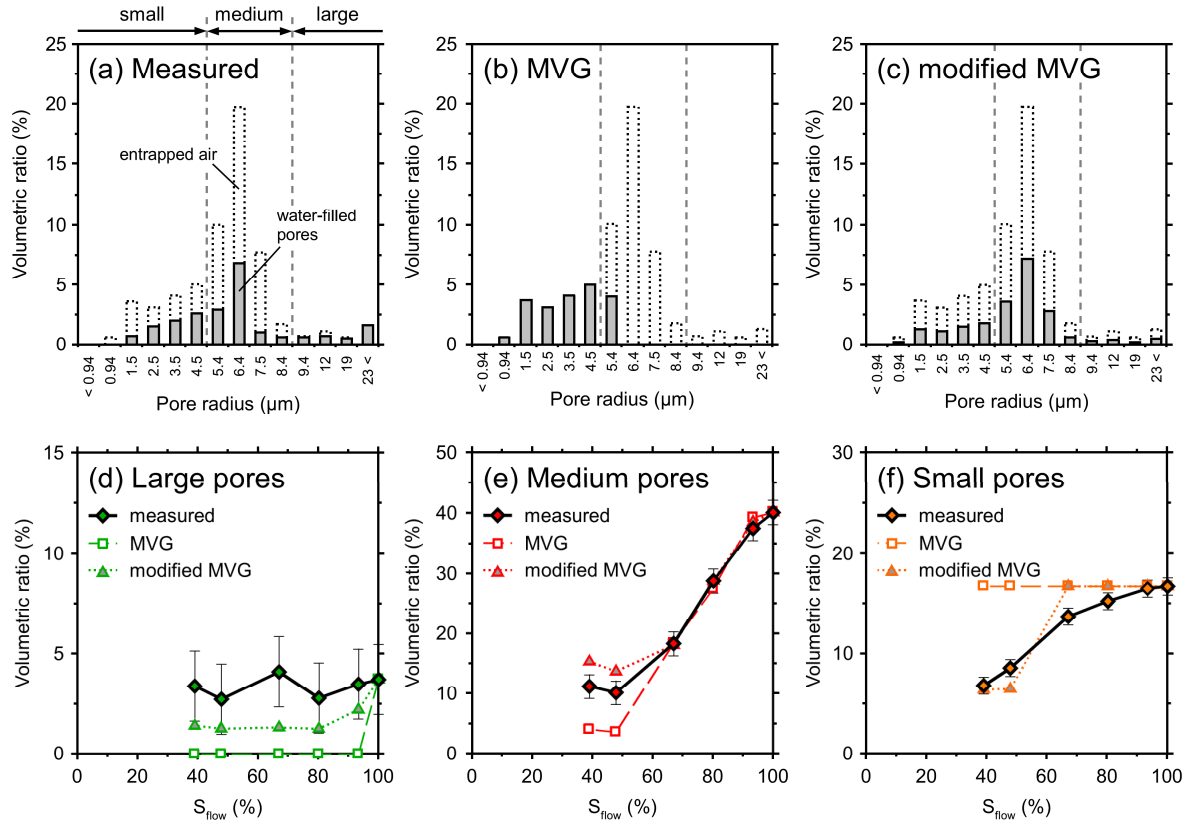
Fig. 2.12. Size distribution of pore water after flow at S_{flow} = 39% measured by the water-expulsion porosimetry (a) and calculated based on the MVG model (b) and the modified MVG model (c). Comparison of the volumetric ratios of pore water after flow obtained by the experiment, the MVG model, and the modified MVG model for large (d), medium (e), and small (f) pores, respectively. Errors were estimated from the reproducibility of the water-expulsion measurements.
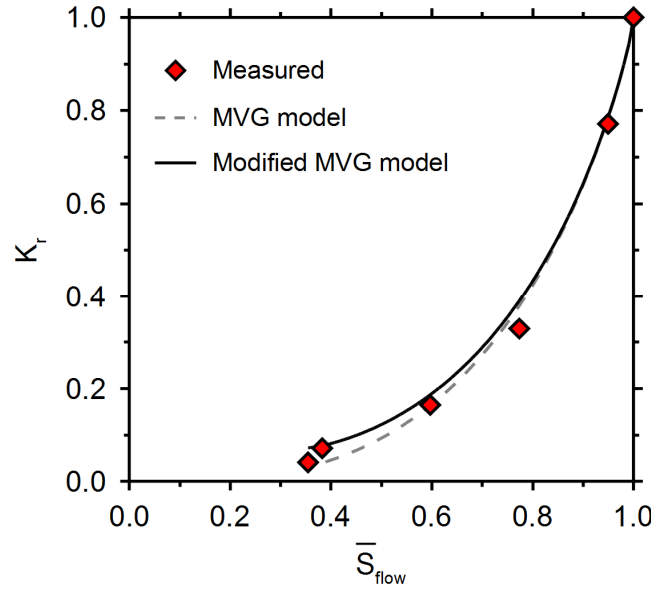
Fig. 2.13. K_r as a function of effective flow-state saturation ($\overline{S}_{flow}$); experimentally measured values and those predicted by the original MVG model (dashed line) and the modified MVG model (solid line). Here, $S_{pre-flow}$, S_{flow} and $\overline{S}_{flow}$ are expressed as fractions.

2.6. Conclusions

Water transport during drying-infiltration processes was characterized using Fontainebleau sandstone, having pore radii ranging from 1–20 µm with a peak around 6 µm. First, the change in the size distribution of pore water with the progress of drying was evaluated by water expulsion porosimetry. Next, water was infiltrated in the sample adjusted to various degrees of drying, and the entrapped air saturation and hydraulic conductivity were measured. In addition, the size distributions of pore water and entrapped air after the flow were evaluated. Finally, we compared the experimentally measured pore water size distribution and $K\text{-}S$ relationship using the MVG model and its modified version, accounting for air entrapment. The results and interpretations were as follows:

(1) As drying proceeded, the volume of pore water decreased successively from larger pores to smaller ones, ensuring the occurrence of capillary flow.

(2) The entrapped air saturation increased and hydraulic conductivity decreased with decreasing $S_{pre\text{-}flow}$. The amounts of entrapped air were up to approximately 60% of open pore space. The hydraulic conductivity and water saturation (S_{flow}) were related by approximately $K\left(S_{flow}\right) \propto S_{flow}^{4.5}$.

(3) If the pore sizes were classified as large ($\geq$ 9.4 µm), medium (8.4–5.4 µm) and small ($\leq$ 4.5 µm), preferential air entrapment with decreasing S_{flow} was observed for the medium pores. The significant decrease of $K(S_{flow})$ at S_{flow} = 100–80% seemed to be mainly caused by the entrapment of air in the medium pores.

(4) The measured K-S relationship agreed well with those predicted by the original and modified MVG models. This appeared to be because for medium pores the amounts of water and entrapped air at each S_{flow} determined by the water-expulsion method were well reproduced by both the original and modified MVG models. However, for large pores and small pores, some differences were observed between the experiment and the models.

The above results showed that the ease of water infiltration and air entrapment depends on pore size. Advance in such knowledge will contribute to the understanding of the transport of water in the Earth's surface.

Appendix 2A

In Eq. (2.6), one term originally contained in *Lenhard and Parker* (1987) is excluded because it becomes zero in the current experimental condition. Consider the situation in which water infiltrates into the sample at a given $\bar{S}_{pre-flow}$ with air entrapment. The effective water saturation and effective entrapped air saturation are defined as $\bar{S}_w$ and $\bar{S}_a$, respectively. At $\bar{S}_w = \bar{S}_{pre-flow}$, $\bar{S}_a$ equals to zero, as shown in Fig. 2.A1a (*Parker and Lenahrd*, 1987). As infiltration proceeds, $\bar{S}_w$ and $\bar{S}_a$ gradually increase; water infiltrates first into the smallest empty pores, and the size of water-filled pores gradually increases. Because the capillary pressure P_c and the pore radius r are correlated by $r = 2\gamma \cos\theta / P_c$, P_c gradually decreases as the infiltration proceeds ($\bar{S}_w$ increases) (Fig. 2.A1b). As infiltration further proceeds (Fig. 2.A1c), the P_c-$\bar{S}_w$ curve approaches the end point (i.e., P_c = 0) and $\bar{S}_a$ and $\bar{S}_w$ become $\bar{S}_{tot-air}$ and $1 - \bar{S}_{tot-air}$, respectively. The relationship between relative hydraulic conductivity K_r and $\bar{S}_w$ proposed by *Lenhard and Parker* (1987) is

$$K_r = \bar{S}_w^{\frac{1}{2}} \left[1 - \left(1 - \frac{\bar{S}_{tot-air}}{1 - \bar{\bar{S}}_{pre-flow}} \right) \left(1 - \bar{\bar{S}}_w^{\frac{1}{m}} \right)^m - \left(\frac{\bar{S}_{tot-air}}{1 - \bar{\bar{S}}_{pre-flow}} \right) \left(1 - \bar{\bar{S}}_{pre-flow}^{\frac{1}{m}} \right)^m \right]^2 \tag{2A.1}$$

where $\bar{\bar{S}}_w$ is the apparent saturation and is expressed as $\bar{\bar{S}}_w = \bar{S}_w + \bar{S}_a$. In our experiment, the size distribution of pore water was determined after water percolated into the sample and flow rate reached quasi-steady-state. In this case, P_c is regarded as

almost zero (the end point in the P_c-$\bar{S}_w$ curve). $\bar{\bar{S}}_w = 1$ is then satisfied, and $1 - \bar{S}_{tot-air}$ becomes equal to $\bar{S}_{flow}$ (Fig. 2.A1c). Therefore, the term $1 - \bar{\bar{S}}_w^m$ in Eq. (2.A1) becomes zero, yielding Eq. (2.6) is obtained. For consistency, Eq. (2.6) is expressed as a function of $\bar{S}_{pre-flow}$ and $\bar{S}_{flow}$ using the relationship $\bar{S}_{tot-air} = 1 - \bar{S}_{flow}$.
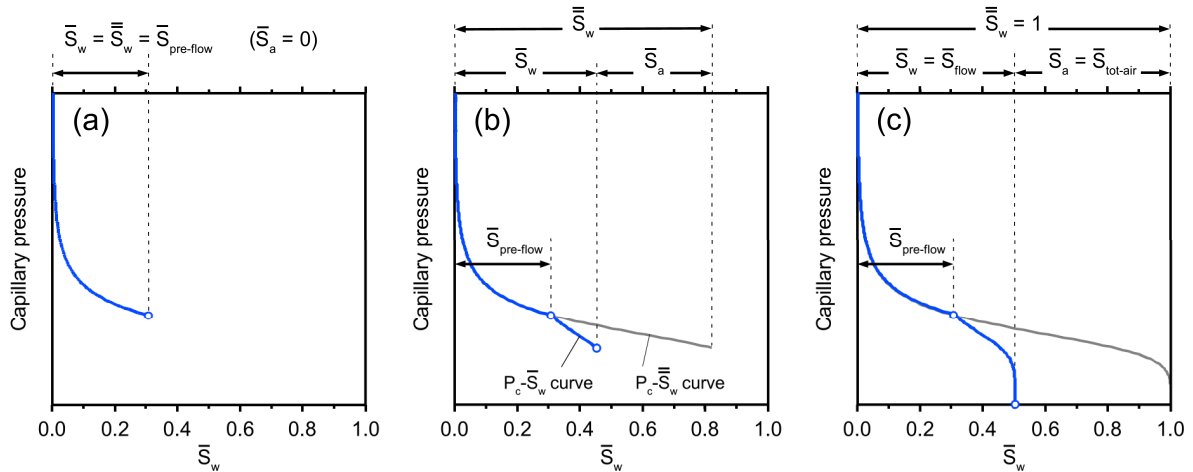
Fig. 2.A1. Schematic of the relationship between capillary pressure P_c and effective water saturation $\bar{S}_w$ before water infiltration (after drying) (a), during water infiltration with air entrapment (b) and after reaching $P_c = 0$ (c). $\bar{S}_w$ is calculated by $\bar{S}_w = (S_w - S_{wr})/(1 - S_{wr})$, where S_{wr} is the saturation of residual water.

References

Assouline S. (2001) A model for soil relative hydraulic conductivity based on the water retention characteristic curve. *Water Resour. Res.* **37**(2), 265–271.

Bear J. (1972) *Dynamics of Fluids in Porous Media*. Dover, Mineola, N. Y.

Bourbie T. and Zinszner B. (1985) Hydraulic and acoustic properties as a function of porosity in Fontainebleau sandstone. *J. Geophys. Res.* **90**, 1524−1532.

Brooks R. H. and Corey A. T. (1964) Hydraulic properties of porous media. *Hydrol. Pap. 3*, Colo. State Univ., Fort Collins, Colo.

Brutsaert W. and Chen D. Y. (1995) Desorption and the two stages of drying of natural tallgrass prairie. *Water Resour. Res.* **31**(5), 1305–1313.

Brutsaert W. (2000) A concise parameterization of the hydraulic conductivity of unsaturated soils. *Adv. Water Resour.* **23**, 811–815.

Burdine N. T. (1953) Relative permeability calculation for pore size distribution data. *Tras. Am. Inst. Min. Metall. Pet. Eng.* **198**, 71–78.

Canone D., Ferraris S., Sander G. and Haverkamp R. (2008) Interpretation of water retention field measurements in relation to hysteresis phenomena. *Water Resour. Res.* **44**, W00D12.

Chatzis I., Morrow N. R. and Lim H. T. (1983) Magnitude and detailed structure of residual oil saturation. *Soc. Pet. Eng. J.* **24**(5), 311−326.

Coussot P. (2000) Scaling approach of the convective drying of a porous medium. *Eur. Phys. J. B* **15**(3), 557−566.

D'Hollander E. H. (1979) Estimation of the pore size distribution from the moisture characteristic. *Water Resour. Res.* **15**, 107−112.

Doyen P. M. (1988) Permeability, conductivity, and pore geometry of sandstone. *J. Geophys. Res.* **93**, 7729−7740.

Dullien F. A. L. (1979) *Porous Media, Fluid Transport and Pore Structure*. Academic, San Diego, Calif.

Dullien F. A. L., Zarcone C., Macdonald I. F., Collins A. and Bochard R. D. E. (1989) The effects of surface-roughness on the capillary-pressure curves and the heights of capillary rise in glass bead packs. *J. Colloid Interface Sci.* **127**(2), 362–372.

Evans D. D., Nicholson T. J. and Rasmussen T. C. (2001) Flow and transport through unsaturated fractured rock: as overview. In: *Flow and transport through unsaturated fractured rock, Geophys. Monogr. Ser.*, vol. 42 (eds. D. D. Evans et al.). AGU, Washington, D.C., pp. 1−18.

Fagerlund F., Niemi A. and Illangasekare T. H. (2008) Modeling of nonaqueous phase liquid (NAPL) migration in heterogeneous saturated media: effects of hysteresis and fluid immobility in constitutive relations. *Water Resour. Res.* **44**, W03409.

Faybishenko B. (1995) Hydraulic behavior of quasi-saturated soils in the presence of entrapped air: Laboratory experiments. *Water Resour. Res.* **31**(10), 2421–2435.

Gelinas C. and Angers R. (1986) Improvement of the dynamic waterexpulsion method for pore size distribution measurements. *Am. Ceram. Soc. Bull.* **65**, 1297−1300.

Gouet-Kaplan M., Tartakovsky A. and Berkowitz B. (2009) Simulation of the interplay between resident and infiltrating water in partially saturated porous media. *Water Resour. Res.* **45**, W05416.

Gupta R. P. and Swartzendruber D. (1964) Entrapped air content and hydraulic conductivity of quartz sand during prolonged liquid flow. *Soil Sci. Soc. Am. J.* **28**(1), 9–12.

Haverkamp R., Reggiani P., Ross P. J. and Parlange J.-Y. (2002) Soil water hysteresis prediction model based on theory and geometric scaling. In *Environmental Mechanics: Water, Mass and Energy Transfer in the Biosphere, Geophys. Monogr. Ser.*, vol. 129. AGU, Washington, D. C., pp. 213−246.

Heaviside J. (1991) Measurement of Relative Permeability. In *Interfacial Phenomena in*

Petroleum Recovery (eds. N. R. Morrow). Marcel Dekker, N. Y., pp. 377−411.

Hildenbrand A., Schlömer S. and Krooss B. M. (2002) Gas breakthrough experiments on fine-grained sedimentary rocks. *Geofluids* **2**, 3−23.

Hildenbrand A., Schlomer S., Krooss B. M. and Littke R. (2004) Gas breakthrough experiments on pelitic rocks: comparative study with N_2, CO_2, and CH_4. *Geofluids* **4**, 61−80.

Hillel D. (1998) *Environmental soil physics*. Academic Press, San Diego, CA.

Indraratna B. and Ranjith P. (2001) *Hydromechanical aspects and unsaturated flow in jointed rock*. A. A. Balkema Publishers.

Innocentini M. D. M., and Pandolfelli V. C. (2001) Permeable porosity of refractory castables evaluated by the waterexpulsion porosimetry technique. *J. Am. Ceram. Soc.* **84**, 236−238.

Jury W. A. and Horton R. (2004) *Soil physics*. John Wiley, Hoboken, N. J.

Kieffer B., Jove C. F., Oelkers E. H. and Schott J. (1999) An experimental study of the reactive surface area of the Fontainebleau sandstone as a function of porosity, permeability, and fluid flow rate. *Geochim. Cosmochim. Acta* **63**, 3525−3534.

Klute A. (1986) Water retention: Laboratory methods. In *Methods of Soil Analysis, Part 1: Physical and Mineralogical Methods, Agron. Monogr. 9* (eds. A. Klute). Am. Soc. of Agron., Madison, WI., pp. 635–662.

Kool J. B. and Parker J. C. (1987) Development and evaluation of closed-form expressions for hysteretic soil hydraulic properties. *Water Resour. Res.* **23**(1), 105–114.

Kosugi K. (1994) Three-parameter lognormal distribution model for soil water retention. *Water Resour. Res.* **30**(4), 891–901.

Kosugi K. (1996) Lognormal distribution model for unsaturated soil hydraulic properties. *Water Resour. Res.* **32**(9), 2697–2703.

Krevor S. C. M., Pini R., Zuo L. and Benson S. M. (2012) Relative permeability and trapping of CO_2 and water in sandstone rocks at reservoir conditions. *Water Resour. Res.* **48**, W02532.

Kumar M., Senden T., Sheppard A., Middleton J. and Knackstedt M. (2010) Visualizing and quantifying the residual phase distribution in core material. *Petrophysics* **51**(5), 323–332.

Land C. S. (1968) Calculation of imbition relative permeability for two- and three-phase flow from rock properties. *Soc. Pet. Eng. J. Trans. Am. Inst. Min. Metall. Pet. Eng.* **243**, 149–156.

Lehmann P., Assouline S. and Or D. (2008) Characteristic lengths affecting evaporative drying of porous media. *Phys. Rev. E* **77**, 056309.

Lenhard R. J. and Parker J. C. (1987) A model for hysteretic constitutive relations governing multiphase flow: 2. Permeability-saturation relations. *Water Resour. Res.* **23**(12), 2197–2206.

Lenhard R. J., Parker J. C. and Kaluarachchi J. J. (1991) Comparing simulated and experimental hysteretic two-phase transient fluid flow phenomena. *Water Resour. Res.* **27**(8), 2113–2124.

Lindquist W. B., Venkatarangan A., Dunsmuir J. and Wong T. (2000) Pore and throat size distributions measured from synchrotron X-ray tomographic images of Fontainebleau sandstones. *J. Geophys. Res.* **105**(B9), 21,509–21,527.

Lowry M. I. and Miller C. T. (1995) Pore-scale modeling of nonwetting-phase residual in porous media. *Water Resour. Res.* **31**(3), 455–473.

Luckner L., van Genuchten M. T. and Nielsen D. R. (1989) A consistent set of parametric models for the two-phase flow of immiscible fluids in the subsurface. *Water Resour. Res.* **25**(10), 2187–2193.

Mualem Y. (1976) New model for predicting hydraulic conductivity of unsaturated porousmedia. *Water Resour. Res.* **12**, 513−522.

Mualem Y. (1986) Hydraulic conductivity of unsaturated soils: Prediction and formulas. In *Methods of Soil Analysis, part 1, Physical and Mineralogical Methods*, *Agron. Monogr. 9* (eds. A. Klute). Am. Soc. of Agron., Madison, WI, pp. 799−823.

Parker J. C. and Lenhard R. J. (1987) A model for hysteretic constitutive relations governing multiphase flow: 1. Saturation-pressure relations. *Water Resour. Res.* **23**(12), 2187–2196.

Parlange M. B., Katul G. G., Cuenca R. H., Kavvas M. L., Nielsen D. R. and Mata M. (1992) Physical basis for a time series model of soil water content. *Water Resour. Res.* **28**(9), 2437–2446.

Pentland C. H., El-Maghraby R., Iglauer S. and Blunt M. J. (2011) Measurements of the capillary trapping of super-critical carbon dioxide in Berea sandstone. *Geophys. Res. Lett.*, **38**, L06401.

Sakaguchi A., Nishimura T. and Kato M. (2005) The effect of entrapped air on the quasi-saturated soil hydraulic conductivity and comparison with the unsaturated hydraulic conductivity. *Vadose Zone J.* **4**, 139−144.

Scherer G. W. (1990) Theory of drying, *J. Am. Ceram. Soc.* **73**, 3−14.

Shokri N., Lehmann P. and Or D. (2008) Effects of hydrophobic layers on evaporation from porous media. *Geophys. Res. Lett.* **35**, L19407.

Sok R. M., Knackstedt M. A., Sheppard A. P., Pinczewski W. V., Lindquist W. B., Venkatarangan A. and Paterson L. (2002) Direct and stochastic generation of network models from tomographic images; effect of topology on residual saturations. *Transp. Porous Media* **46**(2), 345–371.

Suzanne K., Hamon G., Billiotte J. and Trocme V. (2003) Experimental relationships between residual gas saturation and initial gas saturation in heterogeneous sandstone reservoirs. In: Paper presented at SPE Annual Technical Conference and Exhibition, SPE, Denver,

Colorado.

Tsimpanogiannis I. N., Yortsos Y. C., Poulou S., Kanellopoulos N. and Stubos A. K. (1999) Scailing theory of drying in porous media. *Phys. Rev. E* **59**(4), 4353−4365.

Turton D. J., Barnes D. R. and de Jesus Navar J. (1995) Old and new water in subsurface flow from a forest soil block. *J. Environ. Qual.* **24**, 139−146.

van Genuchten M. T. (1980) A closedform equation for predicting the hydraulic conductivity of unsaturated soils. *Soil Sci. Soc. Am. J.* **44**, 892−898.

Wardlaw N. C. and Cassan J. P. (1978) Estimation of recovery efficiency by visual observation of pore systems in reservoir rocks. *Bulletin of Canadian Pet. Geo.* **26**(4), 572–585.

Yokoyama T. and Takeuchi S. (2009) Porosimetry of vesicular volcanic products by a water-expulsion method and the relationship of pore characteristics to permeability. *J. Geophys. Res.* **114**, B02201.

Zhou N., Matsumoto T., Hosokawa T. and Suekane T. (2010) Pore-scale visualization of gas trapping in porous media by X-ray CT scanning. *Flow Meas. Instrum.* **21**, 262–267.

Zimmerman R. W. and Bodvarsson G. S. (1989) An approximate solution for onedimensional absorption in unsaturated porousmedia. *Water Resour. Res.* **25**, 1422−1428.

Chapter 3

Prediction of Saturated and Unsaturated Hydraulic Conductivities of Sandstone by Using Size Distribution of Transport Pores

Abstract

The pore size distribution of a rock is one of the important factors controlling permeability (hydraulic conductivity). The Katz and Thompson model (KT model) can predict permeability using only pore size distribution and porosity. Previous studies have conventionally used those of open pores measured by mercury intrusion porosimetry. However, open pores usually include pores unavailable for flow such as dead ends and dents. In contrast, water-expulsion porosimetry (WEP) yields information of transport pores directly serving as flow paths. The size distributions and porosities of transport pores of nine sandstones were measured by WEP, and the permeabilities predicted by the KT model were compared with those measured using a gas permeameter. Permeabilities are shown to be better predicted by using transport porosity rather than by open porosity. Application to predicting the permeability–saturation degree relation by combining WEP, the KT model, and a multi-phase flow model is also discussed.

3.1. Introduction

Estimations of permeabilities (hydraulic conductivities) of rocks are essential in considering various geological and engineering processes, including groundwater flow, ore deposit formation, and oil and gas storage. Empirical and theoretical models have been proposed to predict the permeability of rock (single-phase flow) based on porosity, pore size, pore size distribution, pore connectivity, and tortuosity (e.g., *Walsh and Brace*, 1984; *Katz and Thompson*, 1986, 1987; *Guéguen and Dienes*, 1989; *Bernabé et al.*, 2010). A model proposed by *Katz and Thompson* (1987) (KT model) is a very useful model because it is known to predict the permeability of sandstone using no adjustable parameters within error of a factor of three (*Thompson et al.*, 1987) and the only data required is the pore size distribution (capillary pressure curve) and porosity.

Mercury intrusion porosimetry (MIP) has been widely used to determine the pore size distribution of rock. Previous studies addressing the KT model have commonly measured the data required for the modeling by MIP (e.g., *Katz and Thompson*, 1987; *Bernard et al.*, 2007; *Milsch et al.*, 2008; *Amirtharaj et al.*, 2011). MIP provides the relation between mercury pressure and the volume of mercury intruded into a sample, which corresponds to the capillary pressure curve (Fig. 3.1a). Because a mercury pressure is related to a pore diameter, the capillary pressure curve can be converted to the pore size distribution (Fig. 3.1b). As another method for measuring pore size distribution, there is water-expulsion porosimetry (WEP) (*Nishiyama et al.*, 2012). This

method is also called the gas breakthrough method (*Hildenbrand et al.*, 2004), and the measurement principle is similar to the pressure plate method (e.g., *Klute*, 1986) often used in soil physics. Although WEP is not as widely used as MIP, WEP is harmless and inexpensive as long as air and water are used (other combination of fluids is also available), and the sample used in the measurement can be reused for other purposes. These are large advantages of WEP over MIP, considering that mercury is harmful and the sample used in the MIP measurement cannot be reused. In WEP, a gas pressure is applied from one end of a water-saturated sample, and water in pores penetrating the sample is expelled to the other end. Thus, WEP provides the information of "transport pores" that are directly serving as flow paths (*Yokoyama and Takeuchi*, 2009), in which dead-end pores and dents that are unavailable for flow paths are not included. In contrast, the result of MIP usually measures the information of "open pores" that includes pores unavailable for fluid flow because mercury is injected into all pores open to the outside of the sample (*Chen and Penumadu*, 2006). Given these differences between MIP and WEP, to use the capillary pressure curve and porosity of transport pores determined by WEP rather than those of open pores determined by MIP is inferred to be reasonable for predicting permeability with the KT model. However, to our knowledge, no previous study has combined the information of transport pores with the KT model, and the applicability of the data by WEP to the KT model remains to be evaluated.

If accurate estimation of permeability is possible using the data of WEP and the KT model, it is also useful in modeling of multi-phase flow in rock pores (e.g., water flow under unsaturated condition). Because experimental determination of the relation between permeability to a fluid phase (effective permeability in m^2) and saturation degree S is difficult and time consuming, this relation is often predicted from a capillary pressure curve (or water retention curve) that is more easily measured by methods such as pressure plate method and WEP. For this prediction, multi-phase flow models using a capillary pressure curve have been developed (e.g., *Brooks and Corey*, 1964; *Mualem*, 1976; *van Genuchten*, 1980). Because these models commonly provide "relative permeability" (i.e., the "ratio" of the effective permeability at a given S to the intrinsic permeability (permeability at S=100%)), the intrinsic permeability must be separately measured to obtain the effective permeability (absolute value) at each S. However, there is a possibility that the effective permeability–S relation can be predicted from only a capillary pressure curve by the combination of the KT model for determining the intrinsic permeability and a multi-phase flow model.

With these points in mind, we measured the capillary pressure curves and

porosities of transport pores in sandstones by WEP and compared the permeabilities predicted by the KT model using the results of WEP with those measured experimentally. We also discuss a way to predict the effective permeability– S relation by combining WEP, the KT model, and a multi-phase fluid flow model.

3.2. Katz and Thompson Model

Based on percolation theory (critical path analysis), *Katz and Thompson* (1987) postulated that the following equation can express the intrinsic permeability of a rock k_{KT} (m^2) if pore diameter d (m) is selected optimally:

$$k_{KT} = \frac{1}{89} \phi \frac{d^3}{d_c} f(d),$$ (3.1)

where ϕ is the porosity of the rock and $f(d)$ is the volume fraction of pores having diameters of d and larger. d_c (m) is the critical pore diameter, defined as the diameter of the smallest portion in the largest flow path penetrating the sample. Eq. (3.1) assumes that permeability is mainly controlled by the pores with diameters of d and larger, and the diameters of pores larger than d are all considered as equal to d and the rest are zero. Under this assumption, Eq. (3.1) will yield the value of k_{KT} which is smaller than the actual value. Therefore, if d is chosen as $d^3 f(d)$ is maximized ($d = d^h_{max}$), k_{KT} becomes closest to the actual value. By inserting $d = d^h_{max}$ into Eq. (3.1), the following KT model for predicting permeability can be obtained:

$$k_{KT} = \frac{1}{89} \phi \frac{\left(d^h_{max}\right)^3}{d_c} f\left(d^h_{max}\right).$$ (3.2)

Katz and Thompson (1987) proposed a procedure to determine d_c and d^h_{max} from the data of MIP. d_c is obtained from the pressure corresponding to the inflection point in the capillary pressure curve using the Washburn equation $P_{Hg} = -4\gamma_{Hg} \cos\theta_{Hg}/d$, where P_{Hg} is the mercury pressure (Pa), γ_{Hg} is the surface tension of mercury (0.485 N m^{-1}), and θ_{Hg} is the contact angle of mercury (141.3°); an example is shown in Fig. 3.1a. This is based on the observation that mercury cluster penetrating through the sample is first formed at the pressure close to the inflection point (*Katz and Thompson*, 1986). In determining d^h_{max}, *Katz and Thompson* (1987) used the cumulative pore size distribution measured by MIP as $f(d)$. They assumed that the volume of mercury injected prior to the pressure at the inflection point (surface volume, as indicated in Fig.

3.1a) is due to the defects at the sample surfaces and pores not involved in the first percolating mercury cluster. By calculating $f(d)$ in which the surface volume is neglected, $d^3 f(d)$ is calculated, and d_{max}^h is determined from the maximum value in the $d^3 f(d)$ (Fig. 3.1c). We determined d_c, d_{max}^h, and $f(d_{max}^h)$ following the above procedure but used the capillary pressure curve measured by WEP.
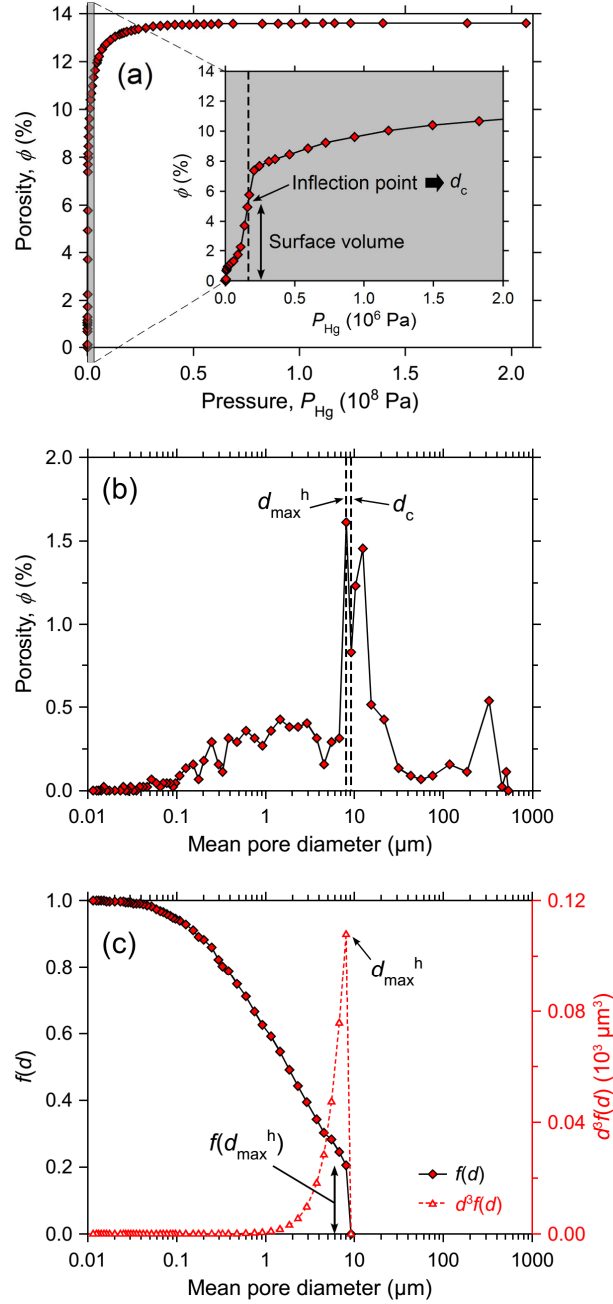

Fig. 3.1. Measurement result by mercury intrusion porosimetry for a Berea sandstone (sample 5). (a) Capillary pressure curve. Vertical dotted line represents the inflection

point on the curve. (b) Pore size distribution. A peak at 200–300 μm diameters may be attributable to the detachment of grains at the time of sample preparation as described in *Nishiyama et al.* (2012). (c) Pore diameter (d) vs. $f(d)$ and $d^3 f(d)$ calculated by the capillary pressure curve.

3.3. Materials and Methods

3.3.1. Sandstones

Four Fontainebleau sandstones (Fb), four Berea sandstones (Br), and one Indian sandstone (In) were used. Cylindrical core of each sandstone (24–35 mm in diameter and 9.5–16 mm in length) was mounted in a resin (Technovit 4004) to seal its lateral side and was used for the porosity, permeability, and WEP measurements. Open porosity ϕ_{open}, transport porosity ϕ_{tra}, and permeability k_{meas} (m^2) of each sample are summarized in Table 3.1. ϕ_{open} was measured from the difference between the water-saturated and dry weights of the sample. ϕ_{tra} was determined by the WEP measurement, as the procedure is described later (for details, see *Yokoyama and Takeuchi* (2009)). k_{meas} was measured using a gas permeameter, following the same procedure reported in *Yokoyama and Takeuchi* (2009). Cylinders of samples 2 and 5 with 14 mm in diameter and 5–10 mm in length (no lateral seal) were also made for the MIP measurement (AutoPore IV 9500, Micromeritics).

Table 3.1. Physical properties, parameters of the KT model determined from the capillary pressure curves measured by water-expulsion method (for samples 2 and 5, data of mercury intrusion porosimetry are also shown), and measured and calculated permeabilities of sandstone samples.

Sample	1	2	3	4	5	6	7	8	9
Sandstone[a]	Fb	Fb	Fb	Fb	Br	Br	Br	Br	In
ϕ_{open} (%)	5.7	6.1 (6.0)[d]	10	26	16 (14)[d]	18	21	20	14
ϕ_{tra} (%)	3.2	3.7	7.3	20	8.1	11	13	13	5.6
k_{meas} (10^{-13} m^2)	0.11	0.16	2.0	29	0.20	0.83	4.7	20	0.12
d_c (μm)	13	13 (12)[d]	25	59	13 (9.2)[d]	21	37	58	8.9
d_{max}^{h} (μm)	11	11 (10)[d]	22	43	8.9 (8.1)[d]	18	30	42	6.9
$f(d_{max}^{h})$	0.38	0.38 (0.46)[d]	0.49	0.48	0.46 (0.21)[d]	0.28	0.48	0.43	0.26
k_{KT}^{b} (10^{-13} m^2)	0.23	0.25 (0.27)[d]	2.4	18	0.44 (0.18)[d]	1.4	7.8	13	0.16
k_{KT}^{c} (10^{-13} m^2)	0.13	0.15	1.7	14	0.23	0.85	4.9	8.0	0.061

[a] Fb: Fontainebleau sandstone, Br: Berea sandstone, In: Indian sandstone.

[b] Calculated from Eq. (3.2) with ϕ_{open} .

[c] Calculated from Eq. (3.2) with ϕ_{tra} .

[d] Data in parentheses were determined using the mercury intrusion method.

3.3.2. Measurement of Transport Pore Size Distribution

WEP was applied to the nine water-saturated samples to measure the size distribution of transport pores. A brief outline of the experimental procedures is provide here (for more details, see *Nishiyama et al.* (2012) and Chapter 2 in this thesis). When a gas pressure is applied to the lower end of the water-saturated sample, pore water is expelled from the upper end. Assuming cylindrical pore geometry, the pressure difference between the lower and upper ends of the sample ΔP (Pa) and the diameter of the pores from which water is expelled (d) can be correlated by (*Gelinas and Angers*, 1986)

$$\Delta P = \frac{4\gamma\cos\theta}{d},$$
(3.3)

where γ is the surface tension of the water-gas interface (for water-air system, 7.28×10^{-2}–7.20×10^{-2} N m^{-1} at 20–25°C), and θ is the contact angle between solid and water (assumed to be 0°, as with *Gelinas and Angers* (1986)). According to Eq. (3.3), water is expelled first from the largest pores, and water in smaller pores is progressively expelled with increasing ΔP. By measuring the volume of expelled water with increasing ΔP in incremental steps, the pore size distribution of transport pores that can be converted to capillary pressure curve is obtained, and transport porosity is also determined from the total amount of expelled water. The volume of water expelled at each ΔP was measured by wiping the water with a dry tissue until water expulsion ceased and measuring the change in the weight of the tissue.

The experiments were conducted at 20–25°C. Compressed air, humidified before injecting into the sample (relative humidity ~93%), was used as a working gas. The maximum pressure applied was ΔP = 1.0×10^{5}–2.0×10^{5} Pa, equivalent to pore diameters of 1.4–2.9 μm. For sample 2, the maximum pressure was confirmed to be enough to extrude almost all water from transport pores (*Nishiyama et al.*, 2012 and Chapter 2 in this thesis). However, some water in transport pores might remain, especially for the samples having smaller pore diameters. As an example, the pore size distribution of sample 5 measured by MIP shows that pores of <1.4 μm occupy 22% of open pores (Fig. 3.1b). If some of the 22% corresponds to transport porosity, the true

value of transport porosity is somewhat larger than the value determined for the pores of ≥ 1.4 μm by WEP.

3.4. Results and Discussion

3.4.1. Prediction of Permeability by Applying WEP Results to the KT Model

The capillary pressure curves and the pore size distributions of the nine samples determined by WEP are shown in Fig. 3.2. d_c of each sample was determined from the pressure at the inflection point on the capillary pressure curve using Eq. (3.3). $d^3 f(d)$ was calculated from the result of WEP, and $d_{\max}^h$ was determined from the peak of the $d^3 f(d)$ (Fig. 3.2). The values of d_c, $d_{\max}^h$, and $f(d_{\max}^h)$ obtained are summarized in Table 3.1. Fig. 3.3 compares the permeabilities measured using a gas permeameter with the values predicted using the results of WEP (unfilled square). In the calculation, ϕ_{open} was used as ϕ in Eq. (3.2), as with *Katz and Thompson* (1987). The predicted permeabilities k_{KT} are in good agreement with the measured values k_{meas} within a factor of three. To compare the accuracy of k_{KT} predicted by WEP with those by MIP, d_c, $d_{\max}^h$, and $f(d_{\max}^h)$ of samples 2 and 5 were determined from the data of MIP (the result of sample 2 is shown in Fig. 2.1b and that of sample 5 is shown in Fig. 3.1). The parameters obtained are given in Table 3.1, and the resultant values of k_{KT} are plotted in Fig. 3.3 (unfilled circle). The values of d_c, $d_{\max}^h$, and $f(d_{\max}^h)$ determined by WEP and MIP are revealed to be similar, although the two methods yield the size distribution of different types of pores. The k_{KT} determined by WEP are as close to the measured values as those by MIP, which demonstrates that the results of WEP are not inferior to those of MIP in applying to the KT model.

Although ϕ_{open} has been conventionally employed in applying to the KT model, open pores include pores unavailable for fluid flow as noted previously. As is seen in Table 3.1, ϕ_{tra} is always smaller than ϕ_{open}, that is, there are some pores not contributing to flow. Here, we attempted to use ϕ_{tra} instead of ϕ_{open} in calculating k_{KT} using Eq. (3.2). In Fig. 3.3, it is apparent that k_{KT} calculated by ϕ_{tra} (filled diamond) are closer to the 1:1 line than those calculated by ϕ_{open}, suggesting that ϕ_{tra} rather than ϕ_{open} is suited for calculating permeability by the KT model. This is consistent with the physical meaning of ϕ_{tra} that transport pores do not include pores that are not serving as flow path.
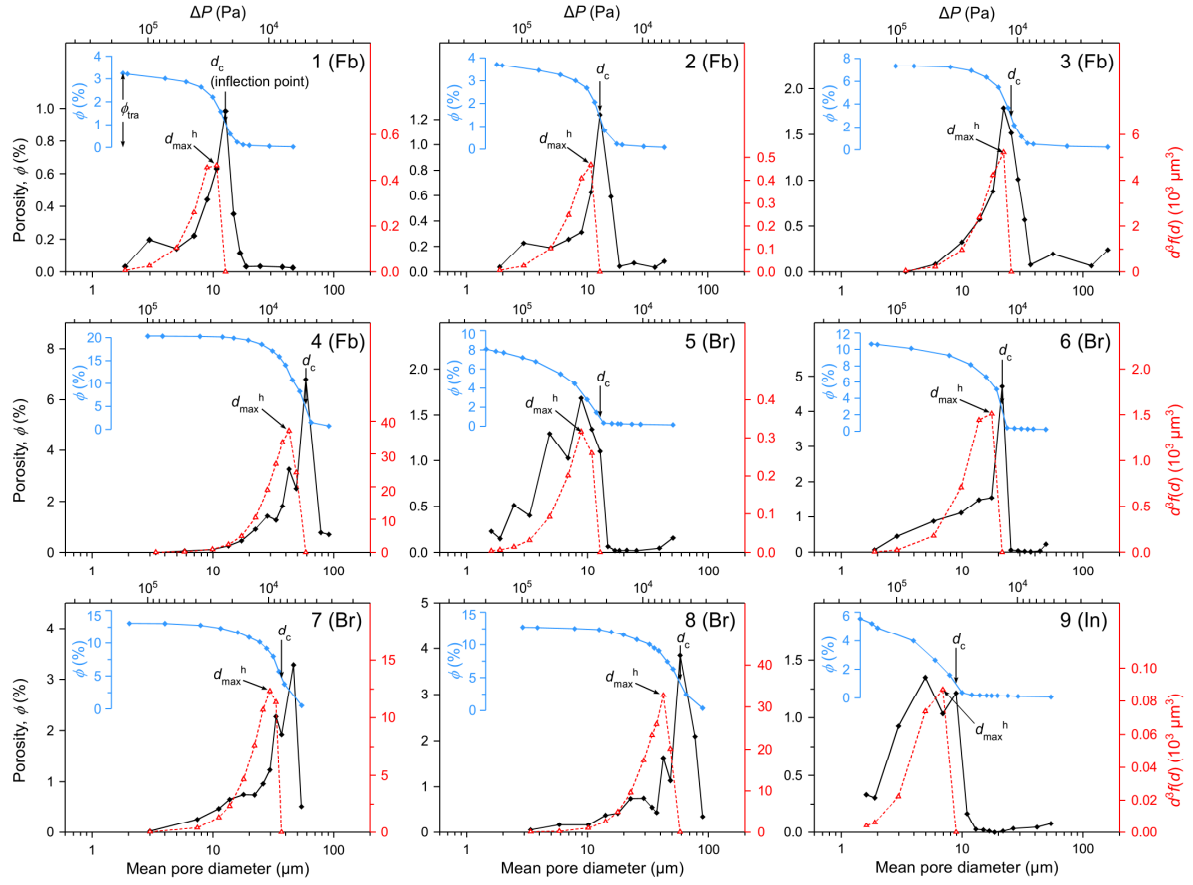
Fig. 3.2. Capillary pressure curve (blue solid line), pore size distribution (black solid line), and calculated $d^3 f(d)$ (red dotted line), as determined for nine sandstone samples by the water-expulsion porosimetry. Arrows represent the pressure at the inflection point on each curve relating to the critical pore diameter (d_c) and the optimum pore diameter (d_{max}^h), as determined by the procedure of *Katz and Thompson* (1987).
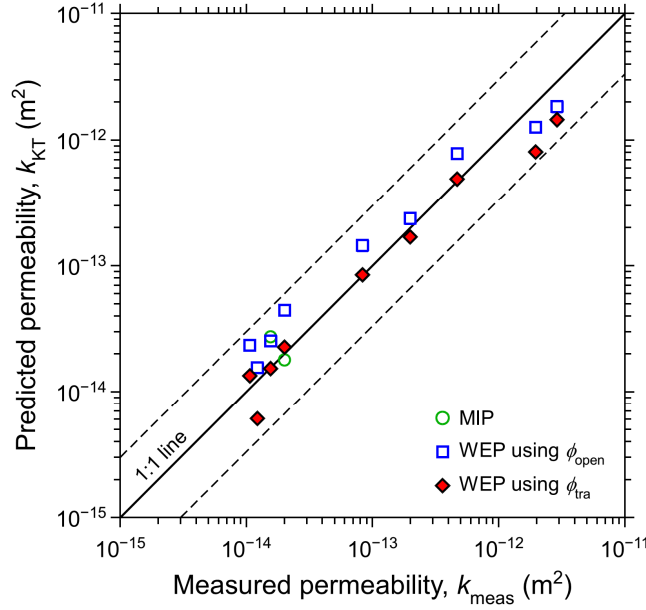
Fig. 3.3. Comparison of measured permeability (k_{meas}) with the values predicted from Eq. (3.2) (k_{KT}) using open porosity (ϕ_{open}) and transport porosity (ϕ_{tra}). Dashed line shows a factor of three deviation between k_{meas} and k_{KT}, which corresponds to the range of prediction errors of the KT model using the MIP data as reported by *Thompson et al.* (1987).

3.4.2. Application to Predicting the Effective Permeability–Saturation Degree Relation

Finally, we propose a way to predict the effective permeability to water (absolute value) as a function of saturation degree using only a capillary pressure curve measured by WEP (or pressure plate method). The effective permeability to water at a given S, $k(S)$ (m^2), is calculated by $k(S) = k_{\text{r}}(S)k$, where k (m^2) is the intrinsic permeability which can be obtained from a capillary pressure curve and the KT model as we show above (k can be replaced by k_{KT}). $k_{\text{r}}(S)$ is the relative permeability to water at S and can be also calculated from the capillary pressure curve. Here, we calculated $k_{\text{r}}(S)$ by the Mualem-van Genuchten (MVG) model modified by *Lenhard and Parker* (1987). The modified MVG model has two equations—one describes the capillary pressure curve and the other expresses $k_{\text{r}}(S)$. For the application of the model, first, the following equation (*van Genuchten*, 1980) is fitted to a measured capillary pressure curve: $S_{\text{CPC}} = (1 - S_{\text{wr}})\left[1 + (\alpha P_c)^{1/1-m}\right]^{-m} + S_{\text{wr}}$, where S_{CPC} is the water saturation during capillary pressure curve measurement, P_c (Pa) is the capillary pressure ($= \Delta P$), α (Pa^{-1}) and m are shape parameters of capillary pressure curve, and S_{wr} is the residual water saturation that corresponds to the difference of the volume between open

pores and transport pores (Fig. 3.4a). It should be noted that the determination of S_{wr} is possible by WEP but impossible by MIP. $k_r(S)$ (Fig. 3.4a) can be calculated by inserting the obtained value of m into the expression of $k_r(S)$ given in *Lenhard and Parker* (1987) and *Nishiyama et al.* (2012) (Eq. (2.6) in this thesis). Fitting the van Genuchten equation to the capillary pressure curve measured for sample 2 (Fig. 3.4a) gave m = 0.82, α = 4.2 × 10^{-5} Pa^{-1}, and S_{wr} = 0.40. The predicted $k(S)$ ($= k_r(S)k_{KT}$) for sample 2 is plotted in Fig. 3.4b, together with measured values reported in *Nishiyama et al.* (2012). The predicted curve of $k(S)$ agrees well with the measured values especially for the curve calculated using ϕ_{tra}. The method presented above is the first attempt of predicting both the intrinsic and effective permeabilities of rock using a single capillary pressure curve, although the methods to predict each of these permeabilities separately have been proposed in previous studies. These discussions would contribute not only to facilitating the modeling of multi-phase flow in rock pores but also to comprehensively understanding the relation between the intrinsic/effective permeabilities and pore structure.

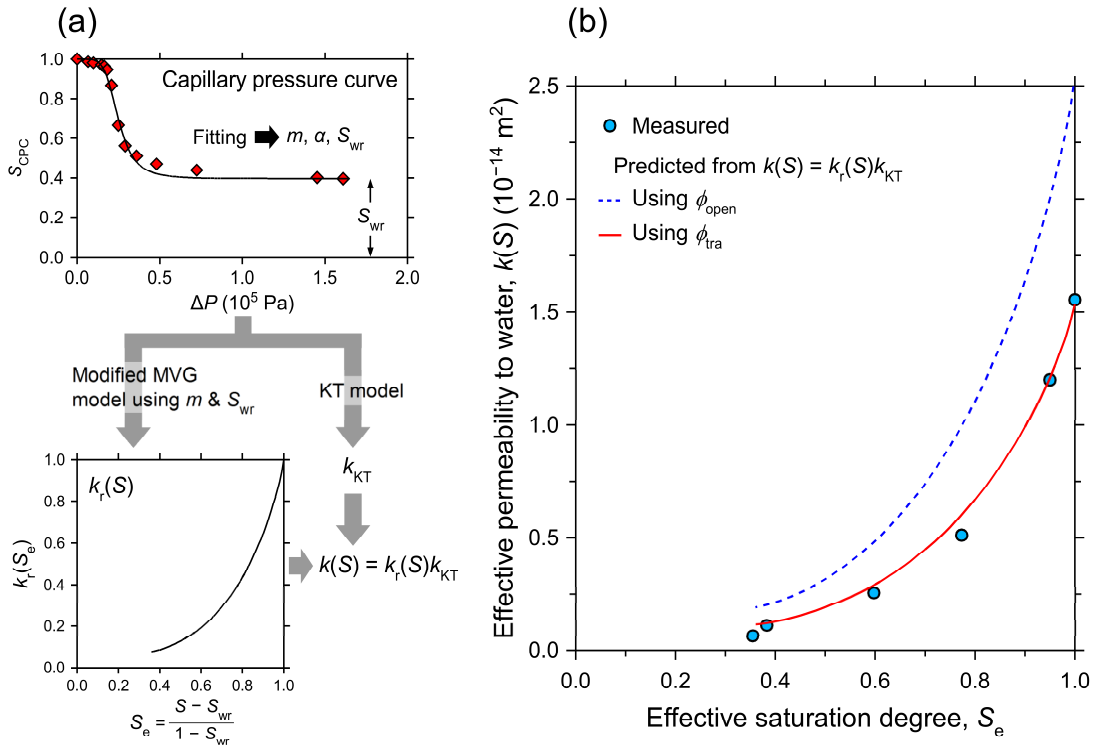**Fig. 3.4.** (a) Procedure for obtaining k_{KT}, $k_r(S)$, and $k(S)$ from a capillary pressure curve. (b) Comparison of the effective permeability to water ($k(S)$) measured at each water saturation degree (circle) and the values predicted by combining intrinsic permeability (k_{KT}) from the KT model with relative permeability ($k_r(S)$) from the modified Mualem-van Genuchten (MVG) model. Horizontal axis is the effective

saturation degree calculated by $S_e = (S - S_{wr})/(1 - S_{wr})$ because the modified MVG model provides $k_r(S)$ as a function of S_e.

3.5. Conclusions

Our results demonstrate that to apply the capillary pressure curve of transport pores determined by WEP to the KT model is effective for predicting the permeability of sandstone. To use ϕ_{tra} as an input parameter for the KT model was shown to improve the predictability of permeability. These findings ensure a way to predict the effective permeability–saturation degree relation from a capillary pressure curve only. Therefore, our results would be useful not only for estimating intrinsic permeability but also for modeling multi-phase fluid flow phenomena including water permeation in vadose zone and geological sequestration of carbon dioxide.

References

Amirtharaj E. S., Ioannidis M. A., Parker B. and Tsakiroglou C. D. (2011) Statistical synthesis of imaging and porosimetry data for the characterization of microstructure and transport properties of sandstones. *Transp. Porous Media* **86**, 135–154.

Bernabé Y., Li M. and Maineult A. (2010) Permeability and pore connectivity: a new model based on network simulations. *J. Geophys. Res.* **115**, B10203.

Bernard M. L., Zamora M., Géraud Y. and Boudon G. (2007) Transport properties of pyroclastic rocks from Montagne Pelée volcano (Martinique, Lesser Antilles). *J. Geophys. Res.* **112**, B05205.

Brooks R. H. and Corey A. T. (1964) *Hydraulic properties of porous media*. Hydrol. Pap. 3. Colo. State Univ., Fort Collins, CO.

Chen X. and Penumadu D. (2006) Characterizing microstructure of refractory porous materials. *J. Mater. Sci.* **41**, 3403–3415.

Gelinas C. and Angers R. (1986) Improvement of the dynamic waterexpulsion method for pore size distribution measurements. *Am. Ceram. Soc. Bull.* **65**, 1297−1300.

Guéguen Y. and Dienes J. (1989) Transport properties of rocks from statistics and percolation. *Math. Geol.* **21**, 1–13.

Hildenbrand A., Schlomer S., Krooss B. M. and Littke R. (2004) Gas breakthrough experiments on pelitic rocks: comparative study with N_2, CO_2, and CH_4. *Geofluids* **4**, 61−80.

Katz A. J. and Thompson A. H. (1986) Quantitative prediction of permeability in porous rock. *Phys. Rev. B* **34**, 8179–818.

Katz A. J. and Thompson A. H. (1987) Prediction of rock electrical conductivity from mercury injection measurements. *J. Geophys. Res.* 92, 599–607.

Klute A. (1986) Water retention: Laboratory methods. In: *Methods of Soil Analysis, Part 1: Physical and Mineralogical Methods, Agron. Monogr. 9* (eds. A. Klute). Am. Soc. of Agron., Madison, WI., pp. 635–662.

Lenhard R. J. and Parker J. C. (1987) A model for hysteretic constitutive relations governing multiphase flow: 2. Permeability-saturation relations. *Water Resour. Res.* 23, 2197–2206.

Milsch H., Blöcher G. and Engelmann S. (2008) The relationship between hydraulic and electrical transport properties in sandstones: an experimental evaluation of several scaling models. *Earth Planet. Sci. Lett.* 275, 355–363.

Mualem Y. (1976) New model for predicting hydraulic conductivity of unsaturated porousmedia. *Water Resour. Res.* 12, 513−522.

Nishiyama N., Yokoyama T. and Takeuchi S. (2012) Size distribution of pore water and entrapped air during drying-infiltration processes of sandstone characterized by water-expulsion porosimetry. *Water Resour. Res.* 48, W09556.

Thompson A. H., Katz A. J. and Krohn C. E. (1987) The microgeometry and transport properties of sedimentary rock. *Adv. Phys.* 36, 625–694.

van Genuchten M. T. (1980) A closedform equation for predicting the hydraulic conductivity of unsaturated soils. *Soil Sci. Soc. Am. J.* 44, 892−898.

Walsh J. B. and Brace W. F. (1984) The effect of pressure on porosity and the transport properties of rock. *J. Geophys. Res.* 89, 9425–9431.

Yokoyama T. and Takeuchi S. (2009) Porosimetry of vesicular volcanic products by a water-expulsion method and the relationship of pore characteristics to permeability. *J. Geophys. Res.* 114, B02201.

Chapter 4

Does the Reactive Surface Area of Sandstone Depend on Water Saturation?
—The Role of Reactive-transport in Water Film

Abstract

To investigate how mineral-water reactive surface area changes depending on water saturation, flow-through dissolution experiments were performed using a sandstone core at various water saturations. Fontainebleau sandstone with an open porosity of 6.3%, consisting of ~100% quartz, was used. The water saturation of the core was adjusted to 0, 51, or 100%, and at each saturation, water was infiltrated into the core at a constant pressure. The experimental results showed that the total amount of dissolved Si did not change with decreasing water saturation. It can be therefore concluded that virtually all of the mineral surfaces were wetted with water film and allowed the progression of dissolution; i.e., the reactive surface area was not affected by water saturation despite the presence of air in the pores. The results also suggested that the flushing rate of dissolved Si from the interior of the water film to the exterior was fast enough to keep the Si concentration in the film sufficiently lower than the equilibrium concentration of quartz.

4.1. Introduction

Accurate estimation of mineral-water reactive surface area is essential for quantifying various geochemical processes including the dissolution and precipitation of minerals and the adsorption of dissolved matters. The total surface areas of soils and rocks have often been estimated by isotherm adsorption of inert gases such as N_2 and Kr (Brunauer-Emmet-Teller (BET) method) or by geometric approximation in which mineral grains or pores have uniform geometry with smooth surfaces (e.g., *White and Peterson*, 1990; *White and Brantley*, 2003; *Hodson*, 2006).

The rock pores below the water table are usually saturated with water, and all of the mineral surfaces exposed to pores may be in contact with water and available for reactions. In contrast, rocks above the water table are not saturated with water. This region is known as the vadose zone or the unsaturated zone. The depth ranges from a few meters to hundreds of meters from the ground surface (*Zimmerman and Bodvarsson*, 1989). Under water-unsaturated conditions, some pores are filled with air, which potentially results in a low reactive surface area. As an example that may be related to this issue, chemical weathering rates differ depending on whether the rates are determined in the laboratory or by field-based studies (e.g., *Pačes*, 1983; *Velbel*, 1985; *Schnoor*, 1990; *Swoboda-Colberg and Drever*, 1993; *Yokoyama and Banfield*, 2002; *White and Brantley*, 2003; *Zhu*, 2005). The uncertainty in estimating the degree of contact between mineral surfaces and water has been proposed as one of the possible

causes of field-lab discrepancies. In the vadose zone, water saturation (volume of pore water / volume of open pore) changes depending on the condition of wetting and drying. Therefore, knowledge of the relationship between water saturation and reactive surface area is important. However, experimental or theoretical studies that provide such information are very limited (*Saripalli et al.*, 2006; *Yokoyama*, 2013).

To experimentally evaluate reactive surface area, *Kieffer et al.* (1999), *Colon et al.* (2004), *Noiriel et al.* (2004), and *Scislewski and Zuddas* (2010) carried out flow-through dissolution experiments using rock cores under water-saturated conditions and estimated the reactive surface area by comparing the amount of elements discharged from the rock with the known dissolution rate constants of minerals. A similar approach was applied in this study. Water was infiltrated into the sandstone core initially adjusted to various water saturations, and the amounts of dissolved elements in the effluent were measured. By comparing the amount of dissolution at each saturation level, we investigated the relationship between reactive surface area of sandstone and water saturation.

4.2. Sample Description and Methods
4.2.1. Rock Sample

Fontainebleau sandstone from France was used in the experiments. This rock was adopted because its flow properties under water-saturated and unsaturated conditions were characterized by *Nishiyama et al.* (2012) and because its simple mineral composition can reduce uncertainty in considering reactive surface area. The mineralogical composition of the rock was ~100% quartz, which was confirmed by X-ray powder diffraction. A scanning electron microscope image (Fig. 4.1a) shows that the rock consisted of well-sorted quartz grains with approximate sizes of 200–300 μm. These properties coincide with the previous reports of *Bourbie and Zinszner* (1985), *Doyen* (1988), and *Kieffer et al.* (1999). Two cylindrical cores of the sandstone (diameter 35 mm) having lengths of 9.5 mm (FS-1) and 9.2 mm (FS-2), each mounted in a resin (Technovit 4004) to seal its lateral side, were prepared. The sample FS-1 was used in all of the flow-through dissolution experiments. The sample FS-2 was used in the supplemental experiment for visualizing flow paths using dye (for details, see section 4.2.3). The total porosity of the rock was 7.4%, which was determined by measuring the bulk density (2.45×10^3 kg m^{-3}) and the solid density (2.65×10^3 kg m^{-3}). The open porosity was 6.3% (the fraction of the pores open to the outside of the sample; isolated pores are excluded), which was determined from the difference between the

water-saturated and dry weights. More details of the porosity measurement procedures were reported in *Yokoyama and Takeuchi* (2009). Fig. 4.1b is the pore size distribution of the rock measured by mercury intrusion porosimetry. The main pore diameters range from 7–43 μm, with a peak of approximately 8–20 μm (measurement range: ca. 8 nm–500 μm). The approximately 300 μm diameter data may be attributable to the artificial surface openings formed by the detachment of quartz grains at the time of sample preparation, as noted by *Thompson et al.* (1987) and *Nishiyama et al.* (2012). The rock has a specific surface area of 0.10 $m^2 \ g^{-1}$, as measured by the N_2 adsorption BET method (FlowsorbIII 2305, Micromeritics). The BET surface area measurement was conducted using grain aggregates of a few millimeters in size in which the pore structure of the rock was preserved. The permeabilities of the samples FS-1 and FS-2, determined by constant head permeability tests, were both $1.6 \times 10^{-14} \ m^2$. This value is similar to the value ($2 \times 10^{-14} \ m^2$) reported in *Bourbie and Zinszner* (1985).
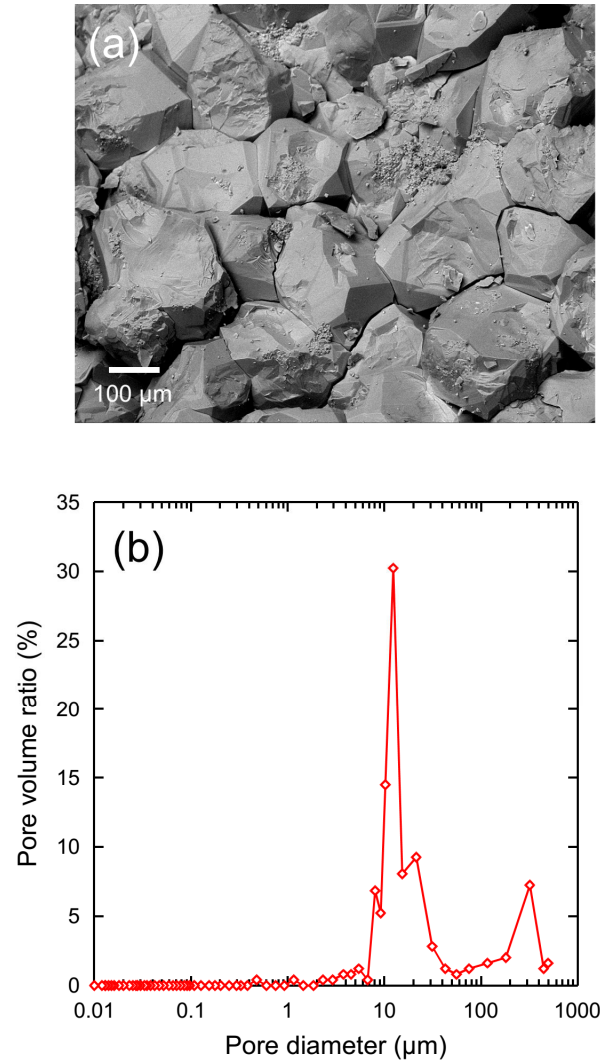
Fig. 4.1. (a) SEM image of the Fontainebleau sandstone sample. (b) Pore size distribution of the Fontainebleau sandstone measured by mercury intrusion porosimetry.

4.2.2. Flow-through Dissolution Experiments

The water saturation S (%) of a rock is generally given by

$$S = \frac{V_{\text{water}}}{V_{\text{pore}}} \times 100 = \frac{\left(W_{\text{wet}} - W_{\text{dry}}\right)/\rho_{\text{w}}}{V_{\text{pore}}} \times 100 \tag{4.1}$$

where V_{water} (m^3) is the volume of water in pores and V_{pore} (m^3) the volume of open pores. W_{wet} and W_{dry} are the wet and dry weights of the sample (kg), respectively, and ρ_{w} is the density of water (998 kg m^{-3} at 22°C). We determined S by measuring W_{wet} and W_{dry} using a digital balance with an accuracy of 0.0001 g. In the

68

flow-through dissolution experiments, water was infiltrated into the sample after adjusting S. Because S was not constant during the experiment, we refer to the S prior to the infiltration as the pre-flow water saturation "$S_{\text{pre-flow}}$". The experiment was started under three conditions: $S_{\text{pre-flow}}$ = 100% (fully saturated), 51% (partially saturated), and 0% (completely dried). To adjust $S_{\text{pre-flow}}$ to 100%, the sample was inserted in a bottle; the bottle was inserted in a vacuum chamber and degassed; water was poured into the bottle while degassing to submerge the sample; and finally, the chamber was ventilated, and the rock pores were saturated with water, in the same manner as *Yokoyama* (2013). To adjust $S_{\text{pre-flow}}$ to 51%, the sample was saturated with water and dried at ambient temperature until $S_{\text{pre-flow}}$ became 51%. For $S_{\text{pre-flow}}$ = 0%, the sample was dried in an oven at 70°C until the weight was stabilized. The same sample (FS-1) was used for each $S_{\text{pre-flow}}$. The experiment started at $S_{\text{pre-flow}}$ = 51% was duplicated to verify the reproducibility. Ultrapure water (Milli-Q, 18.2 MΩ) was employed throughout the experiments.

Fig. 4.2 is a schematic of the apparatus used for the flow-through dissolution experiment. The sample FS-1 was installed in the sample holder immediately after adjusting $S_{\text{pre-flow}}$. Under an unsaturated condition, flow occurs either as uniform flow or preferential (bypass) flow (*Hendrickx and Flury*, 2001). The preferential flow is furthermore categorized as macropore flow and unstable flow (*Wang et al.*, 1998a). When water infiltrates to a downward direction, unstable flow has been known to occur depending on flow rate and $S_{\text{pre-flow}}$ (e.g., *Diment and Watson*, 1985; *Wang et al.*, 1998a; *Wang et al.*, 1998b) even if the sample has homogeneous pore structure (i.e., without macropores and cracks). In this study, to conduct the experiment under a uniform flow condition, we first started the experiment using the setup shown in Fig. 4.2b. Pure water was flowed from the bottom to the top of the sample at 22 ± 1 °C by applying a constant water head difference of ΔH = 9.7 cm, equivalent to a water pressure of 950 Pa ($\Delta H \rho_{\text{w}} g$, the gravitational acceleration g = 9.81 m s^{-2}). The water level was kept constant by continuously pumping water into the bottle of the constant water level part (Fig. 4.2) so that the water overflowed from the bottle. As water infiltrated into the sample, water extruded some of the air in the pores, resulting in a water saturation change. To monitor changes in water saturation, the sample was weighed at intervals. Water saturation significantly changed in several minutes from the onset of the experiment, after which the changes became small (data shown in section 4.3.1). We considered that the flow reached a quasi-steady state within the first several minutes, and the sample holder was turned over to collect effluent water (Fig. 4.2a). The output solution pooled in the bottle below the sample holder was periodically collected,

and its weight was measured by a digital balance to determine flow rate. The solution was filtered by a 0.22 μm filter, and the concentration of Si was measured with a liquid chromatography instrument (ICA2000; TOA DKK) by the molybdenum blue method (post-column reaction) using a UV/VIS detector (UV-2075 plus; Jasco). The error in concentration measurement was approximately 8–14%, which was larger than typical errors (3–4%) because the concentrations of Si in the output solutions were close to the lower detection limit (ca. 3.5×10^{-7} mol kg^{-1}). The concentrations of Si in some of the solutions were less than the lower detection limit. For such case the solutions were condensed in an oven at 80°C while flowing dehumidified air filtered at 1 μm, and the concentration was increased by 3–15 times. To check for Si contamination during condensation, ultrapure water was condensed in the same manner as that described above. The concentration of Si in ultrapure water, including both the effects of contamination from the outside and inherent concentration, was lower than ca. 3.5×10^{-9} mol kg^{-1}; this leads to an overestimation of the concentrations of Si in the collected solutions (mainly at S = 100%) by less than 6% because the measured concentrations were higher than 5.8×10^{-8} mol kg^{-1}. We also confirmed the validity of condensation by measuring the Si concentration of the solution that was made by condensing the solution of a known Si concentration; the measured value agreed with the expected value within the measurement error.

To describe the concentration dependence of the mineral dissolution rate r (mol m^{-2} s^{-1}), the following equation is one of the commonly used forms (*Steefel and van Cappellen*, 1990):

$$r = r_{\text{const}}\left(1 - \Omega^{m}\right)^{n} \tag{4.2}$$

where r_{const} is the dissolution rate constant (mol m^{-2} s^{-1}), $\Omega = IAP/K_{\text{eq}}$ is the saturation index of the mineral, IAP is the activity product, K_{eq} is the equilibrium constant, and m and n are the fitting parameters. For the dissolution of quartz, Ω is equal to $c/c_{\text{eq}}^{\text{Qz}}$ and m = n = 1 (*Berger*, 1994; *Schott et al.*, 2009), where c is the Si concentration and $c_{\text{eq}}^{\text{Qz}}$ is the Si concentration in equilibrium with quartz. r is equal to r_{const} at $c \ll c_{\text{eq}}^{\text{Qz}}$. When water infiltrates into the rock, dissolution occurs at the position where water contacts mineral, and solution containing the dissolved Si flows out from the rock. At a water saturation S, the overall dissolution rate R_{S} (mol s^{-1}) (the dissolution rate of the whole rock core) is given by the following equation:

$$R_{S} = A_{S} r_{\text{const}} = Q_{S} \Delta c_{S} \tag{4.3}$$

where A_S (m^2) is the reactive surface area, Q_S (kg s^{-1}) is the mass flow rate passing through the rock, and Δc_S (mol kg^{-1}) is the difference in Si concentration between the input and the output solutions (subscript S indicates the value at S). The values of Q_S and Δc_S (thus, R_S) can be directly determined by the flow-through experiment. Let us suppose we measure $Q_{S=100\%}$, $\Delta c_{S=100\%}$ and Q_S, Δc_S (S can be any value of $0 < S < 100\%$). Then, we can evaluate the extent to which A_S is smaller than $A_{S=100\%}$ by the following relationship derived using Eq. (4.3): $A_S / A_{S=100\%} = (Q_S \Delta c_S)/(Q_{S=100\%} \Delta c_{S=100\%})$ (note r_{const} does not depend on S as long as dissolution occurs at far from equilibrium condition).
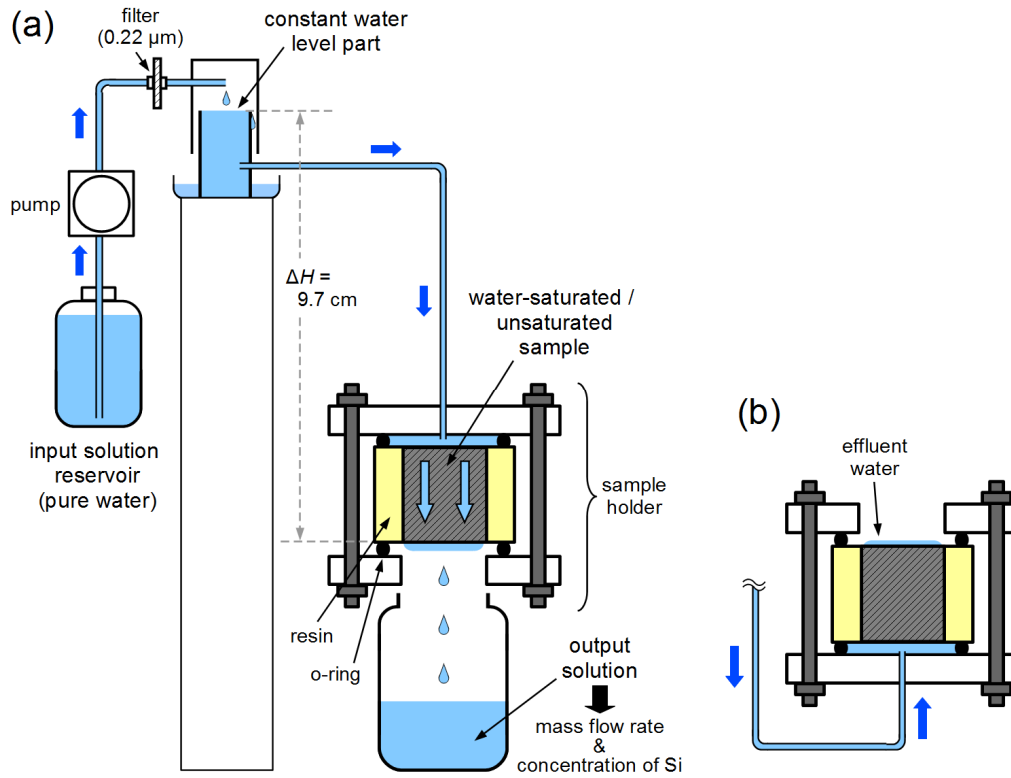
Fig. 4.2. Schematic of the apparatus used for the flow-through dissolution experiment.

4.2.3. Visualization of Pore Water and Air during Flow-through Experiment

To evaluate how water and air are distributed in the rock under unsaturated conditions, flow paths were visualized by dye solution using the same experimental setup as the flow-through dissolution experiment (Fig. 4.2b). Methylene blue solutions have been used for visualizing flow paths in porous media (e.g., *Sygouni et al.*, 2006; *Schneider et al.*, 2011) and we used this method. A methylene blue aqueous solution

(8.1 g L^{-1}) was infiltrated from the bottom of the dried sample (sample FS-2 at $S_{\text{pre-flow}}$ = 0%) by applying a constant water head difference of 10 cm. To monitor how the solution discharges, the top of the sample was intermittently photographed using a digital microscope (Dino-Lite, AnMo Electronics Corp.). After approximately 4 hours passed, the sample was taken out from the sample holder and weighed to determine the water saturation. Then, the sample was immediately cut in the direction parallel to the flow by a flat chisel and the cut surface was photographed using the digital microscope.

4.3. Results
4.3.1. Water Saturation

Fig. 4.3a shows the temporal changes in water saturation. At $S_{\text{pre-flow}}$ = 0% and 51%, the water saturation increased rapidly within several minutes from the onset of the experiment. The saturations were still changing after several hours had elapsed, but the changes were much smaller. As a representative saturation in each experiment at $S_{\text{pre-flow}}$ = 0% and 51%, S_{flow} is defined as an average value of water saturation after the inflow (S_{flow} = 46% and 76% at $S_{\text{pre-flow}}$ = 0% and 51%, respectively) and hereafter the data are presented using S_{flow}. The changes in water saturation indicated that some of the air was extruded by percolating water while other air was enclosed by water and immobilized, especially at the onset of the experiment. Such air is referred to as "entrapped air" (*Faybishenko*, 1995). *Suzanne et al.* (2003) measured the amount of entrapped air using Fontainebleau sandstone having a porosity of 8.5% and reported that air was trapped in 69% and 38% of the pore space for $S_{\text{pre-flow}}$ = 6% and 50%, respectively. Our result, air was trapped in 60% and 32% of the pore space immediately after the infiltration at $S_{\text{pre-flow}}$ = 0% and 51%, generally agrees with the reported values. Although some difference exists, this may be due to the difference in fluids used (they used oil (strongly wetting for rock) as substitute for water).

4.3.2. Mass Flow Rate

Fig. 4.3b shows the temporal changes in the mass flow rate. The lower the S_{flow} is, the lower the flow rate. The flow rates at S_{flow} = 46% and 76% were respectively 5–7% and 20–34% of the flow rate at S_{flow} = 100%. The results of the first and second runs started at $S_{\text{pre-flow}}$ = 51% was highly reproducible, both for water saturation and the flow rate (Figs. 4.3a and b). As time passed, the flow rate at S_{flow} = 46% moderately decreased, whereas that at S_{flow} = 76% slightly increased. The changes in

flow rate with time may be related to the reduction in the entrapped air due to dissolution into the pore solution and/or due to the migration of entrapped air to different positions. Because the changes in water saturation and flow rate after the initial rapid changes were small (Figs. 4.3a and b), it seemed that stable flow paths were formed and maintained for at least the time period of our experiment (~3 days).

4.3.3. Concentration of Dissolved Si

Fig. 4.3c shows the temporal changes of the Si concentration in the output solutions. For all experiments started at different $S_{\text{pre-flow}}$, the Si concentration initially decreased by a factor of 3–5. The changes became moderate after approximately 20 hours passed. The results of the first and second runs started at $S_{\text{pre-flow}}$ = 51% were highly reproducible. The Si concentration in equilibrium with quartz under our experimental condition (22 °C and pH 6) was 8.9×10^{-5} mol kg^{-1}, which was calculated using PHREEQC software (*Parkhurst and Appelo*, 1999) with the minteq database. At any S_{flow}, the Si concentration in the output solution was significantly lower than the equilibrium Si concentration ($c/c_{\text{eq}}^{\text{Qz}}$ = 0.03–0.002 for the initial 20 hours, and $c/c_{\text{eq}}^{\text{Qz}}$ = 0.01–0.0007 for the latter period), and the effect of Ω on the dissolution rate was fairly small.
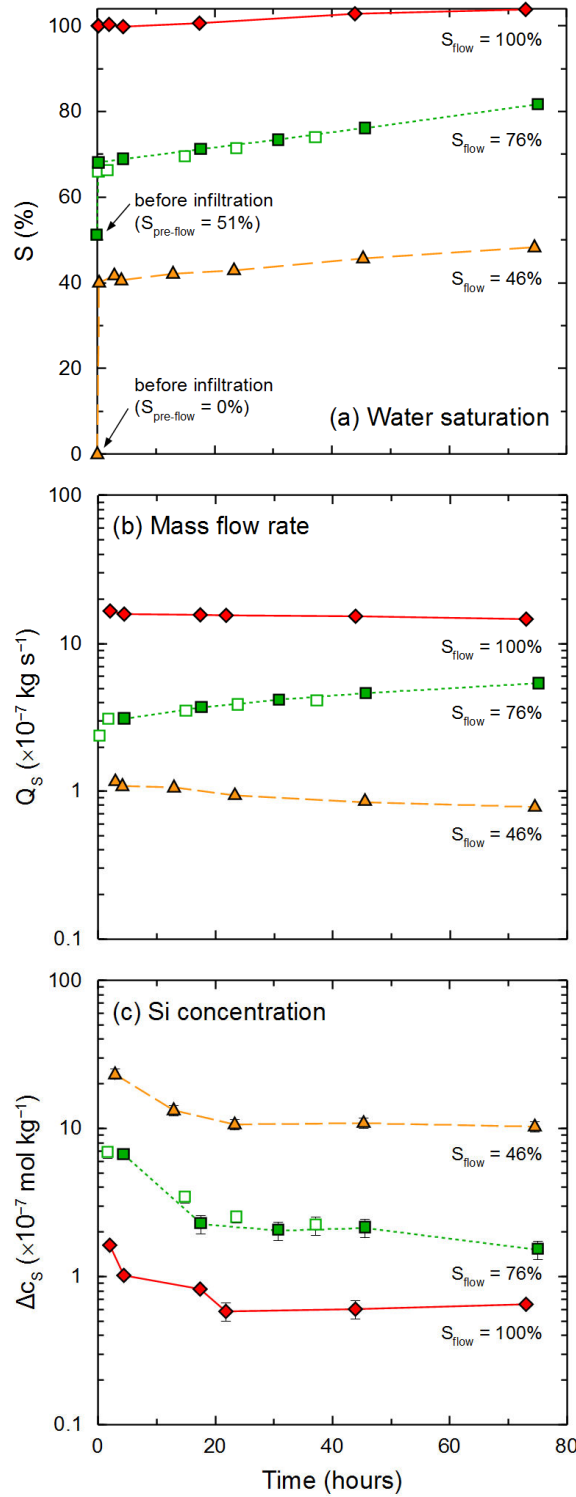
Fig. 4.3. Temporal evolutions of the water saturation S (a), the mass flow rate Q_S (b), and the dissolved Si concentration in the outlet solution Δc_S (c) after water infiltrates into the sample having $S_{\text{pre-flow}}$ = 0, 51, and 100%. The open square represents the second run started at $S_{\text{pre-flow}}$ = 51%.

4.3.4. Distribution of Flow Paths in the Water-unsaturated Sample

Fig. 4.4a is a photograph of the top of the sample (FS-2) before the infiltration of the methylene blue solution ($S_{\text{pre-flow}}$ = 0%) and Figs. 4.4b and c are those after the discharge of the solution (S_{flow} = 37%). The upper surface was wholly stained by the solutions discharged from many pores (Figs. 4.4a–c). Some of the discharged solutions gathered each other and spread widely (Figs. 4-4b and c). From Fig. 4.4c, the spacing between flow paths was roughly estimated to be 0.3–3 mm. Therefore, at least flow does not occur only at several preferential paths, although difference in the size of droplets indicates the variation of flow rate. Fig. 4.4d shows the cut surface of the sample (cut parallel to the direction of water flow). The blue portions correspond to the positions where water passed, whereas the uncolored portions correspond to the positions where air was trapped (or isolated pores). The uncolored areas with sizes of a few hundred micrometers can be found throughout the cross section, and those with larger sizes (a few millimeters) are also present locally. *Kumar et al.* (2010) performed water-injection experiments using Fontainebleau sandstone cores having different porosities (14% and 19%) and measured the size of entrapped air using X-ray microtomography. For both porosities, the main sizes of the entrapped air were 0.1–1 mm but larger air having a length of approximately 2 mm was also observed. Our observation is consistent with the result of *Kumar et al.* (2010).

75
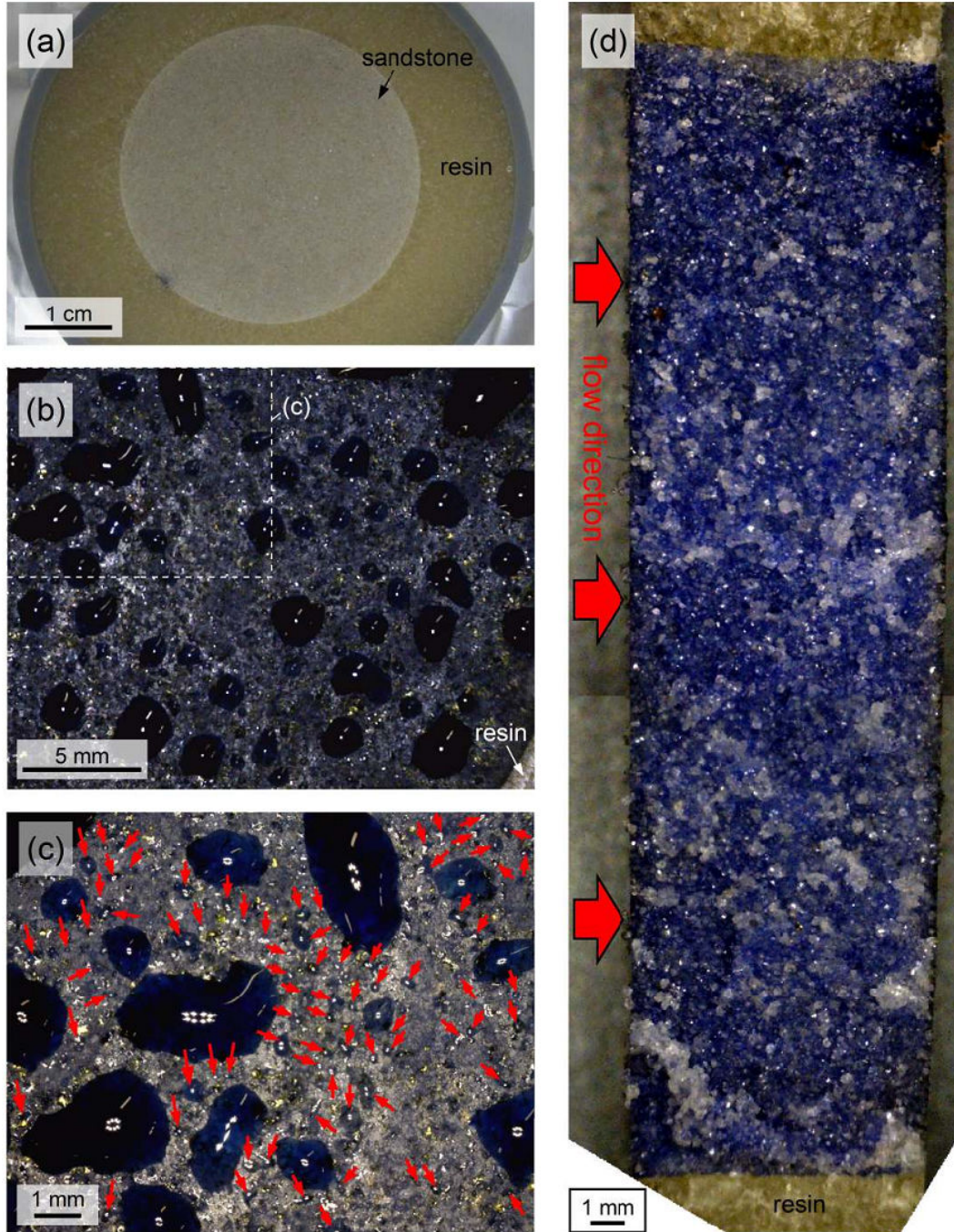
Fig. 4.4. Images of the top of the sample FS-2 (a) before ($S_{pre\text{-}flow}$ = 0%) and (b, c) after the infiltration of dye solution (S_{flow} = 37%). In (c), positions of small droplets are highlighted by red arrows as a guide for identifying them. (d) Image of the cut surface of the sample at S_{flow} = 37% parallel to the flow direction. The direction of the injection of water is shown as arrows.

4.3.5. Dissolution Rate under Water-saturated and Unsaturated Conditions

The overall dissolution rate at each water saturation, determined from the flow rate and dissolved Si concentration, is shown in Fig. 4.5. For all experiments started at different $S_{\text{pre-flow}}$, the temporal change in the overall dissolution rate showed a similar trend; the rates decreased during the initial 20 hours and then became approximately stable. After an almost constant rate was attained, the values obtained were $R_{S_{\text{flow}}=100\%} = (9.3 \pm 0.2) \times 10^{-14}$, $R_{S_{\text{flow}}=76\%} = (8.8 \pm 0.9) \times 10^{-14}$ (first run at $S_{\text{pre-flow}} = 51\%$), $R_{S_{\text{flow}}=71\%} = (9.3 \pm 0.3) \times 10^{-14}$ (second run at $S_{\text{pre-flow}} = 51\%$), and $R_{S_{\text{flow}}=46\%} = (9.0 \pm 1.0) \times 10^{-14}$ mol s^{-1}. Hence, the overall dissolution rates at each S_{flow} were almost equal. In addition to the comparison of the steady state dissolution rate, we compared the total amount of dissolved Si in the initial 22–24 hours of the experiment at each S_{flow}; the obtained values were 1.0×10^{-8}, 0.98×10^{-8}, and 1.1×10^{-8} mol at $S_{\text{flow}} = 100$, 71 (second run at $S_{\text{pre-flow}} = 51\%$), and 46%, respectively. Thus, the amount of dissolution did not depend on water saturation even before reaching the steady state.

As the composition of Fontainebleau sandstone is almost 100% quartz, we determined the dissolution rate of quartz normalized to a BET surface area by using the results of the flow-through dissolution experiment and compared it with the previously reported dissolution rate constant of quartz. At $S_{\text{flow}} = 100\%$, all quartz surfaces can be regarded as wet and reactive. Fig. 4.6 shows the dissolution rates calculated by Eq. (4.3) using the results at $S_{\text{flow}} = 100\%$ ($Q_{S_{\text{flow}}=100\%}$ and $\Delta c_{S_{\text{flow}}=100\%}$) and the surface area measured by the BET method (0.10 m^2 g^{-1} × 21.8 g = 2.25 m^2). The dissolution rate decreased for approximately 20 hours from the onset of the experiment and then approached an almost stable value. The dissolution rate at a quasi-steady state computed after ~20 hours of reaction was 4.1×10^{-14} mol m^{-2} s^{-1}. Quartz dissolution rates in pure water at 23 °C were previously reported by *Tester et al*. (1994) to be $5.8 \times 10^{-15} - 3.5 \times 10^{-14}$ mol m^{-2} s^{-1} as shown in the grey area in Fig. 4.6. The rate in this study is slightly higher than the reported ones but is still in reasonably good agreement.
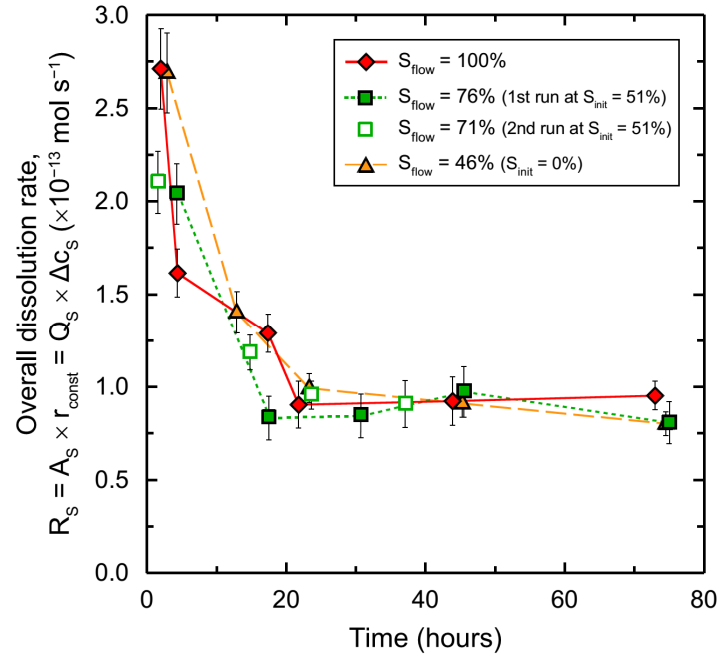
Fig. 4.5. Temporal evolutions of the overall dissolution rate R_S after water infiltrates into the sample having $S_{\text{pre-flow}} = 0$, 51, and 100%.
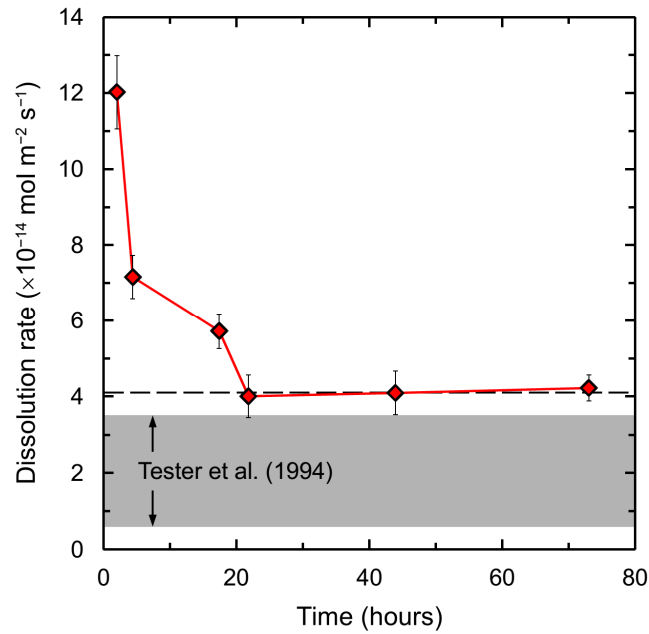

Fig. 4.6. Changes in the dissolution rate of Fontainebleau sandstone normalized to BET surface area with elapsed time. The dashed line represents the dissolution rate at a quasi-steady state. The gray area corresponds to the quartz dissolution rates reported by *Tester et al.* (1994).

4.4. Reactive Transport in Water Film and Its Relevance to Reactive Surface Area

The results of the flow-through dissolution experiment using Fontainebleau sandstone indicated that the reactive surface area was unaffected by water saturation. Even if air occupies the pores, dissolution can proceed as long as the mineral surfaces are wetted by water film. Thus, the presence of wetting film is the most likely explanation for our experimental results. In addition, the results suggest that the flushing of dissolved Si from the interior of the film to the flow paths is fast enough to keep the concentration of Si in the water film far lower than the equilibrium concentration of quartz. The roles of water film in reaction and transport have been considered also in several previous studies, such as in the cases of the dissolution and growth of calcite (single crystal) exposed to air (*Stipp et al.*, 1996; *Hausner et al.*, 2007), diffusion of solutes (*Schaefer et al.*, 2000; *Hu and Wang*, 2003) and electron conduction (*Han et al.*, 2009) in porous media. Our experimental results provide a new perspective that water film plays an essential role in the dissolution behavior in rock pores under water-unsaturated conditions.

4.5. Conclusions

To determine the relationship between water saturation and reactive surface area, flow-through dissolution experiments were conducted at initial water saturations of 0, 51, and 100% using Fontainebleau sandstone consisting of ~100% quartz. The total amount of dissolution did not decrease with decreasing water saturation, which indicated that the reactive surface area remained constant because all of the mineral surfaces were wetted with water film even though air was present in the pores under low water saturation. Furthermore, the experimental data suggest that the flushing of dissolved Si from the interior of the film to the exterior was fast enough to maintain a low concentration compared to the equilibrium concentration of quartz. It can be therefore concluded that the reactive-transport in water film plays an important role for considering the reactive surface area of water-unsaturated rocks.

References

Berger G., Cadore E., Schott J. and Dove P. (1994) Dissolution rate of quartz in lead and sodium electrolyte solutions between 25 and 300°C. Effect of the nature of surface complexes and reaction affinity. *Geochim. Cosmochim. Acta* **58**, 541–551.

Bourbie T. and Zinszner B. (1985) Hydraulic and acoustic properties as a function of porosity in Fontainebleau sandstone. *J. Geophys. Res.* **90**, 11524–11532.

Colon C. F. J., Oelkers E. H. and Schott J. (2004) Experimental investigation of the effect of dissolution on sandstone permeability, porosity, and reactive surface area. *Geochim. Cosmochim. Acta* **68**, 805–817.

Diment G. A. and Watson K. K. (1985) Stability analysis of water movement in unsaturated porous materials: 3. Experimental studies. *Water Resour. Res.* **21**, 979–984.

Doyen P. M. (1988) Permeability, conductivity, and pore geometry of sandstone. *J. Geophys. Res.* **93**, 7729–7740.

Faybishenko B. (1995) Hydraluic behavior of quasi-saturated soil in the presence of entrapped air: laboratory experiments. *Water Resour. Res.* **31**, 2421–2435.

Han M., Youssef S., Rosenberg E., Fleury M. and Levitz P. (2009) Deviation from Archie's law in partially saturated porous media: wetting film versus disconnectedness of the conducting phase. *Phys. Rev. E* **79**, 031127.

Hausner D. B., Reeder R. J. and Strongin D. R. (2007) Humidity-induced restructuring of the calcite surface and the effect of divalent heavy metals. *J. Colloid Interface Sci.* **305**, 101–110.

Hendrickx J. M. H. and Flury M. (2001) Uniform and preferential flow mechanisms in the vadose zone. In *Conceptual models of flow and transport in the fractured vadose zone*. (eds. National Research Council). National Academy Press, Washington DC. pp. 149–187.

Hodson M. E. (2006) Does reactive surface area depend on grain size? Results from pH 3, 25°C far-from-equilibrium flow-through dissolution experiments on anorthite and biotite. *Geochim. Cosmochim. A*cta **70**, 1655–1667.

Hu Q. and Wang J. S. Y. (2003) Aqueous-phase diffusion in unsaturated geologic media: a review. *Crit. Rev. Environ. Sci. Technol.* 33, 275–297.

Kieffer B., Jove C. F., Oelkers E. H. and Schott J. (1999) An experimental study of the reactive surface area of the Fontainebleau sandstone as a function of porosity, permeability, and fluid flow rate. *Geochim. Cosmochim. Acta* **63**, 3525–3534.

Kumar M., Senden T., Sheppard A., Middleton J. and Knackstedt M. (2010) Visualizing and quantifying the residual phase distribution in core material. *Petrophysics*. **51**, 323–332.

Nishiyama N., Yokoyama T. and Takeuchi S. (2012) Size distributions of pore water and entrapped air during drying-infiltration processes of sandstone characterized by water-expulsion porosimetry. *Water Resour. Res.* **48**, W09556.

Noiriel C., Gouze P. and Bernard D. (2004) Investigation of porosity and permeability effects from microstructure changes during limestone dissolution. *Geophys. Res. Lett.* **31**, L24603.

Pačes T. (1983) Rate constant of dissolution derived from the measurements of mass balance in

hydrological catchments. *Geochim. Cosmochim. Acta* **47**, 1855–1863.

Parkhurst, D. L. and Appelo, C. A .J. (1999) User's guide to PHREEQC (Version 2)— A computer program for speciation, batch-reaction, one-dimensional transport, and inverse geochemical calculations. Water-Resources Investigations Report 99–4259, pp. 312.

Saripalli K. P., Freedman V. L., McGrail B. P. and Meyer P. D. (2006) Characterization of the specific solid-water interfacial area-water saturation relationship and its import to reactive transport. *Vadose Zone J.* **5**, 777–783.

Schaefer C. E., DiCarlo D. A. and Blunt M. J. (2000) Experimental measurement of air-water interfacial area during gravity drainage and secondary imbibition in porous media. *Water Resour. Res.* **36**, 885–890.

Schneider M., Osselin F., Andrews B., Rezgui F. and Tabeling P. (2011) Wettability determination of core samples through visual rock and fluid imaging during fluid injection. *J. Pet. Sci. Eng.* **78**, 476–485.

Schnoor J. L. (1990) Kinetics of chemical weathering: a comparison of laboratory and field rates. In *Aquatic Chemical Kinetics*. (eds. W. Stumm). Wiley, New York. pp. 475–504.

Schott J., Pokrovsky O. S. and Oelkers E. H. (2009) The link between mineral dissolution/precipitation kinetics and solution chemistry. In *Reviews in Mineralogy*, vol. 70 (eds. E. H. Oelkers and J. Schott) Mineral. Soc. Amer. pp. 207–258.

Scislewski A. and Zuddas P. (2010) Estimation of reactive mineral surface area during water-rock interaction using fluid chemical data. *Geochim. Cosmochim. Acta* **74**, 6996–7007.

Steefel C. I. and van Cappellen P. (1990) A new kinetic approach to modeling water-rock interaction: The role of nucleation, precursors, and Ostwald ripening. *Geochim. Cosmochim. Acta* **54**, 2657–2677.

Stipp S. L. S., Gutmannsbauer W. and Lehmann T. (1996) The dynamic nature of calcite surfaces in air. *Am. Mineral.* **81**, 1–8.

Suzanne K., Haman G., Billiotte J. and Trocme V. (2003) Experimental relationships between residual gas saturation and initial gas saturation in heterogeneous sandstone reservoirs. Paper presented at SPE Annual Technical Conference and Exhibition, SPE, Denver, Colorado.

Swoboda-Colberg N. H. and Drever J. I. (1993) Mineral dissolution rates in plot-scale field and laboratory experiments, *Chem. Geol.* **105**, 51–69.

Sygouni V., Tsakiroglou C. D. and Payatakes A. C. (2006) Capillary pressure spectrometry: Toward a new method for the measurement of the fractional wettability of porous media. *Phys. Fluids* **18**, 053302.

Tester J. W., Worley W. G., Robinson B. A., Grigsby C. O. and Feerer J. L. (1994) Correlating quartz dissolution kinetics in pure water from 25 to 625°C. *Geochim. Cosmochim. Acta* **58**,

2407–2420.

Thompson A. H., Katz A. J. and Krohn C. E. (1987) The microgeometry and transport properties of sedimentary rock. *Adv. Phys.* **36**, 625–694.

Velbel M. A. (1985) Geochemical mass balances and weathering rates in forested watersheds of the southern blue ridge. *Amer. J. Sci.* **285**, 904–930.

Wang Z., Feyen J. and Ritsema C. J. (1998a) Susceptibility and predictability of conditions for preferential flow. *Water Resour. Res.* **34**, 2169–2182.

Wang Z., Feyen J. and Elrick D. E. (1998b) Prediction of fingering in porous media. *Water Resour. Res.* **34**, 2183–2190.

White A. F. and Brantley S. L. (2003) The effect of time on the weathering of silicate minerals: why do weathering rates differ in the laboratory and field? *Chem. Geol.* **202**, 479–506.

White A. F. and Peterson M. L. (1990) Role of reactive-surface-area characterization in geochemical kinetic models. *In Chemical modeling of aqueous systems II.* ACS symposium series 416. Eds. D. C. Melchior and R. L. Bassett. 461–475.

Yokoyama T. and Banfield J. F. (2002) Direct determinations of the rates of rhyolite dissolution and clay formation over 52,000 years and comparison with laboratory measurements. *Geochim. Cosmochim. Acta* **66**, 2665–2681.

Yokoyama T. and Takeuchi S. (2009) Porosimetry of vesicular volcanic products by a water-expulsion method and the relationship of pore characteristics to permeability. *J. Geophys. Res.* **114**, B02201.

Yokoyama T. (2013) Characterization of the reaction and transport properties of porous rhyolite and its application to the quantitative understanding of the chemical weathering rate. *Geochim. Cosmochim. Acta* **118**, 295–311.

Zhu C. (2005) In situ feldspar dissolution rates in an aquifer. *Geochim. Cosmochim. Acta* **69**, 1435–1453.

Zimmerman R. W. and Bodvarsson G. S. (1989) An approximate solution for one-dimensional absorption in unsaturated porous-media. *Water Resour. Res.* **25**, 1422−1428.

Chapter 5

Estimation of Thickness of Water Film on Pore Wall Associated with the Occurrence of Air Entrapment

Abstract

When water and entrapped gas co-exist in pore spaces of a geological medium, a water film is formed on grain surfaces and plays an important role in chemical reaction and mass transport. We developed a model to estimate the film thickness in a geological medium using a concept of disjoining pressure associated with the electric double layer force and van der Waals force. Water film is assumed to be in equilibrium with water vapor in entrapped gas. By using the Kelvin equation which relates pore size to relative humidity, we obtained an expression describing the relationship between the water film thickness, relative humidity, and pore diameter. The model indicates that to know the pore sizes at which gas is trapped is important for estimating the thickness of the water film under the occurrence of gas entrapment. The model shows that larger pores have thicker water film. We also discussed the dependence of film thickness on pore size using hypothetical pore size distributions of rocks.

5.1. Introduction

When water infiltrates into a dry or partially saturated geological medium, some of gas (e.g., air) is confined by water and remains in pore spaces. Such gas, often referred to as "entrapped gas", is known to influence the permeability of geological media (e.g., *Nishiyama et al.*, 2012) and is becoming an effective mechanism in the storage of CO_2 in aquifers (e.g., *Pentland et al.*, 2011). Previous experimental studies using sandstone (*Nishiyama and Yokoyama*, 2013) and rhyolite (*Yokoyama and Nishiyama*, 2013) have found that the reactive (mineral-water contact) surface area of the rocks in the presence of entrapped air was almost identical to that under water-saturated condition. These findings have suggested that even if air is trapped in pores, the pore walls are wetted by water film and mineral-water interaction can proceed. *Nishiyama and Yokoyama* (2013) have shown that the thickness of water film on mineral surface in an unsaturated rock is a controlling factor of the dissolution rate of the mineral. This means that the estimation of the film thickness is important in the quantitative understandings of the reactive-transport behavior in the vadose zone.

Earlier experimental studies have estimated the thickness of water film adsorbed on mineral plates as a function of relative vapor pressure or the pressure in water film (e.g., *Pashley and Kitchener*, 1979; *Bohr et al.*, 2010). The relationship between film thickness and the pressure in the film associated with electric double layer and van der Waals forces have been also theoretically considered on the basis of Derjaguin-Landau-Verwey-Overbeek (DLVO) theory (e.g., *Derjaguin and Churaev*,

1974; *Churaev*, 2003). Recently, some studies have applied the DLVO theory for predicting the film thickness in geological media under the conditions including water drainage and imbibition events (*Tuller et al.*, 1999; *Tokunaga*, 2011), injection of gaseous/supercritical CO_2 into water-bearing media (*Tokunaga*, 2012), and extraction of pore water by centrifugation (*Yokoyama et al.*, 2011). Under these conditions, gas is connected to atmosphere but not trapped in pores. On the other hand, to our knowledge, no previous work has addressed the thickness of the water film under the condition that gas is trapped in pores. In this study, we focus on the water film present between minerals and entrapped gas, and try to evaluate the water film thickness based on the DLVO theory.

5.2. Model to Estimate Thickness of Water Film between Grain Surfaces and Entrapped Gas

To estimate the thickness of water film by applying the DLVO theory, we assume that the water film between mineral grain and entrapped gas is in equilibrium with the water vapor in the gas. The vapor pressure depends on the curvature of the meniscus formed at the interface between gas and water (Fig. 5.1a). Assuming that the curvature is equivalent to the pore radius $d_{pore}/2$ (m), the relative vapor pressure p/p_{sat} in the gas can be related to d_{pore} using the Kelvin equation:

$$\frac{RT}{V_w}\ln\left(\frac{p}{p_{sat}}\right) = \frac{RT}{V_w}\ln\left(\frac{RH}{100}\right) = -\frac{4\gamma}{d_{pore}} \tag{5.1}$$

where R is the gas constant (J K^{-1} mol^{-1}), T is the absolute temperature (K), V_w is the molar volume of water (= 1.8×10^{-5} m^3 mol^{-1} at 25°C), p is the vapor pressure in the entrapped gas (Pa), p_{sat} is the saturated vapor pressure (Pa), RH is the relative humidity (%), and γ is the water-gas interfacial tension (N m^{-1}). Based on Eq. (5.1), p/p_{sat} in the entrapped gas is less than 1 (i.e., $RH < 100\%$) and the degree of deviation of p from p_{sat} depends on d_{pore}.

The water film on a solid surface is subject to a force perpendicular to the plane of the film as it opposes film thinning, owing to the interfacial interactions between solid/water film/gas. The pressure due to this force is termed as disjoining pressure Π (Pa) (e.g., *Derjaguin and Churaev*, 1974). When equilibrium is attained between water film and surrounding vapor, Π is related to the relative vapor pressure (*Tuller et al.*, 1999; *Churaev*, 2003; *Mercury and Nakashima*, 2004):

$$\Pi = -\frac{RT}{V_w} \ln\left(\frac{p}{p_{sat}}\right) \tag{5.2}$$

Π is a function of the film thickness h (m) and determined by the summation of interaction forces, usually electrostatic, van der Waals, and structural forces (*Derjaguin and Churaev*, 1974):

$$\Pi(h) = \Pi_e(h) + \Pi_m(h) + \Pi_s(h) \tag{5.3}$$

where $\Pi_e(h)$, $\Pi_m(h)$, and $\Pi_s(h)$ are the electrostatic, molecular, and structural components, respectively. We consider only $\Pi_e(h)$ and $\Pi_m(h)$ in the same way as the work of *Lebeau and Konrad* (2010) and *Tokunaga* (2011).

$\Pi_e(h)$ originates from the compression of the electric double layer into a confined space (compare Figs. 5.1b and c). To describe the film thickness for a low-concentration aqueous solution adsorbed on the surface with a high electrostatic potential, the following simple electric double layer model was developed by *Langmuir* (1938):

$$\Pi_e(h) = \frac{\varepsilon_r \varepsilon_0}{2}\left(\frac{\pi k_B T}{eZ}\right)^2 \frac{1}{h^2} \tag{5.4}$$

where ε_r is the static relative permittivity of water (= 78.41 at 25°C), ε_0 is the permittivity of free space (= 8.85×10^{-12} C^2 J^{-1} m^{-1}), k_B is the Boltzmann constant (= 1.38×10^{-23} J K^{-1}), e is the electron charge (= 1.60×10^{-19} C), and Z is the ion valence. $\Pi_m(h)$ is due to dipole-dipole interactions between solid/water/gas and is given by

$$\Pi_m(h) = -\frac{A_{svl}}{6\pi h^3} \tag{5.5}$$

where A_{svl} (J) is the Hamaker constant for solid-vapor interactions through the intervening liquid. The range of the A_{svl} of some minerals reported in *Tokunaga* (2011) is $-6.0 \times 10^{-21} - -4.5 \times 10^{-20}$ J (Table 5.1). The inset of Fig. 5.2 shows Π, Π_e, and Π_m as a function of h for quartz-water-air system at 25°C. The thickness of water film, especially for >10 nm, is mostly controlled by the electric double-layer force. The comparison of experimentally measured relationship between Π and h with that predicted by Eqs. (5.2)–(5.5) demonstrates the validity of the theories (Fig. 5.2).

By combining Eqs. (5.1)–(5.5), we have:

$$\frac{\varepsilon_r \varepsilon_0}{2}\left(\frac{\pi k_B T}{eZ}\right)^2 \frac{1}{h^2} - \frac{A_{svl}}{6\pi h^3} = \frac{4\gamma}{d_{pore}}$$

(5.6)

Using this equation, we can determine h with a given d_{pore}, mineral, and solution. This equation shows that the film thickness for a given mineral and solution composition is controlled by the diameter of the pore in which gas is trapped. There is a possibility that h is affected by other factors such as surface roughness and shape of pore, but these effects are not considered. It should be noted that the use of the above equations may result in a thinner thickness than the actual value as experimental evaluations yielded thicker film than that predicted by the Langmuir model for $h < 30$ nm (*Israelachvili*, 1992).

Table 5.1. Hamaker constants (A_{slv}) of various minerals reported by *Tokunaga* (2011).

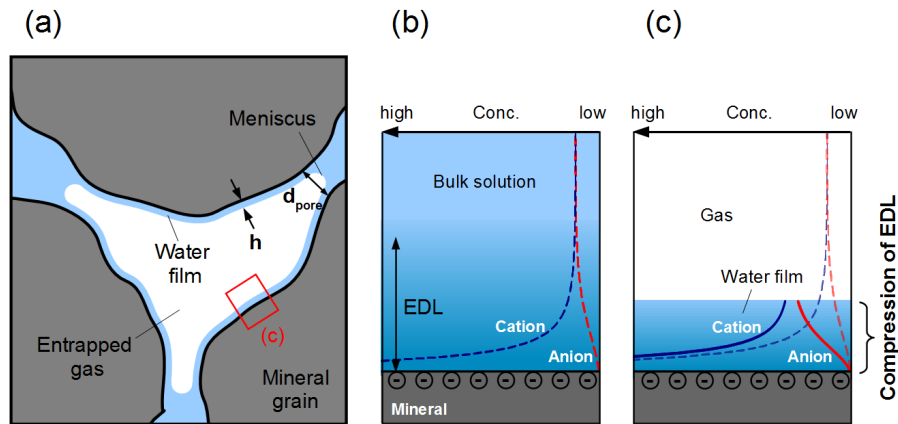| Mineral	A_{slv} (J)
SiO$_2$	$-6.0 \times 10^{-21} - -1.3 \times 10^{-20}$
Al$_2$O$_3$	-4.1×10^{-20}
α-Al$_2$O$_3$	$-3.8 \times 10^{-20} - -3.9 \times 10^{-20}$
α-FeOOH (goethite)	-4.5×10^{-20}
TiO$_2$	-3.7×10^{-20}
Muscovite mica	$-2.4 \times 10^{-20} - -3.4 \times 10^{-20}$
Illite	-4.5×10^{-20}
Kaolinite	$-3.1 \times 10^{-20} - -4.2 \times 10^{-20}$
Montmorillonite	$-2.7 \times 10^{-20} - -4.9 \times 10^{-20}$
CaCO$_3$	$-2.4 \times 10^{-20} - -2.9 \times 10^{-20}$

Fig. 5.1. (a) Schematic of pore spaces where water and entrapped gas co-exist. Grain

surfaces are coated with water films. Schematic of electric double layer (EDL) near negatively charged solid surface for semi-finite system (b). In water film (c), EDL is compressed and thereby the disjoining pressure arises.
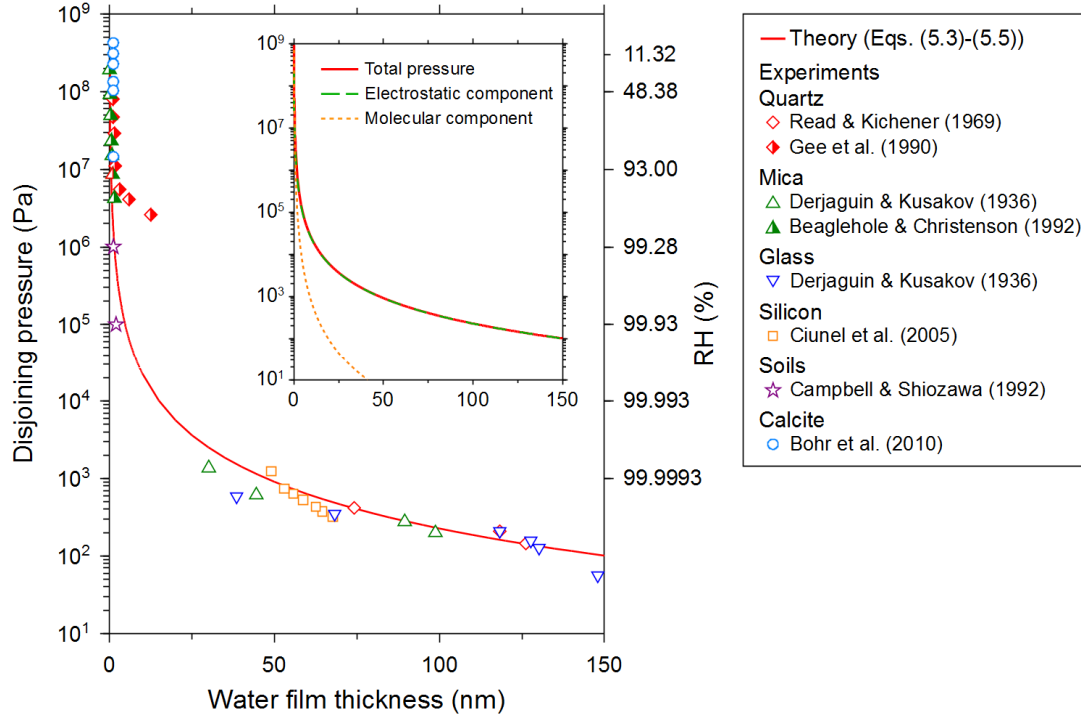

Fig. 5.2. Relationship between water film thickness (h) and disjoining pressure (Π) measured by experiments (points) and calculated by Eqs. (5.2)–(5.5) (line). Inset: h vs. Π and its electrostatic (Π_e) and molecular (Π_m) components, calculated for quartz–water–air system ($A_{svl} = -1.3 \times 10^{-20}$ J) at 25°C.

5.3. Results and Discussion

A geological medium usually has pores of various sizes. This means that the thickness of water film also has variation, because of the existence of the $h\text{-}d_{pore}$ relationship (Eq. (5.6)). To consider the variation of film thickness, we need the pore size distribution (PSD) of a geological medium of interest, which can be measured by the method such as mercury intrusion porosimetry. In this study we consider hypothetical pore size distributions (blue solid and dotted lines in Fig. 5.3). In addition, we need to know the pore sizes at which gas is trapped, which can be estimated either by theoretical calculation or by direct measurement of the size of entrapped gas (*Nishiyama et al.*, 2012 and Fig. 2.8 in this thesis). As a theoretical approach, *Parker*

and Lenhard (1987) introduced an assumption that each size of pore entraps gas in proportion to its volume, in an attempt to predict relative hydraulic conductivities. This assumption was used in this study as a first approximation. The solid line (red) in Fig. 5.3 calculated by Eq. (5.6) is the relationship between film thickness and pore diameter for "quartz–dilute 1:1 aqueous solution (Z = 1)–air" system at 25 °C, showing that larger pore has thicker film thickness. The range of the film thicknesses for a given geological medium can be determined by the range of the pore size, as is described as h_{max} and h_{min} in Fig. 5.3. The broader the pore size distribution, the broader the range of the film thickness (compare cases 1 and 2 in Fig. 5.3).

These results provide an insight into the role of water film in water-rock reaction. Because the efficiency of flushing of dissolved elements in a film will be lower in thinner film and thereby the concentration in the film will be subject to near the equilibrium concentration, the dissolution rate of the mineral coated with a water film will depend on pore diameter; the smaller the pores, the slower the dissolution rate. The model for estimating film thickness proposed in this study will be useful in considering the reaction and transport occurring in water film under the presence of entrapped gas.
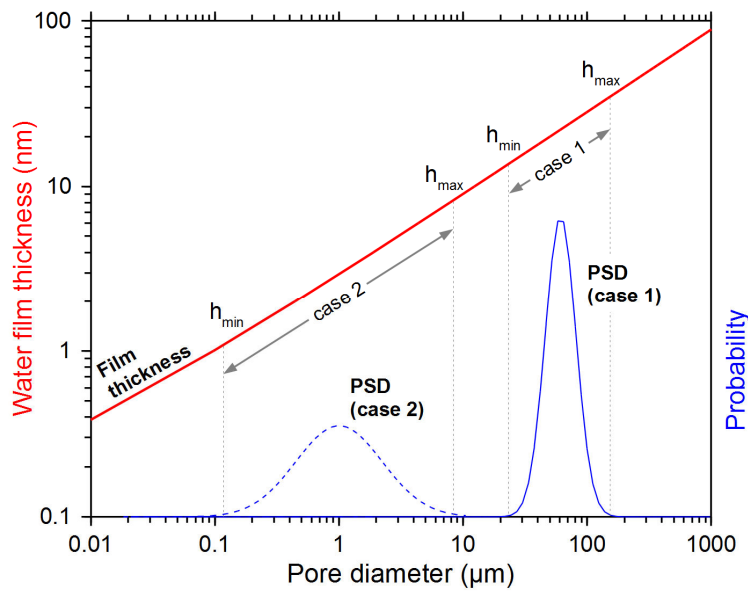

Fig. 5.3. Pore diameter (d_{pore}) vs. water film thickness (h) (red line). Hypothetical pore size distributions are also shown as blue solid and dotted lines.

5.4. Conclusions

We constructed a model to estimate the thickness of water film between mineral

grains and entrapped gas based on a concept of disjoining pressure associated with electric double layer force and van der Waals force. The model reveals that the water film thickness is controlled by pore diameter, mineral composition, and the type of ion in pore solution. Our model shows that larger pore has thicker film thickness. It also indicates that the broader the pore size distribution, the broader the range of the film thickness. The model proposed in the present study will be useful in considering the reaction and transport occurring in water film in a water-unsaturated rock.

References

Bohr J., Wogelius R. A., Morris P. M. and Stipp S. L. S. (2010) Thickness and structure of the water film deposited from vapour on calcite surfaces. *Geochim. Cosmochim. Acta* **74**, 5985–5999.

Beaglehole D. and Christenson H. K. (1992) Vapor adsorption on mica and silicon: Entropy effects, layering, and surface forces. *J. Phys. Chem.* **96**, 3395–3403.

Campbell G. S. and Shiozawa S. (1992) Prediction of hydraulic properties of soils using particle-size distribution and bulk density data. In *Indirect methods for estimating the hydraulic properties of unsaturated soils* (eds. M. T. van Genuchten and F. J. Leij). Univ. of Calif. Press, Riverside, Calif., pp. 317–328.

Churaev N. V. (2003) Surface forces in wetting films. *Adv. Colloid Interface Sci.* **103**, 197–218.

Ciunel K., Armélin M., Findenegg G. H. and von Klitzing R. (2005) Evidence of surface charge at the air/water interface from thin-film studies on polyelectrolyte-coated substrates. *Langmuir* **21**, 4790–4793.

Derjaguin B. and Kussakov M. (1939) Anomalous properties of thin polymolecular - Films V An experimental investigation of polymolecular solvate (adsorbed) films as applied to the development of a mathematical theory of the stability of colloids. *Acta Physicochim. URSS* **10**, 153–174.

Derjaguin B. V. and Churaev N. V. (1974) Structural component of disjoining pressure. *J. Colloid Interface Sci.* **49**, 249–255.

Gee M. L., Healy T. W. and White L. R. (1999) Hydrophobicity effects in the condensation of water films on quartz. *J. Colloid Interface Sci.* **140**, 450–465.

Israelachvili J. N. (1992) *Intermolecular and Surface Forces*. Academic Press, New York.

Langmuir I. (1938) Repulsive forces between charged surfaces in water, and the cause of the Jones-Ray effect. *Science* **88**, 430–432.

Lebeau M. and Konrad J. M. (2010) A new capillary and thin film flow model for predicting the hydraulic conductivity of unsaturated porous media. *Water Resour. Res.* **46**, W12554.

Mercury L. and Nakashima S. (2004) Review on water around solutes and on solids: macroscopic thermodynamics and microscopic views. In *Physicochemistry of water in geological and biological systems*. (eds. S. Nakashima, C. J. Spiers, L. Mercury, P. A. Fenter and M. F. Hochella Jr.). Universal Academy press, Tokyo. pp. 19–44.

Nishiyama N., Yokoyama T. and Takeuchi S. (2012) Size distributions of pore water and entrapped air during drying-infiltration processes of sandstone characterized by water-expulsion porosimetry. *Water Resour. Res*. **48**, W09556.

Nishiyama N. and Yokoyama T. (2013) Does the reactive surface area of sandstone depend on water saturation?—The role of reactive-transport in water film. *Geochim. Cosmochim. Acta* **122**, 153–169.

Parker J. C. and Lenhard R. J. (1987) A model for hysteretic constitutive relations governing multiphase flow: 1. Saturation-pressure relations. *Water Resour. Res*. **23**, 2187–2196.

Pashley R. M. and Kitchener J. A. (1979) Surface forces in adsorbed multilayers of water on quartz. *J. Colloid Interface Sci*. **71**, 491–500.

Pentland, C. H., El-Maghraby R., Iglauer S. and Blunt M. J. (2011) Measurements of the capillary trapping of super-critical carbon dioxide in Berea sandstone. *Geophys. Res. Lett*. **38**, L06401.

Read A. D. and Kitchener J. A. (1969) Wetting films on silica. *J. Colloid Interface Sci*. **30**, 391–398.

Tokunaga T. K. (2011) Physicochemical controls on adsorbed water film thickness in unsaturated geological media. *Water Resour. Res*. **47**, W08514.

Tokunaga T. K. (2012) DLVO-based estimates of adsorbed water film thickness in geologic CO_2 reservoirs. *Langmuir* **28**, 8001–8009.

Tuller M., Or D. and Dudley L. M. (1999) Adsorption and capillary condensation in porous media: liquid retention and interfacial configurations in angular pores. *Water Resour. Res*. **35**, 1949–1964.

Yokoyama T., Nakashima S., Murakami T., Mercury L. and Kirino Y. (2011) Solute distribution in porous rhyolite as evaluated by sequential centrifugation. *Appl Gechem*. **26**, 1524–34.

Yokoyama T. and Nishiyama N. (2013) Role of water film in weathering of porous rhyolite under water unsaturated condition. *Proc. Earth Planet. Sci*. **7**, 916–919.

Chapter 6

A Reactive-Transport Model for Water Film in Unsaturated Rocks

Abstract

A reactive-transport model for quantitatively describing the dissolution and diffusion in water film was derived. The model shows that the solute concentration in a film is a function of the film thickness, diffusion length, dissolution rate of the mineral, equilibrium concentration, and roughness factor. As for the Fontainebleau sandstone, film thicknesses of 7–18 nm and diffusion lengths of 300–600 μm were estimated. The reactive-transport calculation confirmed that the overall dissolution rate of Fontainebleau sandstone sample was almost unaffected by water saturation, owing to the high flushing efficiency of dissolved Si in water film, which agrees with the experimental result. The model found the condition that even if the mineral-water "contact" area is similar between saturated condition and unsaturated conditions due to the presence of water film, the surface area available for dissolution under unsaturated condition is lower than that under saturated condition due to the retardation of dissolution by slow flushing. By seeking this condition for rocks with a variety of mineral compositions, grain sizes, and pore diameters, a diagram to assess whether the reactive surface area decreases with water saturation was obtained. The model can provide a basic concept for evaluating the role of water film on the dissolution behavior under water-unsaturated conditions.

6.1. Introduction

The flow-through dissolution experiments using the Fontainebleau sandstone (~100% quartz) at various water saturations have shown that total amount of dissolved Si did not change with decreasing water saturation. The results are most likely to be explained by the occurrence of dissolution and mass transport in water film wetting quartz grain surfaces in air-containing pores. Because the dissolution rate of a mineral generally decreases with increasing solute concentration, the results also suggested that the flushing of dissolved Si through water film was fast enough to keep the concentration in the film low compared to the equilibrium concentration of quartz. In this chapter, to theoretically underpin this finding, we constructed a reactive-transport model considering the effect of water film. Such reactive-transport modeling is useful because it can provide knowledge of the factors that control the reactive-transport process and solute concentration in water film and it enables to predict the behavior of dissolution induced by water film for rocks having various mineral compositions and pore structure.

6.2. Model for Coupled Dissolution-Diffusion through Water Film

For modeling the dissolution and transport occurring in water film, we assume that a pore has a cylindrical shape with a diameter of d_{pore} (m) and that the central part of the pore is occupied by air (Fig. 6.1a). The pore wall is composed of a uniform mineral and wetted by water film with a thickness of h (m) and a length of L (m) (diffusion length). In the water film, the solute concentration increases from the flow path toward the film and thereby diffusional transport occurs. However, advective transport in the film may also occur. Thus, we first estimated whether diffusion or advection dominates the overall mass transport in water film. The relative amount of elemental flux of diffusion versus flow can be described using the Péclet number (Pe, dimensionless) (e.g., *Lasaga*, 1998):

$$Pe = \frac{vL}{D_0} \tag{6.1}$$

where v (m s^{-1}) is the flow velocity and D_0 (m^2 s^{-1}) is the self-diffusion coefficient. At low Péclet numbers ($Pe \ll 1$), diffusion dominates the mass transfer and the flow is negligible. In contrast, for $Pe \gg 1$, the transport is mainly controlled by the flow. The volume flow rate q_{film} (m^3 s^{-1}) through the circular wetting film, as described in Fig. 6.1a, can be represented by the following equation (*Ershov et al.*, 2001):

$$q_{film} = \frac{\pi \rho_w g d_{pore} h^3}{3\mu} \frac{\Delta H_{film}}{L} \tag{6.2}$$

where ΔH_{film} (m) is the water head difference in the water film and $\Delta H_{film}/L$ corresponds to the hydraulic gradient in the film. The flow velocity can be calculated from Eq. (6.2) as follows:

$$v = \frac{\rho_w g h^2}{3\mu\left(1 - h/d_{pore}\right)} \frac{\Delta H_{film}}{L} \tag{6.3}$$

Because a hydraulic gradient of ~10 was applied to the sample in our flow-through dissolution experiments, $\Delta H_{film}/L = 10$ was assumed as a maximum value. Fig. 6.2 shows the Pe calculated from Eqs. (6.1) and (6.3) as a function of the water film thickness and L. For film thicknesses of 7–18 nm and L of 300–600 μm, similar to our sample (procedures of estimating these parameters are described below), Pe is lower than 1 (Fig. 6.2). Therefore, it is reasonable to assume that the transport of dissolved Si in the wetting film of our sandstone sample is mainly controlled by

diffusion rather than by advection. If $\Delta H_{\text{film}}/L$ is lower than the above case ($\Delta H_{\text{film}}/L$ = 10), Pe becomes lower and the contribution of diffusion becomes much larger than advection, which often seems to be the case with Earth's surface conditions (Fig. 6.2). Our reactive-transport model, therefore, considers diffusional transport only, but the flushing rate of solute becomes faster if the contribution of advection is added to the model.

By mass balance in water film, the following formula is obtained:

$$
\begin{aligned}
\frac{\partial c}{\partial t} &= D_0 \frac{\partial^2 c}{\partial x^2} + \frac{A}{V_{\text{film}}} r_{\text{const}} \left(1 - \frac{c}{c_{\text{eq}}}\right) \\
&= D_0 \frac{\partial^2 c}{\partial x^2} + \frac{\lambda}{h(1 - h/d_{\text{pore}})} r_{\text{const}} \left(1 - \frac{c}{c_{\text{eq}}}\right)
\end{aligned}
\tag{6.4}
$$

where c (mol m^{-3}) is the concentration of a dissolved solute in the water film, t (s) is the time, x (m) is the position in the water film (x = 0 and x = L correspond to the position where water film connects to the adjacent water-filled pore), and c_{eq} (mol m^{-3}) is the equilibrium concentration. V_{film} (m^3) is the volume of water film and is given by $V_{\text{film}} = \pi (d_{\text{pore}}/2)^2 L - \pi (d_{\text{pore}}/2 - h)^2 L = \pi h (d_{\text{pore}} - h) L$. A (m^2) is the mineral-water reactive surface area and is assumed to be equal to $\pi d_{\text{pore}} L \lambda$, which is the product of the geometric surface area of the pore wall ($\pi d_{\text{pore}} L$) and a roughness factor (λ). λ is calculated by BET surface area / geometric surface area and is usually greater than 1 (*White*, 2008; *White and Peterson*, 1990). The magnitude of λ may be attributed to etch pits, internal pores, and the surface topography of grains. Although such surface roughness may affect L, surface holes smaller than the pore size are expected to be filled with water under thermodynamic equilibrium with vapor due to capillary condensation. Thus, it is unlikely that solutes migrate through the tortuous film along the surface roughness as long as the surface holes are small; therefore, the use of L, which is equal to the length along the smooth surface, is reasonable. In Eq. (6.4), m = n = 1 in Eq. (4.2) was assumed because otherwise, it was difficult to obtain an analytical solution. Although a numerical solution can be gained for various m and n, the analytical solution has an advantage in clarifying the parameters controlling the dissolution-transport behavior in wetting film. At steady state ($\partial c/\partial t = 0$), the solution of Eq. (6.4) is given by

$$
c(x) = E e^{\alpha x} + F e^{-\alpha x} + c_{\text{eq}}
\tag{6.5}
$$

$$\alpha = \left\{ \frac{\lambda r_{\text{const}}}{h\left(1 - h/d_{\text{pore}}\right)c_{\text{eq}}D_0} \right\}^{\frac{1}{2}}$$

where E and F are constant. Under the boundary condition of $c(0) = c(L) = c_1$, the solution is

$$c(x) = \frac{c_{\text{eq}} - c_1}{e^{\alpha L} - e^{-\alpha L}}\left[\left(e^{-\alpha L} - 1\right)e^{\alpha x} - \left(e^{\alpha L} - 1\right)e^{-\alpha x}\right] + c_{\text{eq}} \qquad (6.6)$$

Fig. 6.1b shows the concentration profiles calculated by Eq. (6.6) for various αL. The concentrations increase with increasing αL. Here, we define the flushing rate R_{flush} (mol s^{-1}) as the diffusional flux of a solute removed from the wetting film. R_{flush} can be calculated by the product of the diffusional flux $J(x)$ (mol m^{-2} s^{-1}) at $x = 0$ and L and the cross-sectional area of the wetting film ($\pi(d_{\text{pore}} - h)h$):

$$R_{\text{flush}} = 2 \times J(0) \times \pi\left(d_{\text{pore}} - h\right)h \qquad (6.7)$$

The equation is multiplied by 2 because it is assumed that solutes are flushed from the two ends at $x = 0$ and L (Fig. 6.1a) and the diffusional fluxes at both ends are equal. The diffusional flux is given by Fick's first law:

$$J(x) = -D_0 \frac{dc}{dx} \qquad (6.8)$$

By combining Eqs. (6.6)–(6.8), R_{flush} is obtained as:

$$R_{\text{flush}} = \frac{2\pi d_{\text{pore}}\lambda r_{\text{const}}}{\alpha}\left(1 - \frac{c_1}{c_{\text{eq}}}\right)\frac{e^{\alpha L} - 1}{e^{\alpha L} + 1} \qquad (6.9)$$

At the steady state, R_{flush} must be equal to the total amount of dissolution from the pore wall per unit time (R_{diss}). Therefore, the surface area-normalized dissolution rate of the mineral exposed to the wetting film r_{film} (mol m^{-2} s^{-1}) is determined from Eq. (6.9):

$$r_{\text{film}} = \frac{R_{\text{flush}}}{\pi d_{\text{pore}}L\lambda} = \frac{2r_{\text{const}}}{\alpha L}\left(1 - \frac{c_1}{c_{\text{eq}}}\right)\frac{e^{\alpha L} - 1}{e^{\alpha L} + 1} \qquad (6.10)$$

The model presented here shows that the concentration in the film and r_{film} are a function of the film thickness, diffusion length, pore diameter, far from equilibrium dissolution rate, equilibrium concentration, and roughness factor. If $d_{\text{pore}} \gg h$, the term $\left(1 - h/d_{\text{pore}}\right)$ in α approaches 1 and d_{pore} apparently has no obvious effect on

the concentration and r_{film}. αL in Eqs. (6.6) and (6.10) relates to Damköhler number (Da, dimensionless), accounting for the relative contribution of diffusion and dissolution. Da is expressed as $\tau_{\text{flush}}/\tau_{\text{diss}}$, where τ_{flush} and τ_{diss} are the characteristic times for diffusion and dissolution, respectively (*Steefel*, 2008). If $Da <$ 1 ($\tau_{\text{flush}} < \tau_{\text{diss}}$), the diffusion is fast relative to the dissolution. Because $\tau_{\text{flush}} = L^2/D_0$ and $\tau_{\text{diss}} = V_{\text{film}}c_{\text{eq}}/A_{\text{film}}r_{\text{const}}$ for the case of the model presented here, Da is expressed as $\lambda r_{\text{const}}L^2/h(1-h/d_{\text{pore}})c_{\text{eq}}D_0$, which corresponds to $(\alpha L)^2$. Fig. 6.1c shows how r_{film} changes with αL. For $\alpha L < 1$, the efficiency of flushing in the wetting film is good, and low concentrations (Fig. 6.1b) and high dissolution rates (Fig. 6.1c) are maintained. In this case, r_{film} depends on only the boundary concentration (c_1). If c_1 ~ 0, r_{film} is equal to r_{const} (far from equilibrium dissolution rate). As αL increases beyond 1, r_{film} is more retarded by slow flushing and eventually approaches 0 (Fig. 6.1c).
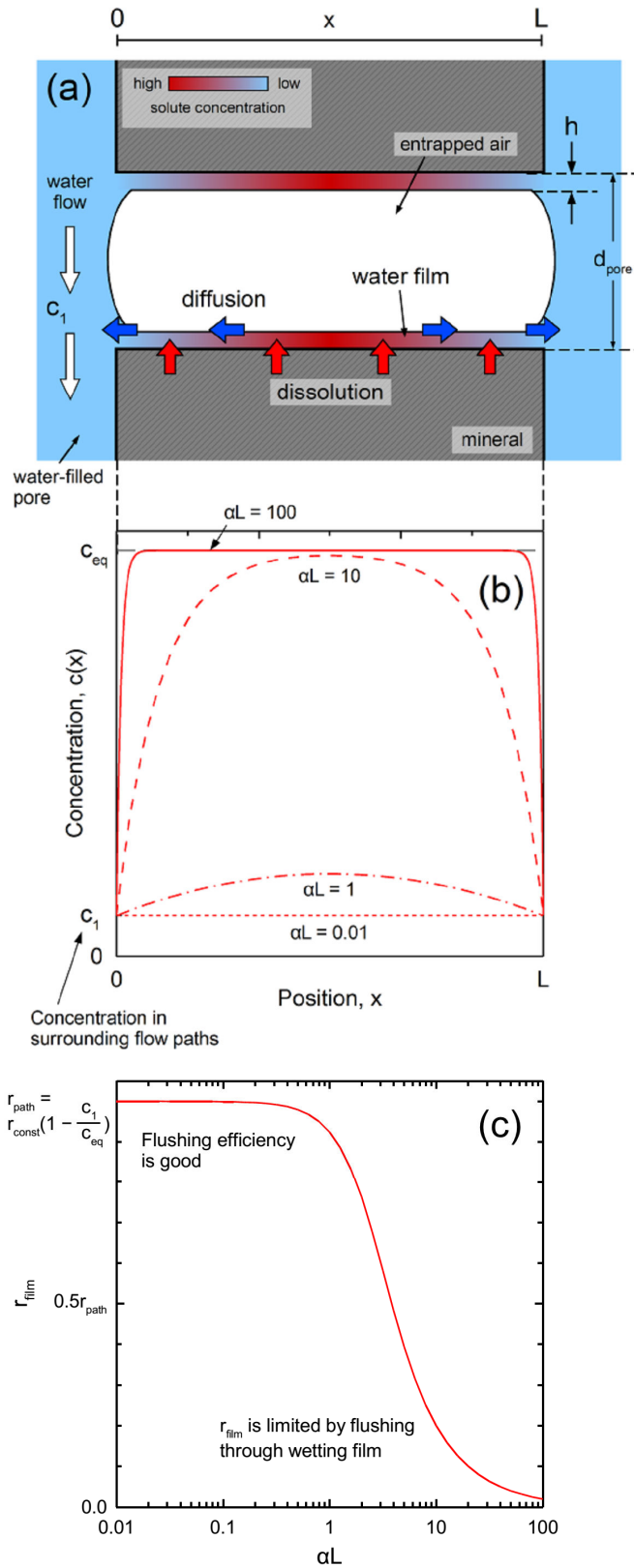
Fig. 6.1. (a) Schematic view of the model for coupled dissolution-diffusion through the wetting film. (b) Steady-state concentration profiles in wetting film along the axis of a

pore for αL = 0.01, 1, 10, and 100. (c) Dissolution rate in wetting film r_{film} as a function of αL. αL relates to Damköhler number ($Da = (\alpha L)^2$) and accounts for the relative contribution of diffusion and dissolution in wetting film. For $\alpha L < 1$, the evolution of the concentration in wetting film is small, and therefore, r_{film} is affected only by c_1. As αL increases, diffusional transport exerts a greater control over r_{film} in the wetting film (see text for details).
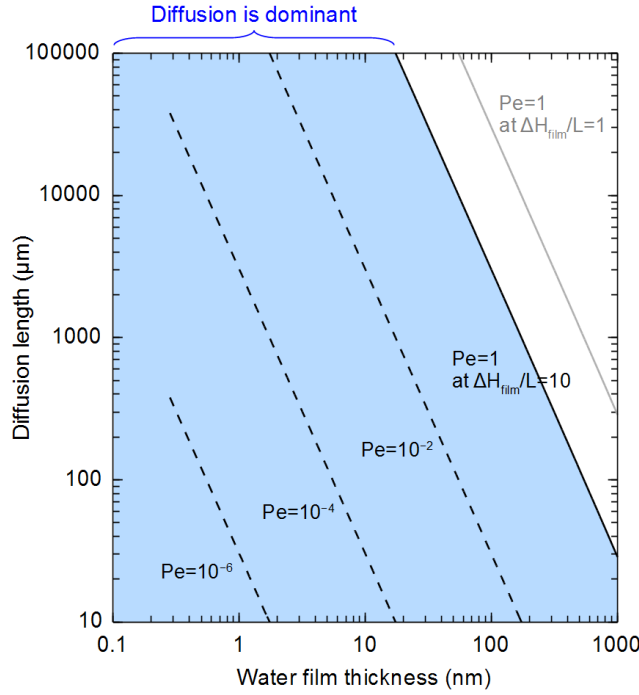

Fig. 6.2. Péclet number (Pe) as a function of wetting film thickness and diffusion length calculated by Eq. (6.1) at $\Delta H_{film}/L$ = 10 (Pe = 1 at $\Delta H_{film}/L$ = 1 is also given). The conditions where diffusion is a dominant transport mechanism are shown in light blue.

6.3. Model Results

6.3.1. The Case of Fontainebleau Sandstone

In this section, we calculate r_{film} for the dissolution of Fontainebleau sandstone in our experimental condition. Parameters required are D_0, r_{const}, c_{eq}, c_1, λ, d_{pore}, L, and h. These parameters are summarized in Table 6.1. The D_0 of aqueous Si at 22 °C is 1.0×10^{-9} m^2 s^{-1}, based on the relationship of $D_0 = 3.33 \times 10^{-15} T/\mu$ proposed by *Rebreanu et al.* (2008) (μ = 9.6×10^{-4} Pa s is the viscosity of water at 22°C). r_{const} is 4.1×10^{-14} mol m^{-2} s^{-1} (see Chapter 4). c_1 was assumed to be 0 because the Si

concentrations in the output solutions was significantly low (c_1/c_{eq} < 0.01 at steady state). λ = 11 was obtained by dividing the BET specific surface area (0.10 m^2 g^{-1}) by the geometric specific surface area (9.1 × 10^{-3} m^2 g^{-1}). The geometric specific surface area was calculated by $6/d_{grain}\rho_m$ (grains were assumed to be smooth spheres), where d_{grain} = 250 μm is the mean grain diameter and ρ_m is the density of the mineral grain (2.65 × 10^3 kg m^{-3} for quartz). The d_{pore} are 7–43 μm, based on the measured pore size distribution (Fig. 4.1b). L depends on the size and shape of the entrapped air. In our flow path visualization experiment (Chapter 4), entrapped air with sizes of less than 1 mm was observed throughout the sample. *Kumar et al.* (2010) also reported that more than 70% of the entrapped air in Fontainebleau sandstones is smaller than 600 μm in size. Therefore, entrapped air mainly has the lengths of 1–2 grains (300–600 μm). Although larger air with sizes of a few millimeters was also found in both studies, L is not necessarily equal to the length of the entrapped air for the following reasons: A pore is often connected to several adjacent pores. The number of pores connected to a given pore in sandstone, called the coordination number, was reported to be 2–10 (*Kwiecien et al.*, 1990). Large, branched, entrapped air would be surrounded by many adjacent water-filled pores, and water is flowing in some of the water-filled pores. Because solutes are flushed if they reach the nearest flow paths, L can be shorter than the length of entrapped air. Therefore, it seems reasonable to adopt 300–600 μm as L values. h was estimated to be 7–18 nm based on Eq. (5.6) with d_{pore} = 7–43 μm. Here, we used Eq. (5.4) to calculate $\Pi_e(h)$ because the ionic strengths of pore solution during the flow-through dissolution experiments were expected to be very low (only quartz was dissolved). We computed $\Pi_m(h)$ with A_{svl} = −1.3 × 10^{-20} J for quartz (*French*, 2000). Because h was sufficiently small compared to the pore diameters of the sample (7–43 μm), the pore size dependence of r_{film} was negligible.

　　Fig. 6.3a shows the concentration profile of dissolved Si for Fontainebleau sandstone calculated by Eq. (6.6) using h = 7 nm and 18 nm for L = 300 μm. The concentration in the wetting film is significantly lower than c_{eq}. Fig. 6.3b shows the dissolution rate of quartz in the wetting film (r_{film}) calculated by Eq. (6.10) as a function of film thickness. As the film thickness increases, r_{film} increases. Fig. 6.3c shows the proportion of r_{film} to the far from equilibrium dissolution rate r_{const}. From the values of r_{film} and r_{film}/r_{const} (grey areas in Figs. 6.3b and c), r_{film} was estimated to be lower than r_{const} by at most approximately 3%. This value is within the error in the measurement of overall dissolution rate. These results reveal that when quartz grains are in contact with the film in a water-unsaturated condition, the flushing rate of dissolved Si is fast enough to keep the concentration sufficiently low, and therefore, the

dissolution rate is not limited by the flushing (diffusion) through the wetting film. This is consistent with the experimental results of flow-through dissolution experiment.

Table 6.1. Parameters for calculating the concentration and the dissolution rate of quartz in the wetting film of Fontainebleau sandstone.

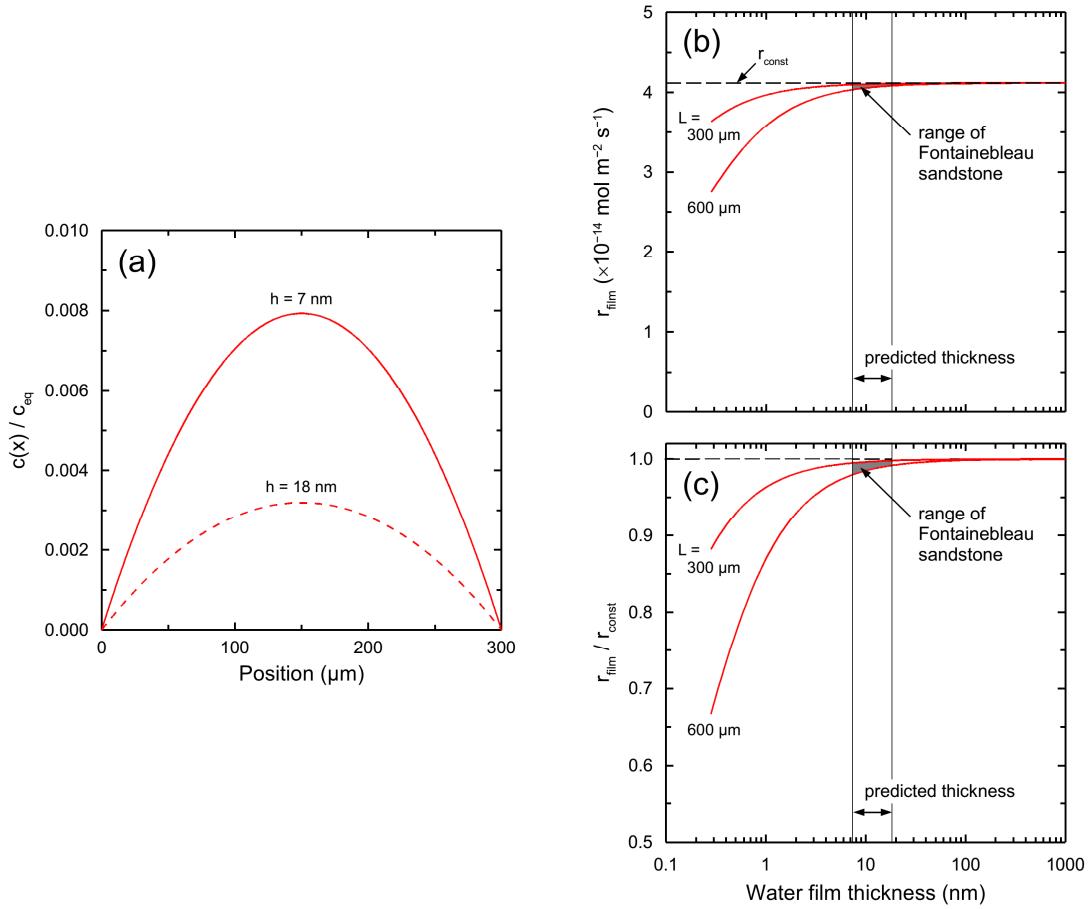| Variable	Unit	Value
D_0	$m^2\ s^{-1}$	1.0×10^{-9}
r_{const}	$mol\ m^{-2}\ s^{-1}$	4.1×10^{-14}
c_{eq}	$mol\ kg^{-1}$	8.9×10^{-5}
c_1	$mol\ kg^{-1}$	0
λ	unitless	11
d_{pore}	μm	7–43
L	μm	300–600
h	nm	7–18

Fig. 6.3. (a) Concentration profiles of dissolved Si in wetting film for the case of Fontainebleau sandstone. (b) Dissolution rate of quartz in water film (r_{film}) as a function of wetting film thickness for $L = 300$ and 600 μm. The horizontal dashed line represents the dissolution rate at far from equilibrium (r_{const}). (c) The proportion of r_{film} to r_{const} for $L = 300$ and 600 μm as a function of thickness. The vertical solid lines designate the range of predicted thicknesses of wetting film (see text). The grey area corresponds to the range of r_{film} and r_{film}/r_{const} for the sandstone.

6.3.2. Prediction of Effect of Water Saturation on Dissolution Behavior for Sedimentary Rocks

On the basis of the reactive-transport model considering the effect of water film, we can consider how water saturation influences the dissolution rate for general cases. We focus on sedimentary rocks taking into account the similarity of the pore structure with Fontainebleau sandstone. In section 6.2, we evaluated the extent to which the concentration in water film is higher than that in the flow path (c_1). In a natural system, as rain water infiltrates deep underground, the concentrations in the flow paths increase and eventually reach equilibrium. Here, we seek for the condition at which the flushing

rate of solutes in the film is sufficiently fast and dissolution rates in the flow path and in the film become equal. If the concentration in the flow path at a particular depth is c_1, the dissolution rate of the mineral exposed to the flow path r_{path} (mol m^{-2} s^{-1}) is given by

$$r_{path} = r_{const}\left(1 - c_1/c_{eq}\right).$$ (6.11)

In addition, the dissolution rate in water film around the corresponding depth (r_{film}) is described by Eq. (6.10). As an index to evaluate the proximity of r_{film} to r_{path}, we use the following value:

$$\frac{r_{film}}{r_{path}} = \frac{2}{\alpha L}\frac{e^{\alpha L} - 1}{e^{\alpha L} + 1}$$ (6.12)

If $r_{film}/r_{path} \sim 1$ ($\alpha L < 1$), the flushing of solute in water film is fast enough that the concentration in the film is close to c_1 (Fig. 6.1b). As r_{film}/r_{path} decreases from 1 to 0 ($\alpha L > 1$), the flushing efficiency decreases and the concentration in the film approaches c_{eq} (Fig. 6.1b). At the low flushing efficiency, the mineral-water "contact" area may be similar between water-saturated and unsaturated conditions, but the "active" surface area under unsaturated conditions is lower than that under saturated condition. Fig. 6.4 shows the values of r_{film}/r_{path} for quartz, K-feldspar, and kaolinite plotted against film thickness for L = 100 and 1000 μm with λ = 10 and 1. For simplicity, congruent dissolution was assumed and the dissolution and transport of Si was considered. The values of r_{const} and c_{eq} used are those at 25°C and pH = 5 (Table 6.2). As the film thickens and the diffusion length and roughness factor decrease, r_{film}/r_{path} approaches 1. It is possible to evaluate the condition at which r_{film} is approximately similar to r_{path} for given minerals and grain sizes. Quartz (Qz), muscovite (Ms), albite (Ab), K-feldspar (Kf), anorthite (An), diopside (Di), forsterite (Fo), and Kaolinite (Ka) were chosen, and for each mineral the condition at which r_{film}/r_{path} is larger than 0.9 was determined. Under this condition, the difference between r_{film} and r_{path} is within 10% and water-saturated and unsaturated conditions have similar "active" surface areas. The combinations of h and L were determined by searching h at which r_{film}/r_{path} becomes 0.9 at a given L (examples are shown as diamonds in Fig. 6.4). The results at λ = 1 and 10 are shown in Fig. 6.5. To use this diagram, h and L of a rock are required. h for a given mineral and solution composition can be calculated by d_{pore} using Eq. (5.6). As for L, according to the

researches addressing the size of entrapped gas or oil in glass bead columns and sandstones, the majority of the entrapped fluid has lengths of 1–2 grains (*Mayer and Miller*, 1992; *Al-Raoush and Willson*, 2005; *Kumar et al.*, 2010) although some may have lengths of 5–6 grains (*Chatzis et al.*, 1988; *Al-Raoush and Willson*, 2005). By combining these results with the idea for L as described in section 6.3.1, it seems reasonable to estimate that in many types of sediment L is 1–2 grains in size, and the mean grain size can be used as a first approximation. As a guide for estimating the grain size, the classification of sedimentary rocks based on the grain size is given in Fig. 6.5. When the values of a rock of interest is plotted in the h-L diagram, if the line of a mineral is located above the plot of the rock, the dissolution rate in the flow paths and in the film are almost equal (the dissolution rate is not controlled by the flushing of solute in the water film, and the reactive surface area is not affected by water saturation). In contrast, if the line of a mineral is located below the plot, the dissolution rate of the mineral in the film is slower than that in the flow paths. For quartz, the line is located above the data of our Fontainebleau sandstone sample (area with dotted line in Fig. 6.5b), and this is consistent with the experimental results.

Although the above reactive-transport model assumes that flow occurs homogeneously, for rocks this assumption is not satisfied, L may be longer than the grain size due to the occurrence of preferential flow. There are many other factors that may affect the calculation. For example, the dissolution of minerals was assumed to be congruent, but many silicates are known to dissolve incongruently (e.g., *Brantley*, 2008). The thickness of the water film was determined based on the disjoining pressure that is related to the diffuse double layer. The major species of dissolved Si at neutral pH is electrically neutral $Si(OH)_4$ (*Sjöberg*, 1996), and as long as dissolved Si alone is considered, its effect on film thickness may be relatively small. However, when cation and anion concentrations are high, their effect on film thickness may not be negligible. In such cases, it may be better to employ the equation proposed by *Gregory* (1975) to calculate the electrical component of disjoining pressure. We used the self-diffusion coefficient of Si in bulk water for calculating diffusional transport in water film. Molecular dynamics simulations have proposed that the self-diffusion coefficients of water and ions in proximity to the mineral-water interface (at distances of up to 2.0–2.5 nm from the solid surface) are different from those in bulk water for orthoclase (*Kerisit and Liu*, 2009), muscovite (*Sakuma and Kawamura*, 2011) and smectite (*Bourg and Sposito*, 2011). According to *Kerisit and Liu* (2009), the diffusion coefficient of water in a 5 nm width pore is ~80% of that of bulk water. In the case of Fontainebleau sandstone, the change in the diffusion coefficient may be much smaller because the film is thicker

(7–18 nm) and the solid surface is present only on one side of the water film. This extent of change has an insignificant effect on our results, but such effects may not be negligible when the film is much thinner. Although these factors need to be considered in future works, the model presented in the present study provides a basic concept for evaluating the role of water film and predicting the dissolution behavior under water-unsaturated conditions.

Table 6.2. Dissolution rate constants and equilibrium Si concentrations of minerals at 25°C and pH = 5.

Mineral	Reaction stoichiometry	$\log r_{const}$[a] $(mol\ m^{-2}\ s^{-1})$	c_{eq}[b] $(mol\ kg^{-1})$
Quartz	$SiO_2 \rightarrow SiO_2(aq)$	-13.1[c]	9.9×10^{-5}
Muscovite	$KAl_3Si_3O_{10}(OH)_2 + 10H^+ \rightarrow K^+ + 3Al^{3+} + 3SiO_2(aq) + 6H_2O$	-12.5[d]	9.7×10^{-6}
Albite	$NaAlSi_3O_8 + 4H^+ \rightarrow Na^+ + 3SiO_2(aq) + Al^{3+} + 2H_2O$	-11.9[e]	1.0×10^{-3}
K-feldspar[f]	$KAlSi_3O_8 + 4H^+ \rightarrow K^+ + Al^{3+} + 3SiO_2(aq) + 2H_2O$	-11.8[g]	2.6×10^{-4}
Anorthite	$CaAl_2Si_2O_8 + 8H^+ \rightarrow Ca^{2+} + 2Al^{3+} + 2SiO_2(aq) + 4H_2O$	-11.3[h]	3.0×10^{-3}
Diopside	$CaMgSi_2O_6 + 4H^+ \rightarrow Ca^{2+} + Mg^{2+} + 2SiO_2(aq) + 2H_2O$	-10.7[i]	1.1
Forsterite	$Mg_2SiO_4 + 4H^+ \rightarrow 2Mg^{2+} + SiO_2(aq) + 2H_2O$	-8.5[i]	2.7
Kaolinite	$Al_2Si_2O_5(OH)_4 + 6H^+ \rightarrow 2Al^{3+} + 2SiO_2(aq) + 5H_2O$	-12.3[j]	1.5×10^{-6}

[a] Release rate of Si.

[b] Equilibrium concentration of Si calculated using PHREEQC (*Parkhurst and Appelo*, 1990) with the minteq database.

[c] *Bennett et al.* (1988).

[d] *Lin and Clemency* (1981a) and *Nagy* (1995).

[e] *Knauss and Wolery* (1986).

[f] Assumed as microcline.

[g] *Busenberg and Clemency* (1976).

[h] *Amrhein and Suarez* (1992).

[i] *Golubev et al.* (2005).

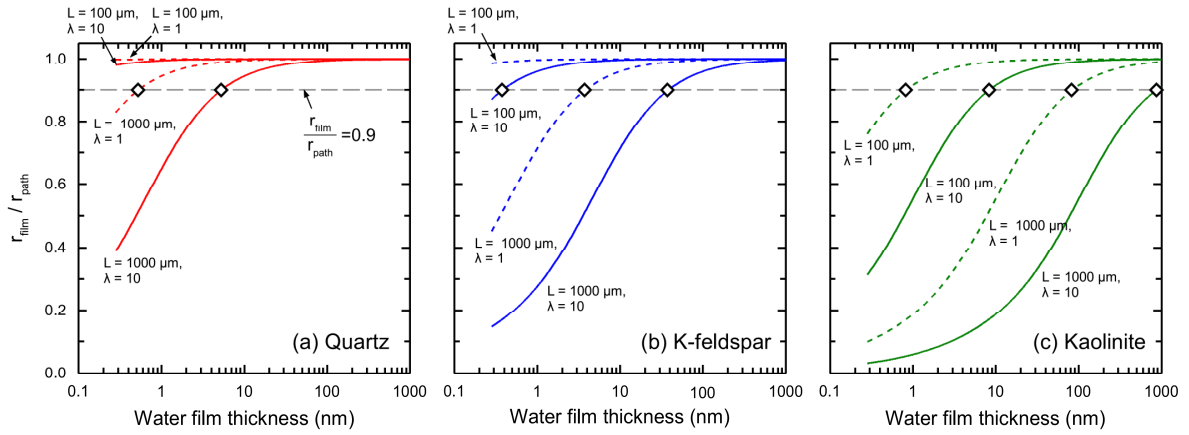[j] *Carroll-Webb and Walther* (1988).

Fig. 6.4. r_{film}/r_{path} of quartz (a), K-feldspar (b), and kaolinite (c) at L = 100 and 1000 μm and at λ = 1 (dotted lines) and 10 (solid lines) as a function of wetting film thickness.
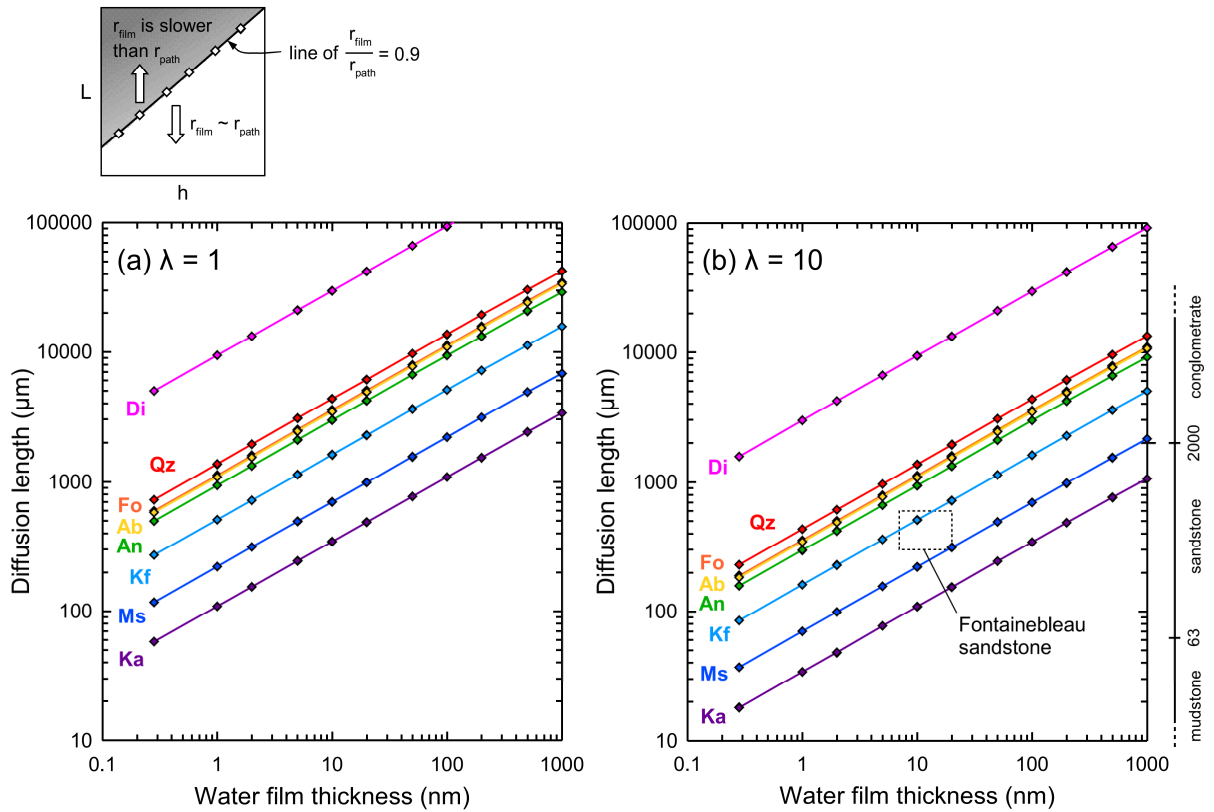

Fig. 6.5. Relationship between wetting film thickness and diffusion length to satisfy r_{film} = $0.9\, r_{path}$, equivalent to the condition at which the dissolution rate of the mineral in water film is little-retarded by the transport of solutes in the film. In this case, the active surface area under water-unsaturated conditions is similar to that under saturated condition. The lines were obtained from Eq. (6.12) using values in Table 2 for λ = 1 (a) and 10 (b). A

106

temperature of 25°C and a pH of 5 are assumed. If the line of a mineral is located above the plot of the rock of interest, the difference of the dissolution rates of the mineral in water film and flow paths is less than 10%, and vice versa.

6.4. Conclusions

We constructed a model of reactive-transport in water film for quantitatively understanding the dissolution behavior under water-unsaturated conditions. The model shows that the solute concentration as well as the dissolution rate of the mineral wetted by water film is a function of the film thickness, diffusion length, far-from equilibrium dissolution rate, equilibrium concentration, and roughness factor. The model calculation for the case of Fontainebleau sandstone consisting of ~100% quartz under a uniform flow condition revealed that the efficiency of flushing by diffusion was high enough to keep low Si concentration in water film and as a result the dissolution rate in the film is only slightly limited by flushing, which is consistent with the results of the flow-through dissolution experiment. By applying the model to rocks with a variety of mineral compositions, grain sizes, and pore diameters, a diagram to assess whether the reactive surface area and the dissolution rate of the mineral change with water saturation was obtained. Although the diagram as well as the model successfully predicted the dissolution behavior of Fontainebleau sandstone, there are many factors potentially affecting the model parameters, including flow heterogeneity, diffusivity of ions in thin water film, and incongruent dissolution behavior of minerals. The experimental and theoretical evaluations of their effects would contribute to the better understanding and quantitative treatment of water-rock interactions in the vadose zone.

References

Al-Raoush R. I. and Willson C. S. (2005) A pore-scale investigation of a multiphase porous media system. *J. Contam. Hydrol.* **77**, 67–89.

Amrhein C. and Suarez D. L. (1992) Some factors affecting the dissolution kinetics of anorthite at 25°C. *Geochim. Cosmochim. Acta* **56**, 1815–1826.

Bennett P. C., Siegel D. I., Melcer M. E. and Hassett J. P. (1988) The dissolution of quartz in dilute aqueous solutions of organic acids at 25°C. *Geochim. Cosmochim. Acta* **52**, 1521–1530.

Bourg I. C. and Sposito G. (2011) Molecular dynamics simulations of the electrical double layer on smectite surfaces contacting concentrated mixed electrolyte (NaCl–CaCl$_2$) solutions. *J.*

Colloid Interface Sci. **360**, 701–715.

Brantely S. L. (2008) Kinetics of mineral dissolution. In *Kinetics of water-rock interaction.* (eds. S. L. Brantley, J. D. Kubicki and A. F. White). Springer Science+Business Media, LLC, New York. pp. 151–196.

Busenberg E. and Clemency C. V. (1976) The dissolution kinetics of feldspars at 25°C and 1 atm CO2 partial pressure. *Geochim. Cosmochim. Acta* **40**, 41–49.

Carroll-Webb S. A. and Walther J. V. (1988) A surface complex reaction model for the pH-dependence of corundum and kaolinite dissolution rates. *Geochim. Cosmochim. Acta* **52**, 2609–2623.

Chatzis I., Kuntamukkula M. S. and Morrow N. R. (1988) Effect of capillary number on the microstructure of residual oil in strongly water-wet sandstones. *SPE Reservoir Eng.* **3**, 902–912.

Ershov A. P., Zorin Z. M., Sobolev V. D. and Churaev N. V. (2001) Kinetics of gas bubble motion in a capillary. *Colloid J.* **63**, 200–207.

French R. H. (2000) Origins and applications of London dispersion and Hamaker constants in ceramics. *J. Am. Ceram. Soc.* **83**, 2117–2146.

Golubev S. V., Pokrovsky O. S. and Schott J. (2005) Experimental determination of the effect of dissolved CO2 on the dissolution kinetics of Mg and Ca silicates at 25°C. *Chem. Geol.* **217**, 227–238.

Gregory J. (1975) Interaction of unequal double layers at constant charge. *J. Colloid Interface Sci.* **51**, 44–51.

Kerisit S. and Liu C. (2009) Molecular simulations of water and ion diffusion in nanosized mineral fractures. *Environ. Sci. Technol.* **43**, 777–782.

Knauss K. G. and Wolery T. J. (1986) Dependence of albite dissolution kinetics on pH and time at 25°C and 70°C. *Geochim. Cosmochim. Acta* **50**, 2481–2497.

Kumar M., Senden T., Sheppard A., Middleton J. and Knackstedt M. (2010) Visualizing and quantifying the residual phase distribution in core material. *Petrophysics*. **51**, 323–332.

Kwiecien M. J., Macdonald I. F. and Dullien F. A. L. (1990) Three-dimensional reconstruction of porous media from serial sectional data. *J. Microsc.* **159**, 343–359.

Lasaga A. C. (1998) *Kinetic theory in the earth sciences.* Princeton University Press, New Jersey.

Lin F. C. and Clemency C. V. (1981) The kinetics of dissolution of muscovites at 25°C and 1 atm CO_2 partial pressure. *Geochim. Cosmochim. Acta* **45**, 571–576.

Mayer A. S. and Miller C. T. (1992) The influence of porous medium characteristics and measurement scale on pore-scale distributions of residual nonaqueous-phase liquids. *J. Contam. Hydrol.* **11**, 189–213.

Nagy K. L. (1995) Dissolution and precipitation kinetics of sheet silicates. In *Reviews in Mineralogy*, vol. 31 (eds. A. F. White and S. L. Brantley). Mineral. Soc. Amer. pp. 173–225.

Parkhurst, D. L. and Appelo, C. A .J. (1999) User's guide to PHREEQC (Version 2)— A computer program for speciation, batch-reaction, one-dimensional transport, and inverse geochemical calculations. Water-Resources Investigations Report 99–4259, pp. 312.

Rebreanu L., Vanderborght J. P. and Chou L. (2008) The diffusion coefficient of dissolved silica revisited. *Mar. Chem.* **112**, 230–233.

Sakuma H. and Kawamura K. (2011) Structure and dynamics of water on Li^+-, Na^+-, K^+-, Cs^+-, H_3O^+-exchanged muscovite surfaces: a molecular dynamics study. *Geochim. Cosmochim. Acta* **75**, 63–81.

Sjöberg S. (1996) Silica in aqueous environments. *J. Non Crystalline Solids* **196**, 51–57.

Steefel C. I. (2008) Geochemical kinetics and transport. In *Kinetics of water-rock interaction*. (eds. S. L. Brantley, J. D. Kubicki and A. F. White). Springer Science+Business Media, LLC, New York. pp. 545–585.

White A. F. and Peterson M. L. (1990) Role of reactive-surface-area characterization in geochemical kinetic models. *In Chemical modeling of aqueous systems II*. ACS symposium series 416. Eds. D. C. Melchior and R. L. Bassett. 461–475.

White A. F. (2008) Quantitative approaches to characterizing natural chemical weathering rates. In *Kinetics of water-rock interaction*. (eds. S. L. Brantley, J. D. Kubicki and A. F. White). Springer Science+Business Media, LLC, New York. pp. 469–532.

Lists of Publications and Presentations

Peer-Reviewed Papers
1. Nishiyama N. and Yokoyama T. (2013) Does the reactive surface area of sandstone depend on water saturation?—The role of reactive-transport in water film. *Geochim. Cosmochim. Acta* **122**, 153–169.

2. Nishiyama N., Yokoyama T. and Takeuchi S. (2012) Size distributions of pore water and entrapped air during drying-infiltration processes of sandstone characterized by water-expulsion porosimetry. *Water Resour. Res.* **48**, W09556.

In Revisions
3. Nishiyama N. and Yokoyama T. Prediction of permeability of sandstone by applying water-expulsion porosimetry to Katz and Thompson model. Submitted in *Eng. Geol.*

Proceedings (peer-reviewed)
1. Nishiyama N. and Yokoyama T. (2013) Estimation of water film thickness in geological media under the occurrence of gas entrapment. *Proc. Earth Planet. Sci.* **7**, 620-623.

2. Yokoyama T. and Nishiyama N. (2013) Role of water film in weathering of porous rhyolite under water unsaturated condition. *Proc. Earth Planet. Sci.* **7**, 916-919.

Other Publications (non peer-reviewed)
1. Nishiyama N. and Yokoyama T. (2011) Relationship between water saturation and mineral-water contact area of a sandstone. *Mineral. Mag.* **75**, 1554.

2. Bessho H., Nakashima S., Hamamoto M., Nishiyama N., Tonoue R., Kirino Y., Yokoyama T. and Sasamoto H. (2013) *In situ* monitoring of water-rock Interaction by micro FT-IR -An example of calcium silicate hydrate formation-. *Mineral. Mag.* **77**, 696.

3. Yokoyama T. and Nishiyama N. (2012) Drying behavior of a rock and its implication to weathering. *Mineral. Mag.* **76**, 2574.

Presentations in International Conferences
1. Nishiyama N. and Yokoyama T., Estimation of water film thickness in rock pores by introducing electric double layer interactions between mineral-water and water-air interfaces. International symposium on research frontiers of physics, earth and space science, Osaka, Japan,

December 2013 (Poster presentation).

2. <u>Nishiyama N.</u> and Yokoyama T., Estimation of water film thickness in geological media under the occurrence of gas entrapment. 14th Water-Rock Interaction, Avignon, France, June 2013 (Oral presentation).

3. <u>Nishiyama N.</u> and Yokoyama T., Relationship between water saturation and mineral-water contact area of a sandstone. 21th Goldschmidt Conference, Prague, Czech, August 2011 (Poster presentation).

4. <u>Nishiyama N.</u>, Yokoyama T. and Takeuchi S., Relationship between water content and permeability of a rock: an example of Fontainebleau sandstone. American Geophysical Union Fall Meeting 2009, San Francisco, USA, December 2009 (Poster presentation).

5. Umezawa R., Katsura M., <u>Nishiyama N.</u> and Nakashima S., Electrical impedance properties of water-containing sandstones. International symposium on research frontiers of physics, earth and space science, Osaka, Japan, December 2013.

6. Hamamoto M., Katsura M., <u>Nishiyama N.</u> and Nakashima S., Transmission IR spectra of water among colloidal silica particles. International symposium on research frontiers of physics, earth and space science, Osaka, Japan, December 2013.

7. Bessho H., Nakashima S., Hamamoto M., <u>Nishiyama N.</u>, Tonoue R., Kirino Y., Yokoyama T. and Sasamoto H. In situ Monitoring of Water-Rock Interaction by Micro FT-IR -An Example of Calcium Silicate Hydrate Formation-". 23th Goldschmidt conference, Florence, Italy, August 2013.

8. Yokoyama T. and <u>Nishiyama N.</u>, Role of water film in weathering of porous rhyolite under water unsaturated condition. 14th Water-Rock Interaction, Avignon, France, June 2013.

9. Bessho H., Nakashima S., <u>Nishiyama N.</u>, Tonoue R., Kirino Y., Yokoyama T., Walker C., and Sasamoto H., In-situ tracing of calcium silicate hydrate precipitation from high pH leachates by micro FT-IR. Clays in Natural and Engineered Barriers for Radioactive Waste Confinement, Montpellier, France, October 2012.

10. Kataoka Y., Nakashima S., <u>Nishiyama N.</u> and Yokoyama T., Attenuated total reflection infrared (ATR-IR) spectroscopy equipped with a humidity control system for studying amounts and sites of water adsorption on biological materials. 14th International Conference on Vibrations at Surfaces, Kobe, Japan, September 2012.

11. Yokoyama T. and <u>Nishiyama N.</u>, Drying behavior of a rock and its implication to weathering. 22th Goldschmidt Conference, Montreal, Canada, June 2012.

12. Kataoka Y., <u>Nishiyama N.</u>, Yokoyama T. and Nakashima S., Analysis of interactions between water and skin model compounds by attenuated total reflection infrared (ATR-IR)

spectroscopy. International Symposium at the 2011 Annual Meeting of the Spectroscopical Society of Japan, Kanagawa, Japan, November-December 2011.

13. Nakashima S., Kirino Y., <u>Nishiyama N.</u>, Tonoue R., Yokoyama T., Nagasawa M., Harui R., Walker C. and Sasamoto H., Quantitative tracing of water-rock interactions by IR spectroscopy–an example of alkaline alteration of granitic rocks. International Congress on Analysis Sciences 2011, Kyoto, Japan, May 2011.